

Copyright

by

Todd Keene Timberlake

2001

Signatures of chaos in periodically driven quantum systems

by

Todd Keene Timberlake, B.S.

Dissertation

Presented to the Faculty of the Graduate School of

the University of Texas at Austin

in Partial Fulfillment

of the Requirements

for the Degree of

Doctor of Philosophy

The University of Texas at Austin

May 2001

Signatures of chaos in periodically driven quantum systems

Approved by
Dissertation Committee:

To Karen.

Acknowledgments

I would like to thank my parents, Jack and Susan Timberlake, for their continuous support of my educational goals. I would like to thank my wife Karen, to whom this work is dedicated, for her patience while I completed my studies. Finally, I would also like to thank Drs. Linda Reichl and Will Chism for their endless advice and encouragement.

Signatures of chaos in periodically driven quantum systems

Publication No. _____

Todd Keene Timberlake, Ph.D.

The University of Texas at Austin, 2001

Supervisor: Linda E. Reichl

One-dimensional, time-periodic systems are the simplest systems that can exhibit classical chaos. The quantum versions of these systems are ideal for investigations of how classical chaos affects quantum dynamics. These systems are also relevant to recent experiments involving high-intensity, pulsed lasers. In this dissertation, we investigate open and closed quantum systems driven by a periodic field. We examine the phase-space structure of the Floquet eigenstates of these systems to determine their relationship to classical phase-space structures. We observe the effects of classical dynamics on the radiation spectra of these Floquet states and their superpositions. We show how avoided crossings can lead to delocalization of the Floquet states and illustrate how certain features of the classical motion can prevent this delocalization. We show how resonance states in an open system are

related to periodic orbits of the classical motion and how this relationship causes the number of resonance states in one system to increase as the driving field is increased. We examine how the phase-space structure of resonance states changes as they are destroyed by coupling to the continuum and as they pass through an avoided crossing. We also present a unified picture of the evolution of a closed quantum system as its classical counterpart becomes chaotic and we point out that modification of this picture is necessary to account for the phenomena observed in open systems.

Contents

Acknowledgments	v
Abstract	vi
1 Introduction	1
2 Harmonic generation in the driven square well	7
2.1 Dynamics of the Driven Square Well	8
2.1.1 Classical dynamics	8
2.1.2 Quantum dynamics	12
2.2 Radiation Spectra	14
2.2.1 Strong field	20
2.2.2 Very strong field	24
2.2.3 General properties	26
2.3 Avoided Crossings	30

3	Changes in Floquet-state structure at avoided crossings	38
3.1	Classical and Quantum Dynamics	39
3.2	Chaos and Avoided Crossings	41
3.3	Changes in Floquet State Structure	44
3.3.1	Sharp Crossing	45
3.3.2	Broad Crossing	46
3.4	Effect on Radiation Spectra	49
3.4.1	Sharp Crossing	53
3.4.2	Broad Crossing	54
4	The Transition to Chaos	60
4.1	Entropy and Delocalization	61
4.2	Avoided Crossings and Entropy	67
4.3	Classical Dynamics and Localization	77
4.3.1	Review of classical dynamics	77
4.3.2	Superscars: classical dynamics and localization	79
4.4	Eigenvalue Statistics and Chaos	88
4.5	Avoided crossings and classical dynamics	91
4.6	Matrix Picture of the Transition to Chaos	93
5	Creation of Quasienergy Resonance States	100

5.1	Driven Inverted Gaussian Model	102
5.2	Complex Coordinate Scaling	110
5.2.1	Standard complex coordinate scaling (CCS)	110
5.2.2	Exterior complex coordinate scaling	112
5.2.3	Husimi distributions and CCS	120
5.2.4	Floquet calculations	121
5.3	Resonance creation and scarring	128
5.4	Avoided crossings between resonances	135
6	Destruction of Quasienergy Resonance States	141
6.1	Time-Dependent Rosen-Morse Model	142
6.2	Resonance Destruction	144
6.3	Phase-space Picture	149
6.4	Coupling to the Continuum	157
6.5	Avoided Crossing	161
7	Conclusions and Discussion	169
A	Floquet Theory	173
B	The Husimi Distribution	175
C	Transformation from Radiation to Length Gauge	177

Bibliography	179
Vita	188

Chapter 1

Introduction

Despite the phenomenal success of quantum mechanics since its introduction in the early 20th Century, there are still some important aspects of the theory that are not clearly understood as we begin the 21st Century. One of these aspects is that of quantum-classical correspondence in systems whose classical dynamics is chaotic. Chaos, as it is usually defined, cannot exist in quantum mechanics. The concept of exponentially divergent trajectories that plays an important role in the classical definition of chaos has no analog in quantum mechanics because trajectories are not a well-defined concept in the quantum world. Because the Schrödinger equation is a linear partial differential equation it cannot produce chaotic solutions. However, quantum systems can exhibit many effects that are related to chaos in classical systems. Understanding these quantum signatures of classical chaos is vital to fully

understanding the relationship between quantum and classical mechanics.

There are a number of ways in which the properties of a quantum system can be related to the dynamics of its classical version. One approach is to relate properties of the quantum eigenvalue spectrum to the behavior of classical trajectories [1, 2]. Integrable systems with regular classical motion display an eigenvalue spectrum that is random and the level spacings follow Poisson statistics. Systems with chaotic classical dynamics have an eigenvalue spectrum that exhibits level repulsion, which is characterized by avoided crossings between the eigenvalue curves as a function of some parameter [3]. These avoided crossings change the distribution of level spacings from one described by Poisson statistics to one described by the statistics of random matrices [4].

Another way to study quantum-classical correspondence is to relate properties of the eigenfunctions of the quantum system to the classical dynamics. Quantum eigenstates can exhibit localization in phase space that is related to the presence of either Komolgorov-Arnol'd-Moser (KAM) tori or Cantori (broken KAM tori) in the classical phase space [5, 6]. However, quantum eigenstates can also exhibit a dynamical localization, similar to Anderson localization in disordered systems [7], that is not related to barriers in the classical phase space [8]. The localization of quantum eigenstates influences the statistics of the eigenvalue spectrum [9] and it has been proposed that avoided crossings lead to the delocalization of quantum

eigenstates, just as they lead to a change in the eigenvalue statistics [10]. One goal of this work is to examine the relationship between avoided crossings and the structure of quantum eigenstates.

To gain a more detailed understanding of the relationship between quantum and classical dynamics one would like to identify how individual quantum eigenstates are related to classical trajectories. This can be accomplished for integrable systems through Einstein-Brillouin-Keller quantization [11]. For fully chaotic systems a relationship between the complete quantum eigenvalue spectrum and the set of all (unstable) periodic orbits has been established with the Gutzwiller Trace Formula [12]. The phenomenon of scarring, in which quantum eigenstates appear to have probability peaks associated with classical periodic orbits, seems to demonstrate a connection between periodic orbits and the structure of quantum wavefunctions as well [13]. Another goal of this work is to investigate the relationship between periodic orbits and quantum eigenstates. In particular, we wish to study the way that this relationship changes as the system undergoes a transition from regular to chaotic behavior.

To investigate these aspects of the quantum-classical correspondence, we choose to study one-dimensional potential wells driven by a strong periodic force. This choice is motivated by the recent development of pulsed lasers with extremely high intensities. The electric field generated by these lasers is comparable to the

electric fields generated within an atom by the atomic nucleus. This leads to a number of interesting effects that are not predicted by perturbation theory, such as above-threshold ionization [14], high harmonic generation [15] and atomic stabilization [16, 17]. Simple one-dimensional models have been shown to reproduce much of the interesting behavior of strongly driven systems [18]. Furthermore, the classical dynamics of these model systems becomes chaotic as the strength of the field is increased, so by studying these systems we not only gain insight into quantum-classical correspondence but also gain an understanding of the dynamics underlying these new phenomena.

We begin our investigation of these systems in Chapter 2 by introducing a simple model that consists of an infinite square well driven by a periodic field. We examine the structure of the quantum eigenstates of this system and relate these eigenstates to particular regions of the classical phase space. The radiation spectrum produced by this system is influenced by the structure of these eigenstates and we show how some properties of the spectrum, such as the cutoff in the generation of high harmonics, is ultimately determined by the classical dynamics. We also examine how avoided crossings in the eigenvalue spectrum of this system can result in population transfer as the strength of the driving field is ramped up from zero. This population transfer can increase the high harmonic generation in the system.

In Chapter 3 we carry out a more detailed study of the avoided crossings in

the system introduced in Ch. 2. In particular, we examine how the structure of the quantum eigenstates changes as the system passes through an avoided crossing in the eigenvalue spectrum. We examine two types of avoided crossings: an isolated (or sharp) avoided crossing in which only two states are involved, and an overlapping (or broad) avoided crossing in which more than two states are involved. Overlapping avoided crossings have a profound effect on the structure of quantum eigenstates, while isolated crossings have only a transient effect. We also investigate how these structural changes lead to changes in the radiation spectra produced by individual quantum eigenstates.

The same system is studied in Chapter 4, but in this chapter we are concerned with how the quantum system as a whole changes when the strength of the driving field is increased. We use the concept of information entropy as a measure of the localization of a quantum state, and we illustrate how overlapping avoided crossings lead to an overall increase of entropy in the system. There are a few states, though, that persist in being localized even at relatively high field strengths. We examine the classical dynamics that underlies this localization. At the end of Chapter 4 we discuss the relationships between avoided crossings, localization, and changes in eigenvalue statistics in order to present a unified picture of the evolution of this type of quantum system as the corresponding classical dynamics changes from regular to chaotic.

We extend our analysis to open systems in Chapter 5 through the use of complex scaling techniques. The system we study consists of an inverted Gaussian potential driven by a periodic field. This system shows an increase in the number of quasibound states as the field strength is increased. This phenomenon may be related to atomic stabilization, and we show that it is the result of the scarring of the quasibound states on periodic orbits of the classical system. We end this chapter by closely investigating the structure of two quasibound states as they pass through avoided crossing with each other.

In Chapter 6 we present another simple open system, the time-periodic Rosen-Morse system. The number of quasibound states in this system decreases as the field strength is increased. We examine the phase space structure of these states as they are destroyed and show that their destruction is the result of strong coupling to the continuum. This strong coupling to the continuum is related to resonant photon absorption. We end this chapter by examining the structure of a quasibound states as they pass through an avoided crossings with the continuum.

In Chapter 7 we will summarize our findings and discuss how they are related to each other and to the general problem of “quantum chaos”. This conclusion is followed by three short appendices discussing Floquet theory, Husimi distributions, and the relationship between the length and radiation gauges.

Chapter 2

Harmonic generation in the driven square well

In this chapter we will examine the Floquet eigenstates (see Appendix A) of a quantum system to determine how they are related to the classical dynamics of the corresponding classical system. The model we will use to carry out this study is that of a particle confined to an infinitely deep square well and driven by a time-periodic field. We choose this model because it is representative of a class of systems whose potential is of the form $V(x) = x^{2n}$ for $n \geq 2$ (it is the $n \rightarrow \infty$ limit of this form). Any classical system of this type will develop non-linear resonances at low energies when it is driven by a periodic force. These resonances can overlap and create a region of chaos that is bounded from above [19, 20]. The quantum versions

of these systems also have features corresponding to classical non-linear resonances [21]. These structures have important effects on the radiation spectra of the system.

This model may also be relevant to recent experiments [22]. In particular, the infinite square well serves as a simple model for recent experiments on electron confinement in GaAs/Al_xGa_{1-x}As quantum wells [23, 24]. These experiments confine electrons in wells that vary in width from 50 to 1000 Å and in depth from 200 to 300 meV. A well with a width of only 50 Å and a depth of 300 meV contains only a few bound states and therefore cannot be expected to produce the effects seen in this study. However, a well with a depth of 300 meV and a width of 600 Å contains about 50 bound states. The dynamics of such a well, driven by a far-infrared laser at low intensity, should be similar to the dynamics of our model. The parameters we use roughly correspond to a laser with a wavelength of 400 μm and intensity of about 10⁵W/cm² striking a 600 Å well with a depth of 300 meV. These parameters are well within the range accessible by recent experiments.

2.1 Dynamics of the Driven Square Well

2.1.1 Classical dynamics

The Hamiltonian for the driven square well is:

$$\tilde{H} = \frac{\tilde{p}^2}{2m} + \tilde{\epsilon}\tilde{x} \cos \tilde{\omega}_0\tilde{t}, \quad |\tilde{x}| \leq a, \quad (2.1)$$

where m is the mass, \tilde{p} is the momentum, and \tilde{x} is the position of the particle. The width of the square well is $2a$. The driving field has amplitude $\tilde{\epsilon}$ and frequency $\tilde{\omega}_0$, with \tilde{t} as the time coordinate. This Hamiltonian can be made dimensionless using the scaling transformation introduced in [19], where $\tilde{H} = Hc$, $\tilde{x} = xa$, $\tilde{p} = p\sqrt{2mc}$, $\tilde{\epsilon} = \epsilon \frac{c}{a}$, $\tilde{t} = ta\sqrt{\frac{2m}{c}}$, and $\tilde{\omega}_0 = \omega_0 \frac{1}{a}\sqrt{\frac{c}{2m}}$. This transformation introduces an arbitrary unit of energy c . The scaled Hamiltonian (in units of c) is:

$$H = p^2 + \epsilon x \cos \omega_0 t, \quad |x| \leq 1 \quad (2.2)$$

where all quantities are now dimensionless.

Note that ϵ and ω_0 are not independent parameters, since the transformation $(\omega_0, \epsilon) \rightarrow (\omega_0\sqrt{c}, \epsilon c)$ produces the same dynamics (with a rescaling of the energy unit c). Because of this scaling law we can choose an arbitrary ω_0 , study the dynamics as a function of ϵ , and effectively analyze the dynamics for any set of (ω_0, ϵ) . In this paper we choose $\omega_0 = 80$. Figure 2.1 shows strobe plots of this system (in action-angle variables) for $\epsilon = 50, 320$, and 1600 .

The action and angle variables for this system are defined by $J = 2|p|/\pi$ and $\theta = \pi \text{sign}(p)(x+1)/2$. Rewriting the Hamiltonian using these action-angle variables we find,

$$H = \frac{\pi^2 J^2}{4} - \frac{4\epsilon}{\pi^2} \sum_{\substack{n=-\infty \\ n \text{ odd}}}^{\infty} \frac{1}{n^2} \cos(n\theta - \omega_0 t). \quad (2.3)$$

Writing the Hamiltonian in this way reveals that the driving field induces an infinite series of non-linear pendulum-like resonances in the classical phase space. The

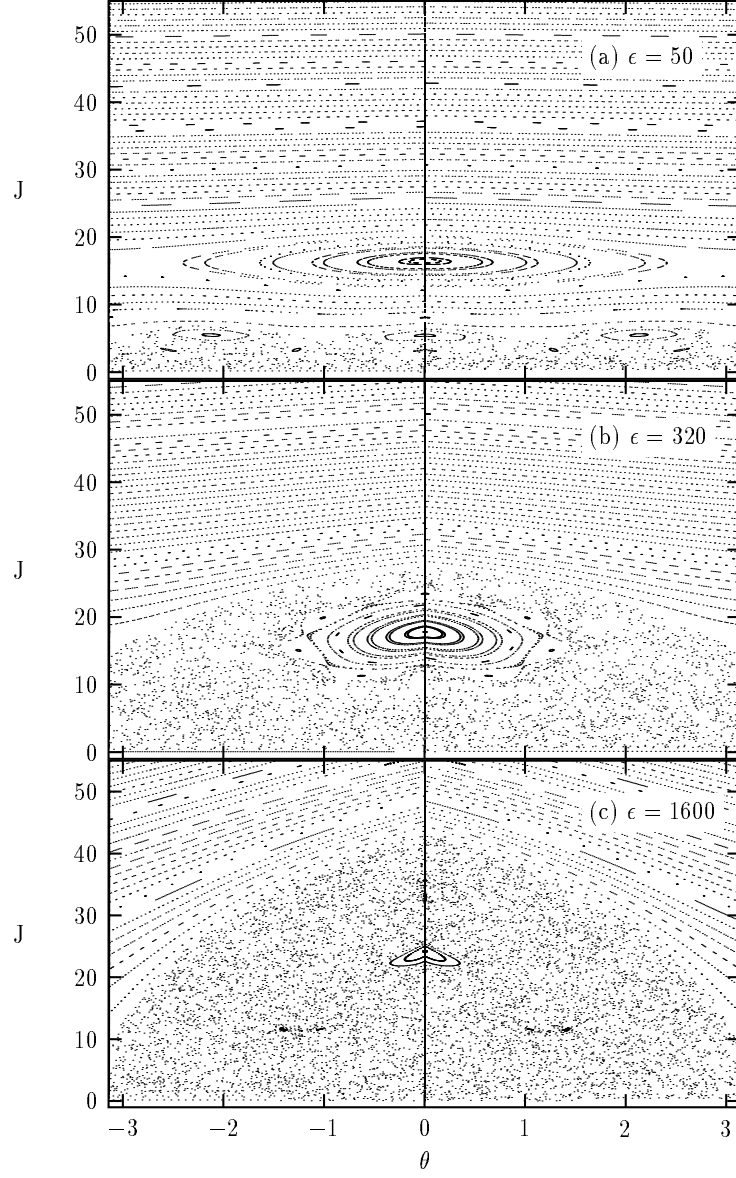


Figure 2.1: Strobe plots of the classical phase space for the driven square well. Primary resonances overlap and form a bounded region of chaos as ϵ is increased. The $M = 1$ primary resonance is the large elliptical feature at $J = 16$ in the first two plots. The line at $\theta = 0$ indicates the presence of a hard wall ($\theta = 0 \leftrightarrow x = -1$).

primary resonances occur at values of the action variable given by $J_c^M = 2\omega_0/(M\pi^2)$. The width of each primary resonance can be derived by approximating the motion in each resonance region as the motion of a pendulum and finding the width of the pendulum's separatrix. This gives

$$\Delta J_M = \frac{4\sqrt{2\epsilon}}{M\pi^2}. \quad (2.4)$$

From these equations we see that two neighboring resonances will overlap when $J_M - J_{M+2} = \Delta J_M + \Delta J_{M+2}$. This is the well-known Chirikov overlap criterion [25]. From this we find that the critical field strength at which the M and $M + 2$ resonances overlap is given by

$$\epsilon_M^c = \frac{\omega_0^2}{(2M+2)^2}. \quad (2.5)$$

When resonances overlap, motion in the region of phase space in which the overlap occurs will become chaotic. Because all high-order resonances occur at very low values of the action, widespread chaos will occur in this system only when the two highest energy resonances (the $M = 1$ and $M = 3$ resonances) overlap. According to the Chirikov criterion this should occur around $\epsilon = 200$. However, the Chirikov overlap criterion is known to overestimate the field strength needed to produce chaos, so widespread chaos may occur at field strengths less than $\epsilon = 200$.

We will now examine some strob plots of the classical motion in this system for three different values of ϵ . These strob plots are shown in Figure 2.1. The

$M = 1$ resonance is apparent in all of the strobe plots in Figure 2.1. The $M = 3$ resonance is visible only in the $\epsilon = 50$ plot. For $\epsilon = 320$ and 1600 all of the primary resonances have overlapped and all but the $M = 1$ resonance have been destroyed. Note that the $M = 1$ resonance cannot overlap with any higher energy primary resonances because there are no primary resonances with a higher energy. Thus, for very high values of J the phase space will remain regular at all field strengths. This leads to “bounded chaos” in the system. We will show that this structure has a profound effect on the dynamics of the corresponding quantum system.

2.1.2 Quantum dynamics

The Schrödinger equation for a driven particle in an infinite square well is given by

$$i\hbar \frac{\partial}{\partial \tilde{t}} |\psi(\tilde{t})\rangle = -\frac{\hbar^2}{2m} \frac{\partial^2}{\partial \tilde{x}^2} + \tilde{\epsilon} \xi(t) \tilde{x} \cos(\tilde{\omega}_0 \tilde{t}) \quad (2.6)$$

where $|\tilde{x}| \leq a$. All parameters are defined as in the classical Hamiltonian above, except $\xi(t)$ which is the turn-on function for the laser field. The transformation to dimensionless coordinates is identical to that used for the classical Hamiltonian, except that instead of scaling \tilde{p} we must scale \hbar . The resulting dimensionless equation is

$$i\kappa \frac{\partial}{\partial t} |\psi(t)\rangle = \left(-\kappa^2 \frac{\partial^2}{\partial x^2} + \epsilon \xi(t) x \cos(\omega_0 t) \right) |\psi(t)\rangle \quad (2.7)$$

where energy is measured in units of c (as in the classical case) and $\kappa = \hbar/(a\sqrt{2mc})$.

Note that in the quantum system there are three parameters: ϵ , ω_0 , and κ . Only

two of these parameters are independent, so the full dynamics of this system can be studied by varying two parameters. In this paper we will only vary one of the parameters, ϵ , and we set $\kappa = 1$ and $\omega_0 = 80$ as above. The effect of varying κ is left for future study.

We will use the eigenstates of the undriven infinite square well to analyze the Schrödinger Equation for this system. The Hamiltonian for the undriven infinite square well is $H_0 = p^2$, where $|x| \leq 1$. The boundary conditions for the eigenstates of H_0 are $\psi(-1, t) = \psi(1, t) = 0$ where $\psi(x, t) = \langle x | \psi(t) \rangle$. The energy eigenvalues of H_0 are

$$E_n = \frac{\pi^2 \kappa^2 n^2}{4}, \quad n = 1, 2, \dots \quad (2.8)$$

and the corresponding wavefunctions are given by

$$\psi_n(x) = \langle x | E_n \rangle = \sin\left(\frac{\pi n(x-1)}{2}\right) \quad (2.9)$$

where $|E_n\rangle$ represents the eigenstate whose eigenvalue is E_n . The dipole matrix elements for these eigenstates are

$$x_{nm} = \begin{cases} 0, & [m+n] \pmod{2} = 0 \\ \frac{16mn}{\pi^2(m^2-n^2)^2}, & [m+n] \pmod{2} = 1 \end{cases} \quad (2.10)$$

where $(\text{mod } 2)$ stands for “modulo 2”. This form is very convenient for numerical calculations.

Writing the wavefunction in the energy basis ($|\psi(t)\rangle = \sum_i c_i(t) |E_i\rangle$), one can convert the Schrödinger Equation into a system of ordinary differential equations

for the c_i 's:

$$\frac{dc_i(t)}{dt} = -\frac{iE_i}{\kappa}c_i(t) + \frac{i}{\kappa}\epsilon\xi(t)\cos(\omega_0 t)\sum_j x_{ij}c_j(t). \quad (2.11)$$

This system can be numerically solved for any initial condition. The radiation spectrum is simply the Fourier transform of the acceleration, and the acceleration time series is given by

$$\langle\psi(t)|\ddot{x}|\psi(t)\rangle = \sum_{ij} c_j^*(t)\ddot{x}_{ji}c_i(t) \quad (2.12)$$

where

$$\begin{aligned} \ddot{x}_{ji} = & -\frac{1}{\kappa^2}(E_j - E_i)^2 x_{ji} \\ & + \frac{1}{\kappa^2}\epsilon\xi(t)\cos(\omega_0 t)\sum_k (2E_k - E_j - E_i)x_{jk}x_{ki} \end{aligned} \quad (2.13)$$

is the “acceleration matrix element”.

We use a basis of the first 80 eigenstates of H_0 , which extends well into the regular region for all of the field strengths we will consider. All spectra were calculated using 128 cycles of the field after the end of the initial turn-on period. Note that since parity is a good quantum number for this system there will be no radiation at even harmonics of the driving field.

2.2 Radiation Spectra

In time periodic quantum systems the radiation spectrum is determined by which Floquet states (see App. A) are excited. Certain superpositions of Floquet states

can lead to high harmonic generation while other superpositions produce no high harmonics. To illustrate how a superposition can lead to efficient high harmonic generation we will briefly examine the radiation spectrum from a superposition of two Floquet states, one localized at high energy and the other at low energy. Husimi plots of these states are shown in Fig. 2.2. We will write the wavefunction of the superposition as

$$|\psi(t)\rangle = a_\alpha e^{-i\Omega_\alpha t} |\Omega_\alpha(t)\rangle + a_\beta e^{-i\Omega_\beta t} |\Omega_\beta(t)\rangle, \quad (2.14)$$

where $|a_\alpha|^2 + |a_\beta|^2 = 1$ and $|\Omega(t)\rangle = |\Omega(t+T)\rangle$.

The time-dependent dipole expectation value for this superposition is

$$\begin{aligned} \langle \psi(t) | x | \psi(t) \rangle &= |a_\alpha|^2 \langle \Omega_\alpha(t) | x | \Omega_\alpha(t) \rangle + |a_\beta|^2 \langle \Omega_\beta(t) | x | \Omega_\beta(t) \rangle \\ &\quad + a_\alpha^* a_\beta e^{i(\Omega_\alpha - \Omega_\beta)t} \langle \Omega_\alpha(t) | x | \Omega_\beta(t) \rangle \\ &\quad + a_\beta^* a_\alpha e^{i(\Omega_\beta - \Omega_\alpha)t} \langle \Omega_\beta(t) | x | \Omega_\alpha(t) \rangle. \end{aligned} \quad (2.15)$$

Each Floquet state can be written as a time-dependent superposition of unperturbed energy eigenstates such that

$$e^{-i\Omega_\alpha t} |\Omega_\alpha(t)\rangle = \sum_j c_{j\alpha}(t) e^{-iE_j t} |E_j\rangle \quad (2.16)$$

and

$$e^{i(\Omega_\alpha - \Omega_\beta)t} \langle \Omega_\alpha(t) | x | \Omega_\beta(t) \rangle = \sum_{j,k} c_{j\alpha}^*(t) c_{k\beta}(t) e^{i(E_j - E_k)t} \langle E_j | x | E_k \rangle. \quad (2.17)$$

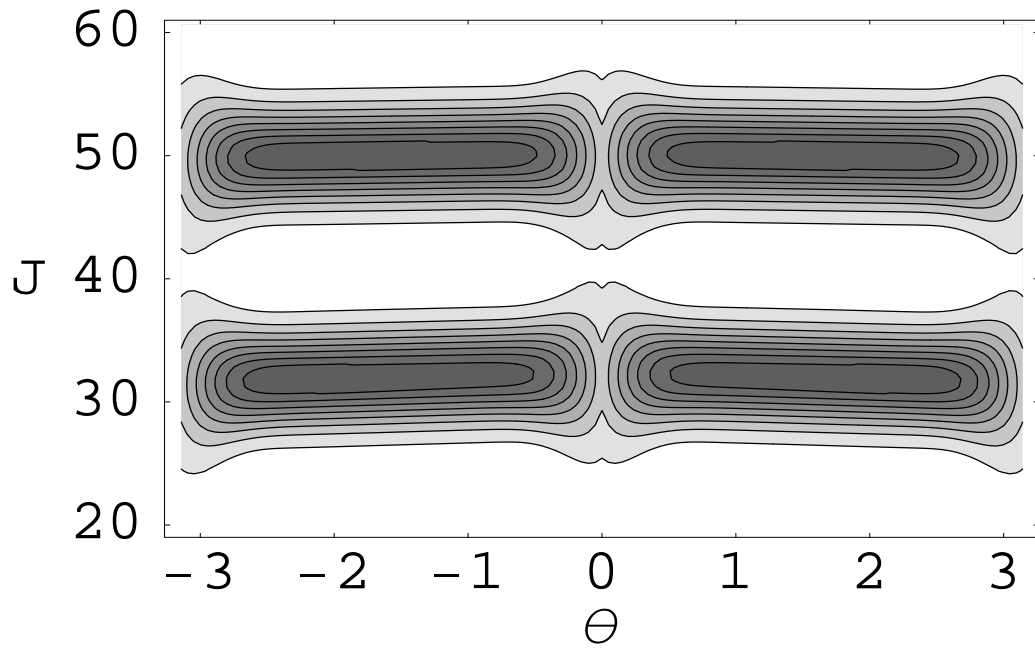


Figure 2.2: Husimi plot showing the two states in the superposition. $|\Omega_{32}\rangle$ is primarily composed of the $n = 32$ energy eigenstate, while $|\Omega_{50}\rangle$ is composed mainly of $n = 50$.

The first two terms in (2.15) correspond to the dipole value if the system was in a single Floquet state, $|\Omega_\alpha(t)\rangle$ or $|\Omega_\beta(t)\rangle$. If we set $\beta = \alpha$ in (2.17), we can see from the left-hand side of that equation that a single Floquet state radiates only at the harmonics of the driving field, because $\langle\Omega_\alpha(t)|x|\Omega_\alpha(t)\rangle$ is a periodic function with period T . Looking at the right-hand side of (2.17) shows that the range of harmonics at which a Floquet state will radiate is determined by the range of unperturbed energy eigenstates over which that Floquet state has support, provided only that the $c_{j\alpha}(t)$'s are weakly time dependent (which is the case for Floquet states in this system). If the Floquet state is spread over a wide range of energies, then these terms can contribute HHG. If the Floquet state is confined to a narrow band of energies there will be no HHG. Figure 2.2 shows two Floquet states that lie in the regular region of the phase space for the driven square well at $\epsilon = 50$. Radiation spectra for each of these states are shown in Figs. 2.3a and 2.3b. It is clear that, as predicted, these states do not generate high harmonics.

The last two terms in (2.15) are cross terms that correspond to transitions between the two Floquet states. Transitions between Floquet states give rise to radiation at frequencies $n\omega_0 \pm (\Omega_\alpha - \Omega_\beta)$. If the two Floquet states have support on widely separated sets of energy eigenstates, then these terms can lead to HHG (at shifted harmonics). An example of this is shown in Fig. 2.3c, which shows the radiation spectrum for a superposition of the two states shown in Fig. 2.2. Note that one

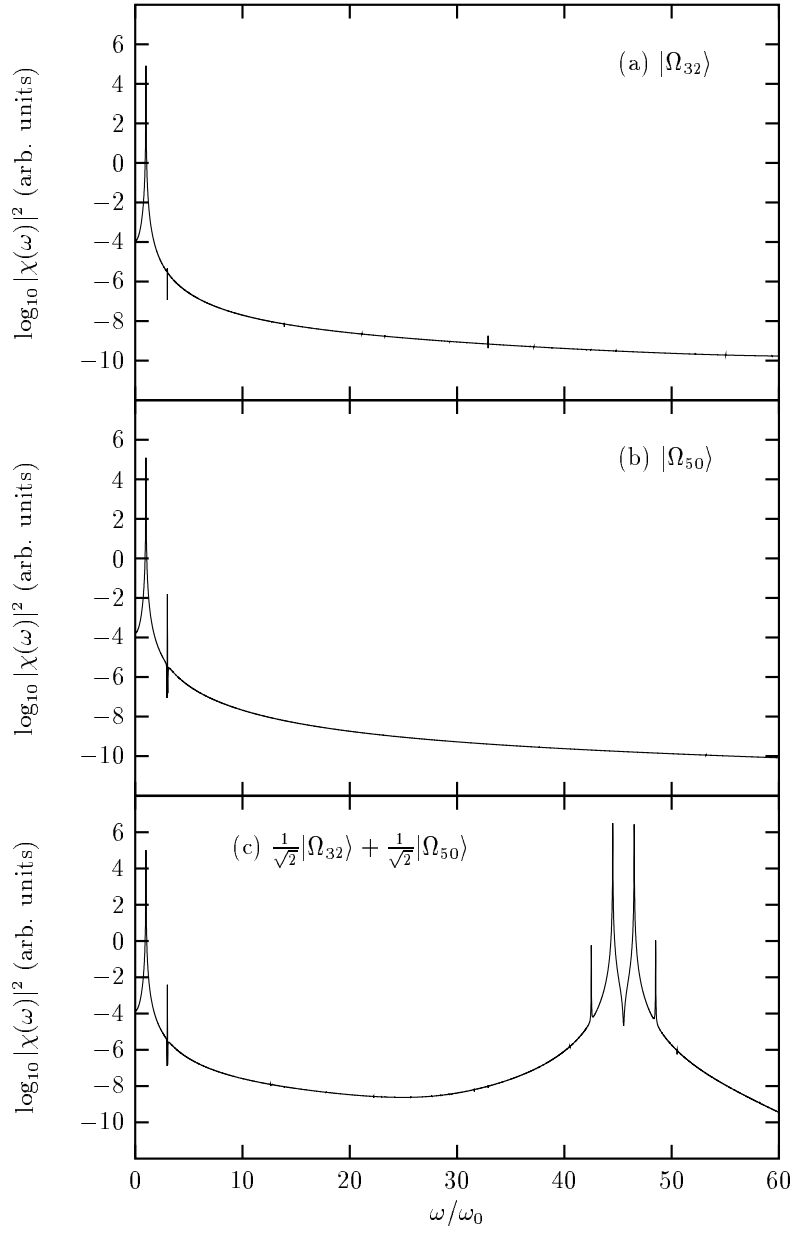


Figure 2.3: Spectra for (a,b) individual Floquet states and for (c) a superposition of two states. The location of the cluster of peaks in (c) is determined by the separation in energy of the Husimi distributions in Fig. 2.2.

of these Floquet states has most of its support on the $n = 32$ energy eigenstate and the other Floquet state is concentrated near $n = 50$. We expect the superposition to radiate at frequencies corresponding to the difference in these energies. For $\omega_0 = 80$ this is near the 45^{th} harmonic, which is exactly where the cluster of peaks in Fig. 2.3c appears. The width of this cluster is determined by the range of energies over which the two Floquet states have support. Close inspection of the peaks in Fig. 2.3c shows that they are all shifted by 0.477 from the odd harmonics. This agrees with our expectations since the difference in the quasienergies of the two Floquet states (divided by ω_0) is $(\Omega_{32} - \Omega_{50})/80 = (46.712 - 8.526)/80 = 0.477$.

The preceding example is artificial in the sense that the superposition of Floquet states that was used is not one that could arise naturally in our system. We will now examine what happens when our system, initially in a single eigenstate of the undriven quantum square well, is subjected to a driving field. The driving field will turn on slowly until its maximum field strength, ϵ , is achieved. We examine the harmonic generation in this system for two values of the maximum field strength. At each field strength we calculate the radiation spectrum, and Floquet composition at the end of the turn-on, for several initial states.

2.2.1 Strong field

The classical phase space for field strength $\epsilon = 320$ is chaotic for actions less than about 25. However, in the middle of this chaotic sea there is a prominent resonance from 12 to 22 in action, and about -1 to 1 in angle. Above $J = 25$ the phase space is regular.

We compute the radiation spectrum of the quantum system for three different initial conditions, $n = 3$, $n = 16$, and $n = 35$. This allows us to study the quantum behavior for states that sit in the chaotic, resonance, and regular regions of the classical phase space. For this field strength we use a 12 cycle turn-on. The radiation spectrum for each initial condition is shown in Figure 2.4.

For initial state $n = 35$ we see that there is no high harmonic generation. The radiation spectrum is typical of what we might find using perturbation theory at weak field strengths. Nearly all radiation occurs at the fundamental frequency ω_0 . After computing the Floquet eigenstates for this field strength we can decompose the wavefunction at the end of the laser turn-on in the Floquet basis. For initial state $n = 35$ we find that only one Floquet state is excited at the end of the turn-on. The Husimi distribution (see Appendix B) of that Floquet state is shown in Figure 2.5a. (Note that this and all Husimi distributions for this system should go to zero at $\theta = 0$ since this corresponds to $x = -1$. Because of the smoothing involved in creating the Husimi distribution there appears to be nonzero probability

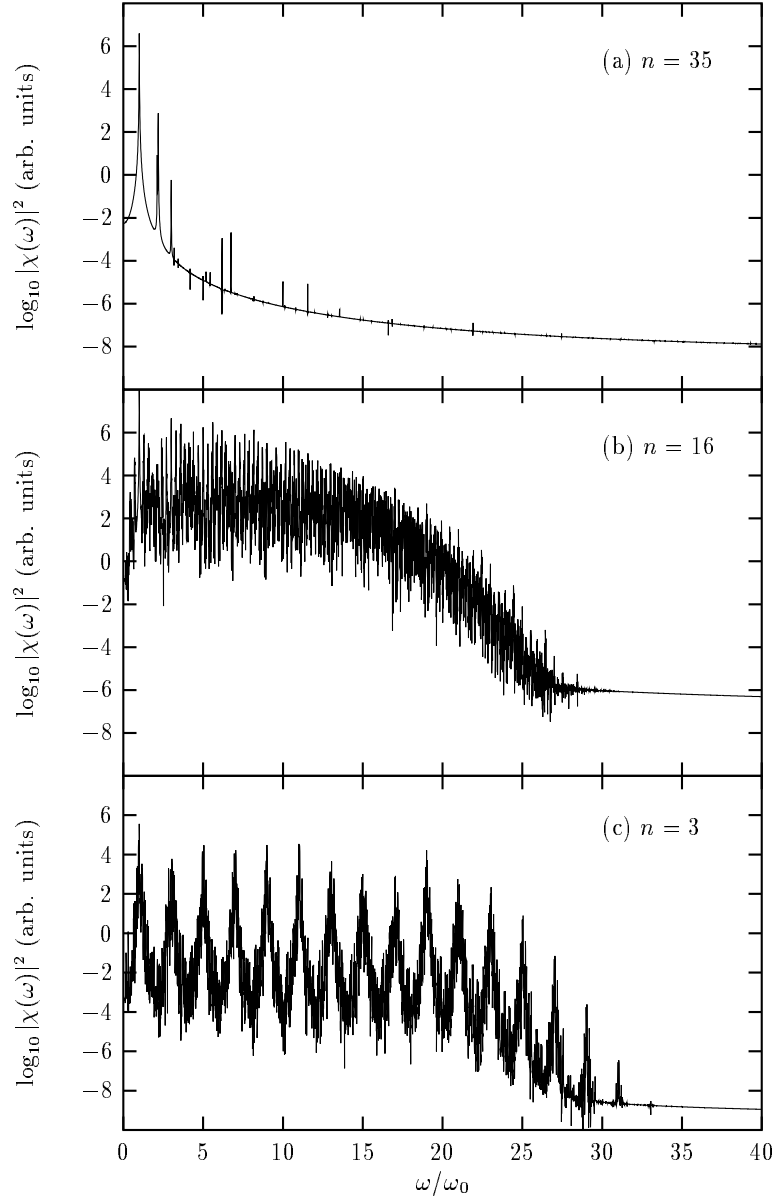


Figure 2.4: Spectra for the driven square well at $\epsilon = 320$. These three spectra are typical for initial conditions starting in the three regions of classical phase space: (a) regular, (b) resonance, and (c) chaotic. The cutoffs for (b) and (c) are determined by the range of energies a classical particle in each region can sample.

at $\theta = 0$ even though the *wavefunction* goes to zero there.) It is clear that the Husimi distribution closely follows the invariant tori that appear in the regular part of the classical phase space. We will call such a state a “regular” Floquet state. These states are typically excited for initial conditions that begin in the regular part of the classical phase space. Since these states produce no HHG, this region will be of little interest to us here.

For initial state $n = 16$ the radiation spectrum (Figure 2.4b) is quite different. There does appear to be a plateau in the spectrum running out to about the 11th harmonic. However, the harmonic peaks do not show up clearly. There are a number of additional peaks (shifted harmonics) that make the spectrum very messy. At the end of the turn-on only about 13 Floquet states are excited above the level of 0.1%. As discussed earlier, this leads to shifted harmonics because the system can radiate at frequencies $n\omega_0 + (\Omega_\alpha - \Omega_\beta)$, where Ω_α and Ω_β are quasienergies associated with the excited Floquet states. If N Floquet states are excited there will be $(N - 1)!$ possible values of $(\Omega_\alpha - \Omega_\beta)$. For 13 states this means nearly 10^9 possible shifted peaks for each harmonic! It should be noted, however, that 80% of the probability lies in three Floquet states. The Husimi distributions for these Floquet states are shown in Figure 2.5(b-d). These three states are all localized within the primary resonance.

Now for initial state $n = 3$ we see from Figure 2.4c that there is strong

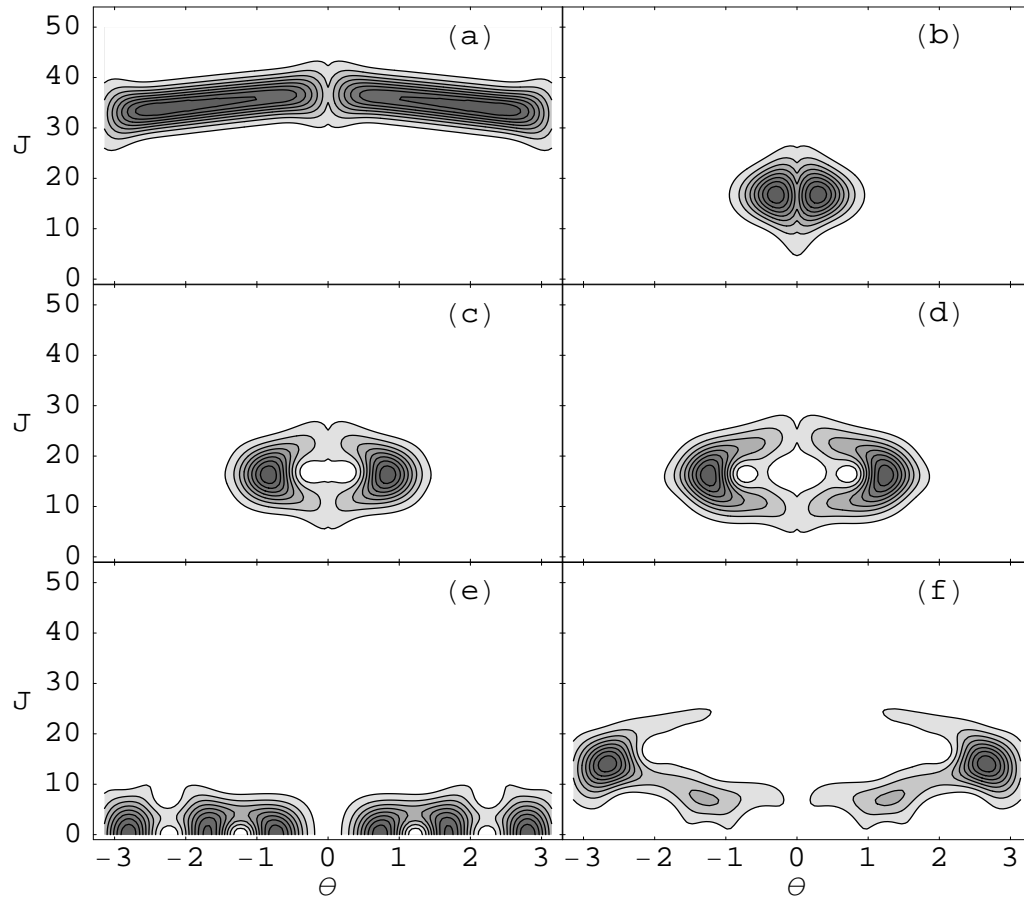


Figure 2.5: Husimi plots of Floquet states for the driven square well at $\epsilon = 320$. Each state can be associated with a particular region of the classical phase space: (a) regular, (b-d) resonance, and (e,f) chaotic.

harmonic generation. The cutoff in the spectrum appears to be at about the 19th harmonic. There are a few shifted peaks, but not so many as to obscure the harmonic peaks. At the end of the turn-on there are two Floquet states that are significantly excited. We see that the Husimi distributions of these Floquet states, shown in Figures 2.5e and 2.5f, are concentrated in the chaotic region of the classical phase space. One of these is localized near $J = 0$ (the bottom of the well) while the other is localized near the unstable fixed point at $J \approx 15$. This combination gives the quantum system access to energies spanning the chaotic region.

For the combination of Floquet states arising from $n = 3$, one would expect transitions to occur whose energy difference is equal to the energy range of the chaotic region ($\Delta E = \pi^2(25^2 - 0^2)/4 = 1542$) or less. So the cutoff in the harmonic generation should occur at $\Delta E/\omega_0 = 1542/80 \approx 19$, which is exactly what we see in Figure 2.4c. For the “resonance” Floquet states arising from $n = 16$ one would expect the cutoff to be given by the energy range of the resonance divided by ω_0 . We find $\Delta E_{res} = \pi^2(22^2 - 12^2)/4 = 839$ and $\Delta E_{res}/\Omega = 839/80 \approx 10.5$ which again fits the spectrum in Figure 2.4b.

2.2.2 Very strong field

At a field strength of $\epsilon = 1600$ the classical phase space is chaotic below $J = 40$, as seen in Figure 2.1c. There is a small resonance still present near $J = 22$, as well as

some tiny secondary resonances, but all of these structures are small compared to κ (the effective \hbar) in the quantum system. We cannot expect these structures to have an impact on the quantum dynamics of the system. Above $J = 40$ the phase space is regular.

We study this field strength using initial conditions $n = 3$ and $n = 22$. We omit the results for $n > 40$ because they are identical to the “regular” results for $\epsilon = 320$ (see Figures 2.4a, 2.5a). The turn-on for this field strength is 60 cycles, which gives the same adiabaticity as the 12 cycle turn on for $\epsilon = 320$.

Starting off in $n = 3$ we find the spectrum shown in Figure 2.6a. At low frequencies the radiation spectrum resembles “white noise”. This is because of the large number of shifted peaks which wash out the harmonics. The system passes through many avoided crossings (see Sec. 2.3) during the turn-on, resulting in the excitation of many Floquet states. There appears to be a cutoff at about the 50th harmonic. We show the Husimi distributions of two of these Floquet states in Figures 2.7a and 2.7b. While the state shown in 2.7a appears to be concentrated near the location of the small resonance (although certainly not inside it), the state in 2.7b is spread throughout the chaotic region. This is somewhat different from the localized “chaotic” Floquet states at $\epsilon = 320$. However, at this higher field strength it is typical for the “chaotic” Floquet states to fill the chaotic region. This delocalization occurs for Floquet states that have passed through many avoided

crossings (see Chapter 3). Again we see that the size of the chaotic region determines the cutoff as $\Delta E = \pi^2(40^2 - 0)/4 = 3948$ and $\Delta E/\omega_0 = 3948/80 \approx 49$, which agrees well with what we see in the spectrum.

At $n = 22$ we are close to the energy of the small resonance. However, we see that the spectrum for this initial condition (Figure 2.6b) looks very similar to the one for $n = 3$. Again we find that there are many Floquet states populated. Husimi plots for two of these are shown in Figures 2.7c and 2.7d. It is clear that these states are *not* concentrated inside the small resonance. This is because the resonance is small compared to the size of κ in our calculations. The quantum system effectively ignores the presence of the resonance. Instead, the system populates delocalized “chaotic” Floquet states, as for $n = 3$. Again, the cutoff matches the energy range of the chaotic region.

2.2.3 General properties

From the above analysis we derive some basic properties of the radiation spectrum for this system. First, states that start out in a regular region of the classical phase space will remain localized in this region. They will typically only excite a single Floquet state whose Husimi distribution is concentrated around a classical invariant torus. Such a state will produce no HHG.

A state initially inside a large (relative to κ) resonance will typically excite

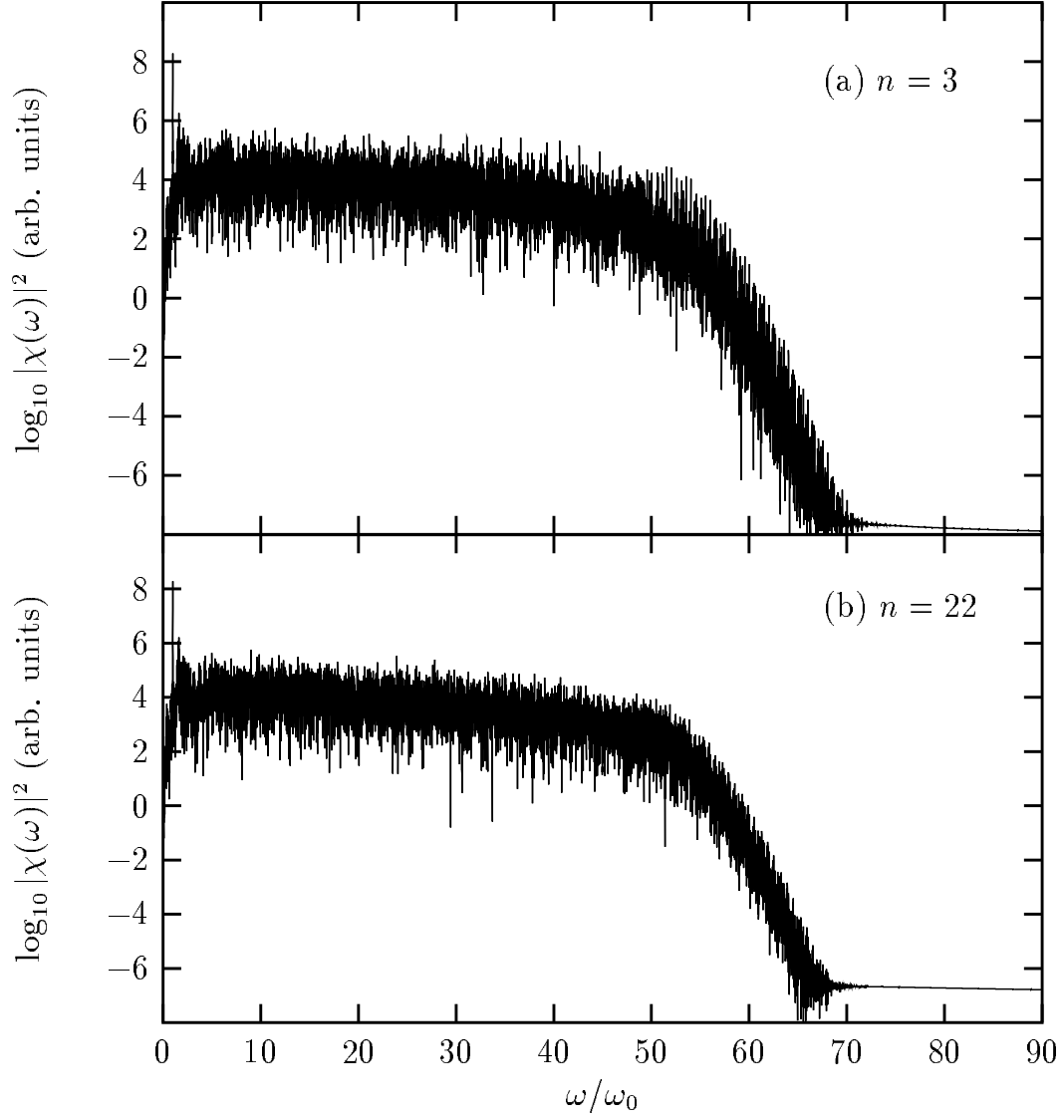


Figure 2.6: Spectra for the driven square well at $\epsilon = 1600$. Although (b) starts off in the resonance region, the resonance at this field strength is too small to influence the quantum dynamics. The cutoffs for both spectra are given by the energy range of the chaotic region.

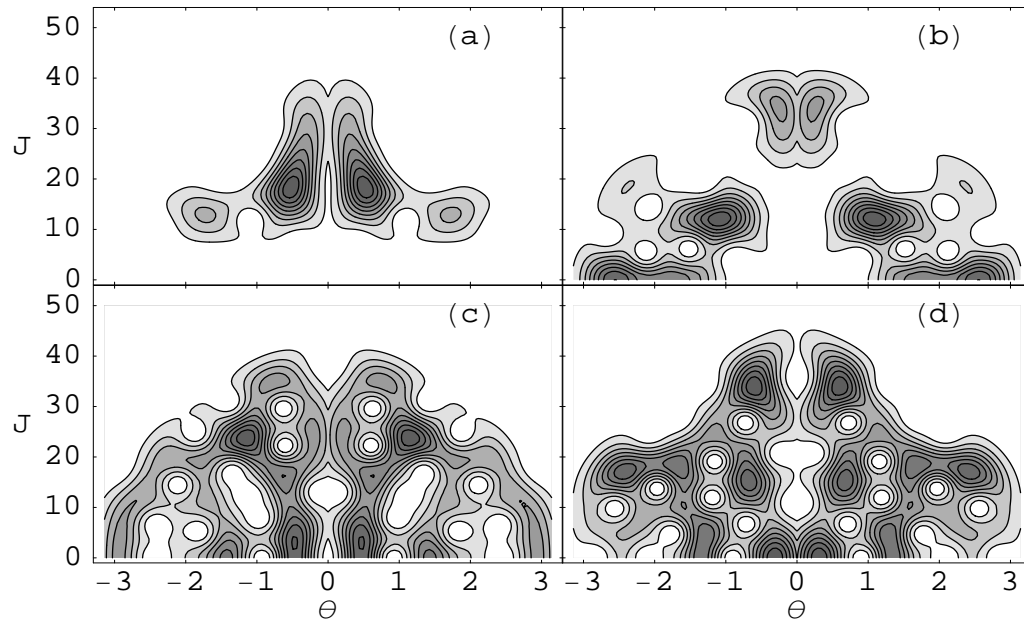


Figure 2.7: Husimi plots for driven square well Floquet states at $\epsilon = 1600$. At this high field strengths the Floquet states broaden to fill the region of chaos.

numerous Floquet states. This large number of Floquet states leads to a noisy spectrum with many shifted peaks. However, most of the probability will be in Floquet states that are localized in or near the resonance region. This leads to a cutoff in the spectrum that is determined by the width (in energy) of the resonance.

An initial condition in the chaotic region will excite “chaotic” Floquet states. At lower field strengths these “chaotic states” seem to be localized near a particular unstable periodic orbit of the classical system. Only a few of these localized states will be excited, which leads to a clean harmonic spectrum. At very high field strengths the “chaotic” Floquet states will have Husimi distributions that fill the chaotic region. These delocalized states have become associated with a large set of periodic orbits of the classical system. This occurs when the system has passed through many avoided crossings during the turn-on. These avoided crossings lead to the excitation of a large number of Floquet states and a white noise radiation spectrum. In either case the cutoff is given by the energy range of the chaos, which can be quite large.

In all of these cases the cutoff in the HHG is determined by the range of energies that the classical particle can sample during its trajectory. This result is in agreement with [26]. It is also similar to other cutoff laws (like those invoking the ponderomotive potential [27] or the Rabi frequency [28]) because the cutoff is just given by the maximum energy that the classical particle can gain from the field. For

a state that is initially in a chaotic region we can predict the cutoff by examining a strobe plot of the classical dynamics. Table 2.1 shows the cutoffs seen in the spectra and the energy range of the chaos seen in the strobe plots. The observed cutoffs follow the strobe plot predictions very closely.

Note that the table includes data from field strengths that are not discussed elsewhere in this paper. The uncertainties in the cutoff values read from the spectra are worse for high field strengths because these spectra tend to be noisy and difficult to read.

2.3 Avoided Crossings

From the above analysis it is clear that the best way to generate high harmonics is to excite chaotic Floquet states. To get sharp peaks at the harmonics (i.e. few shifted harmonics), one should excite as few Floquet states as possible [29]. Ideally one would like to excite a single chaotic Floquet state, but it is nearly impossible to excite only one such state. Another alternative is to excite a superposition of two states that sit at high and low energies, respectively. Avoided crossings in the Floquet spectrum provide the opportunity for transitions between Floquet states [30], and hence a method for engineering a particular combination of Floquet states. A quantum system that is initially in a single Floquet state can transfer some of its probability to another Floquet state during the turn-on of the field if the initial

ϵ	Observed	Strobe
50	9 ± 2	≈ 11
150	15 ± 2	≈ 15
320	19 ± 2	≈ 19
960	35 ± 2	≈ 37
1600	49 ± 4	≈ 49
2560	73 ± 4	≈ 74

Table 2.1: Observed harmonic cutoffs and predictions based on classical strobe plots for several field strengths ϵ . Uncertainties in the observed cutoffs are large for very strong fields because these spectra have many shifted peaks, making them difficult to read.

state has an avoided crossing with another state between $\epsilon = 0$ and the final value of ϵ achieved by the field at the end of the turn-on. This can result in a superposition of Floquet states that covers a broad range of energy, even if the individual Floquet states that compose the superposition are all localized.

We have seen that a superposition of Floquet states that covers a broad range of energy can produce HHG. Now we will examine how such superpositions can be created during the turn-on of the driving field. In Figure 2.8 we plot the quasienergies of our system for field strengths of 0 to 400. Up to the critical field strength for overlap of the two highest energy primary resonances in this system, $\epsilon_1^c = 200$, there are few avoided crossings (where two curves approach, but do not cross each other). However, after this point the avoided crossings arise quickly. At even higher field strengths almost every curve undergoes a rapid succession of many avoided-crossings. The proliferation of avoided crossings is associated with the spread of chaos in the classical system. One of the first avoided crossings occurs at a field strength of $\epsilon \approx 100$. This value of ϵ is less than ϵ_1^c , but as mentioned earlier the value of ϵ_1^c is an overestimate of the field strength that is required to create widespread chaos in the classical phase space [19, 20]. This first avoided crossing involves states connected to $n = 6$ and $n = 10$ (labeled Ω_6 and Ω_{10} in Fig. 2.8). We note that these pairs are symmetric about $n = 8$, because $J = 8$ is precisely where the classical resonances overlap at the critical field strength. This indicates a strong connec-

tion between avoided crossings in the Floquet spectrum and overlap of nonlinear resonances in the classical phase space.

Figure 2.8 shows only the quasienergies of the lowest 40 states in our basis. Using a finite basis to calculate quasienergies always introduces numerical error [31], but for the field strengths shown this error is extremely small. At higher field strengths one would need to use a larger basis to avoid numerical error. Essentially one can avoid numerical error as long as the basis extends well into the regular region of the phase space. Since our calculations use states up to $n = 80$ we will not experience numerical error until the chaotic region comes near $J = 80$, which is not the case for any field strengths we consider here.

It is important to note that there are many places, particularly at small values of ϵ , where the quasienergy curves actually cross. This happens when the two states associated with the curves belong to different (uncoupled) sectors of the Hilbert space and transitions between these states are forbidden [3, 30]. By different sectors of Hilbert space we mean that the two states belong to different blocks of a block-diagonal Hamiltonian, indicating that they belong to different symmetry groups. When ϵ is small these “apparent crossings” are quite common, but at large ϵ there are few apparent crossings. The reason for this is that the spread of chaos is due to the breaking of the same symmetries that prevent coupling of certain states.

Avoided level crossings provide one of the two mechanisms available for pop-

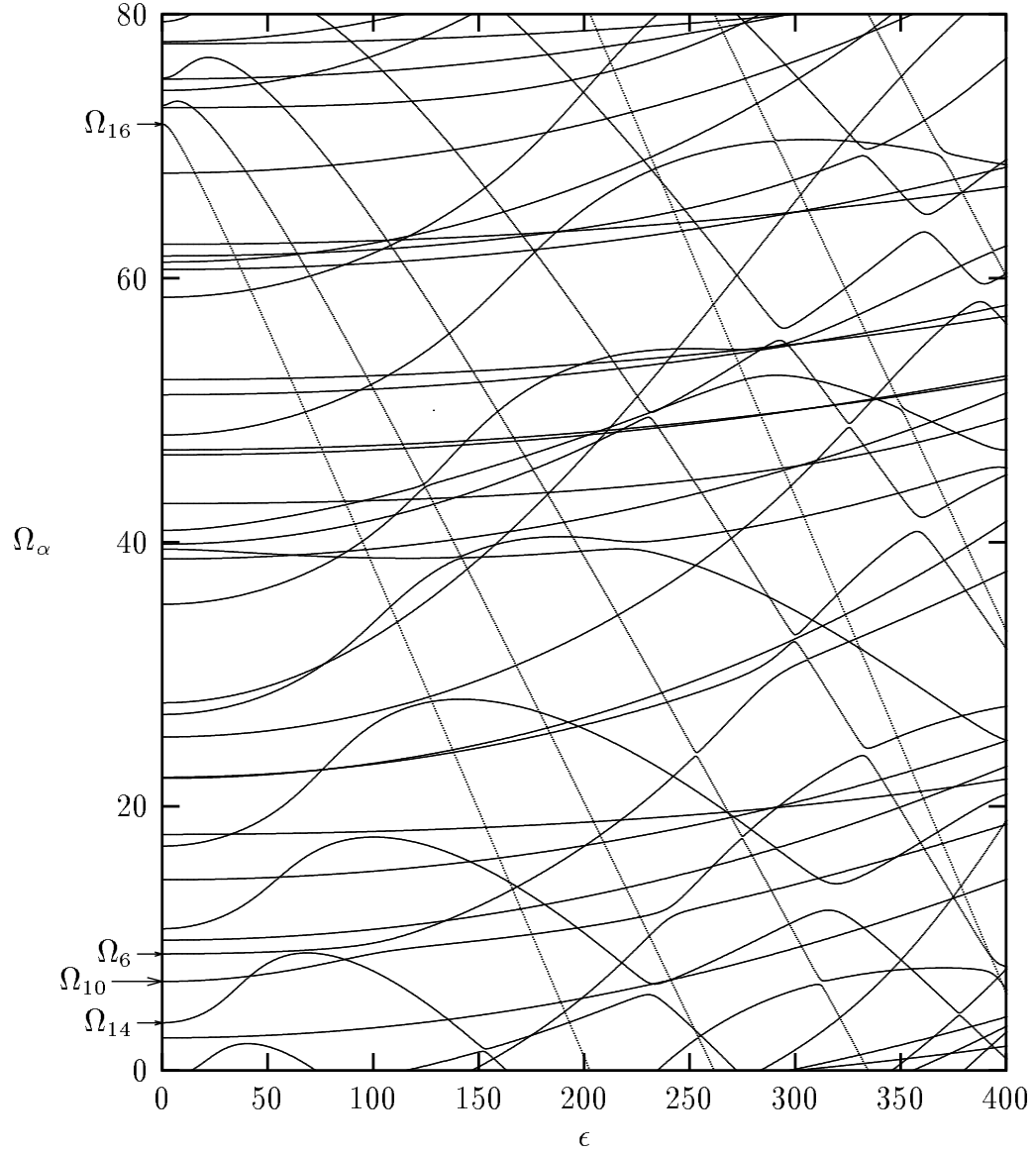


Figure 2.8: Plot of quasienergies as a function of field strength for the driven square well. Curves associated with resonance states (i.e. Ω_{16} and Ω_{14}) resemble eigen-curves of the Mathieu equation [32]. The avoided crossing discussed in the text is between Ω_6 and Ω_{10} at $\epsilon \approx 100$.

ulation transfer between Floquet states. The other mechanism is a non-adiabatic turn-on of the driving field. If the field is turned on rapidly, transitions between Floquet states will be allowed because the Floquet states at one field strength will not be Floquet states at another field strength. A rapidly varying field strength leads to rapid changes in the structure of the Floquet states and thus to transitions between Floquet states. However, if the field is turned on adiabatically the system will remain in the same (continuously connected) Floquet state until it reaches an avoided crossing. We will confine our investigation to population transfer that occurs at the avoided crossing between Ω_6 and Ω_{10} at $\epsilon \approx 100$.

To study this avoided crossing we start with the system in $n = 6$ and investigate the behavior of the system for field strengths below and above the avoided crossing. At $\epsilon = 65$ the state is composed of 98.6% $|\Omega_6\rangle$ and 1.4% $|\Omega_{10}\rangle$ at the end of its turn-on. At $\epsilon = 125$ we are mostly through the avoided crossing and the state is composed of 72.5% $|\Omega_{10}\rangle$ and 27.5% $|\Omega_6\rangle$. Spectra shown in Figure 2.9 show an increase in HHG as the system traverses the avoided crossing. This indicates that population transfer “spreads” the wavefunction over a wider range of energies.

Avoided crossings increase HHG in two ways. The first way is by creating a superposition of Floquet states that occupy different regions of phase space. This superposition will typically be spread over a wide range of energies, which leads to the plateau structure that is observed in the radiation spectra. In the next chapter

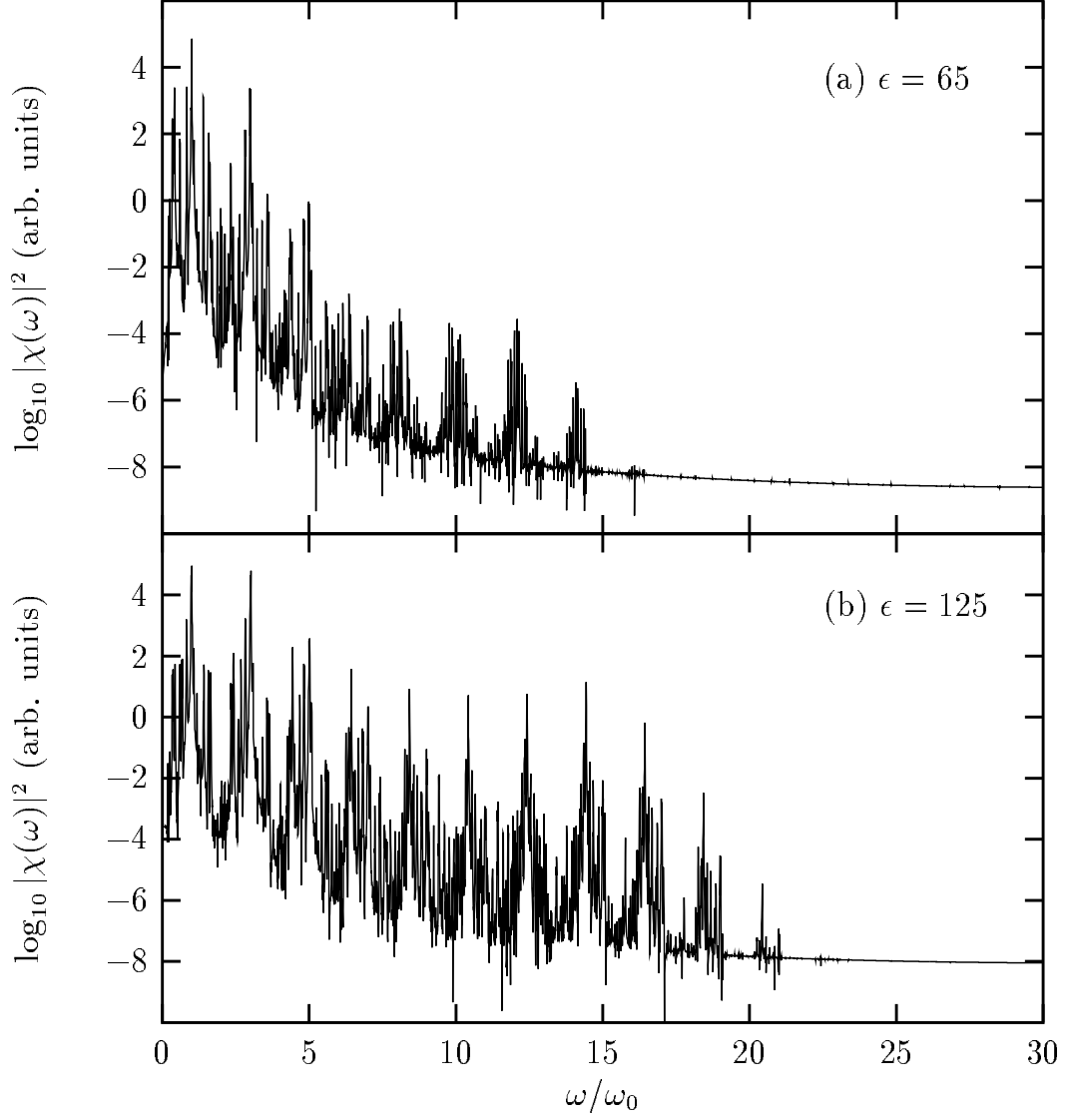


Figure 2.9: Spectra for the driven square well with initial condition $n = 6$. The avoided crossing between Ω_6 and Ω_{10} occurs between these two field strengths. Note the increase in HHG after the system has passed through the avoided crossing.

we will see that avoided crossings are associated with the creation of delocalized states, which also leads to an increase in HHG. After a state passes through many avoided crossings it will lose the close association it had with a single small region of phase space and become associated with a much larger region of phase space. At very high field strengths states are typically spread throughout the chaotic region, which allows these states to radiate at very high harmonics of the driving field.

Chapter 3

Changes in Floquet-state structure at avoided crossings

In the previous chapter we saw that avoided crossings can lead to population transfer during the turn-on of the driving field, creating a superposition of Floquet states that can radiate at high harmonics. In this chapter we will examine avoided crossings in more detail, focusing on how avoided crossings lead to the delocalization of Floquet states. A connection between level repulsion (avoided crossings) and the creation of extended (delocalized) states has already been found [33, 34]. However, these studies look at statistical properties of the system as a whole. Here we will concentrate on the changes in the structure of individual quantum eigenstates at a single avoided crossing. We identify two distinct types of avoided crossings which have different

effects on eigenstate structure. One type of crossing produces significant changes in the eigenstates only for the parameter values at which the avoided crossing actually occurs. The second type results in structural changes that persist for parameter values that are beyond the avoided crossing. Finally, we will investigate what impact these structural changes have on the radiation spectrum of the system.

3.1 Classical and Quantum Dynamics

As in Chapter 2 we will use the driven particle in an infinite square well as our model. Section 2.1 contains a detailed account of the classical and quantum dynamics of this model. However, since the field strengths we use in this chapter are different from those used in Chapter 2, we show two new strobe plots in Figure 3.1. The strobe plots show the classical phase space of our system for $\epsilon = 174$ and $\epsilon = 780$. The most important features of each strobe plot are the bounded region of chaotic motion at low energies, and the $M = 1$ primary resonance which is the elliptical island that lies within the chaotic sea in both strobe plots. Note that at $\epsilon = 780$ the resonance island is distorted and much smaller than at $\epsilon = 174$. As ϵ is increased in this system the chaotic region spreads slowly to higher energies and the resonance island shrinks until it finally disappears.

All of the quantum simulations discussed in this chapter use a basis of 80 eigenstates of the undriven square well. For $\kappa = 1$ this basis extends well into the

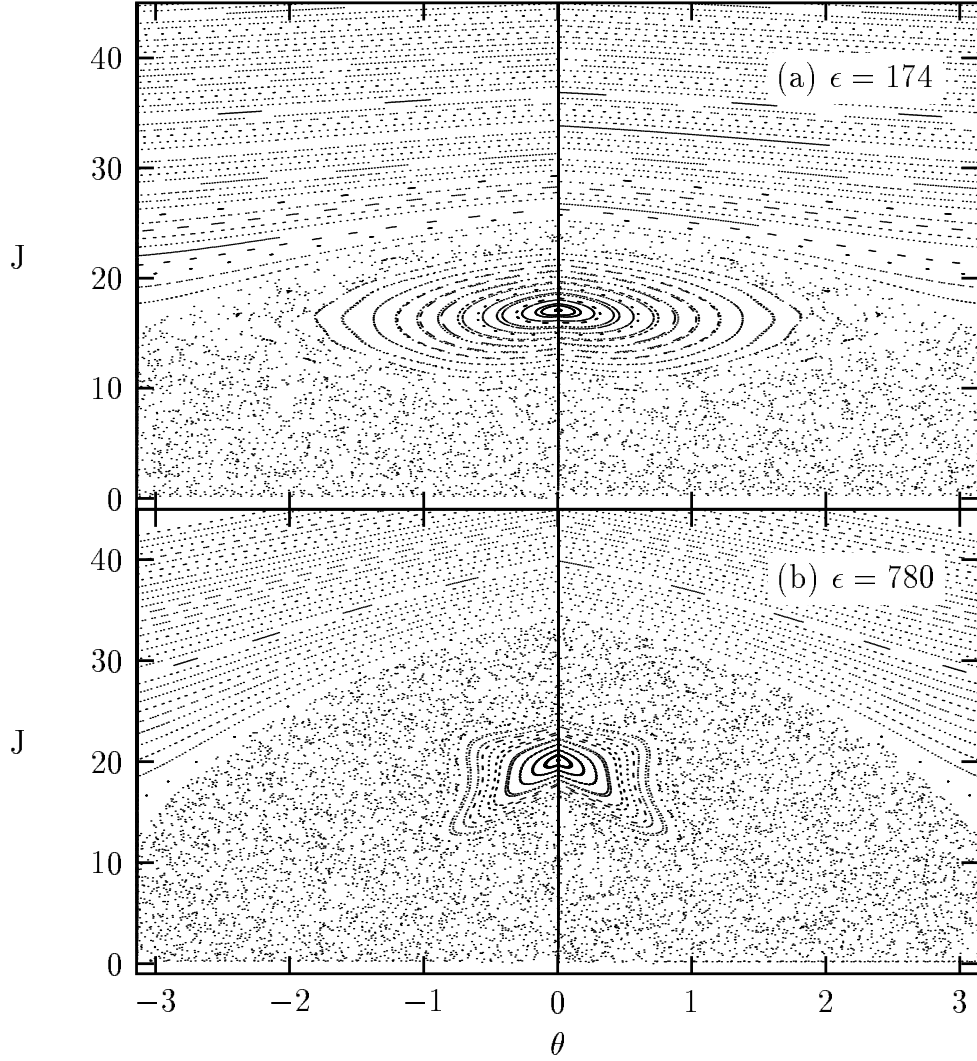


Figure 3.1: Strobe plots of the classical dynamics of the driven square well at two field strengths. J and θ are the dimensionless action-angle variables for the undriven square well. In (a) $\epsilon = 174$ and the $M = 1$ primary resonance is a prominent elliptical feature centered at $\theta = 0$, $J = 16$. All higher-order resonances have been destroyed at this field strength. In (b) $\epsilon = 780$ and the $M = 1$ resonance is distorted and occupies a smaller region of phase space than at $\epsilon = 174$. The chaotic region is much larger at this higher field strength.

regular region of phase space for all values of ϵ considered here. As long as the quantum basis extends into the regular region it should give an accurate description of all dynamics in the chaotic part of the phase space, since there is little coupling between states in the regular region and states in the chaotic region [31].

3.2 Chaos and Avoided Crossings

We wish to study the quantum dynamics that takes place near an avoided crossing (AC) in the spectrum of quasienergies for this system. Our first step then is to locate some avoided crossings. Figure 3.2 shows the $(\text{mod } \omega_0)$ spectrum of the 40 lowest quasienergies as a function of ϵ . As mentioned in Section 2.3, there is a close connection between the onset of ACs and chaos in the classical system. Figure 3.2 shows that avoided crossings begin to appear between $\epsilon = 100$ and $\epsilon = 200$, and by $\epsilon = 800$ the spectrum is dominated by avoided crossings. This compares well with the growth of the chaotic region in the classical phase space between these two values of ϵ (see Fig. 3.1).

There are many strong ties between avoided crossings and chaos, beyond the observed increase of ACs as the classical system becomes chaotic. Successive avoided crossings are responsible for the transition to a random-matrix distribution [4], a property which has long been associated with chaos. In fact, there is a strong correlation between the overlap of these successive ACs and the fraction of the

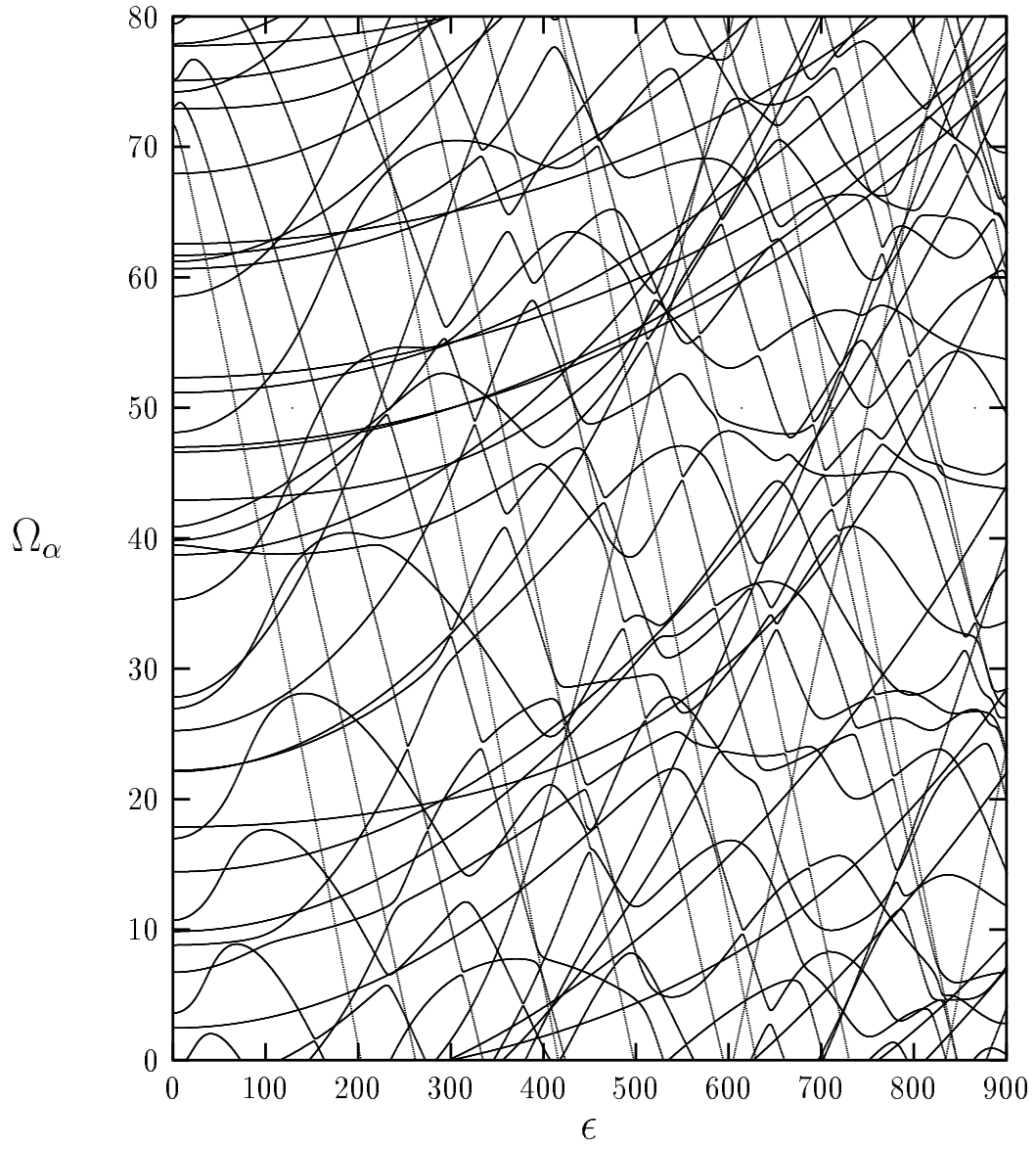


Figure 3.2: Spectrum of quasienergies for the driven square well as a function of field strength. The first avoided crossings appear between $\epsilon = 100$ and $\epsilon = 200$. As ϵ is increased the number of avoided crossings increases rapidly so that by $\epsilon = 800$ avoided crossings dominate the spectrum. Both Ω_α and ϵ are dimensionless quantities.

classical phase space which is chaotic [35]. Other studies have shown that ACs occur between two states only if a quantum wavepacket could tunnel through any Kolmogorov-Arnol'd-Moser (KAM) tori that lie between the two states in the phase space [36]. This means that the states involved in avoided crossings tend to lie in regions of the phase space where the KAM tori have been strongly distorted or destroyed altogether [23].

By studying Fig. 3.2 we can formulate a general picture of what is happening to the quasienergy curves of this system as ϵ is increased. At low ϵ there are no avoided crossings and most of the quasienergy curves maintain a constant slope. The only curvature here is in the set of curves that look like the characteristic curves of the Mathieu equation [32]. The states associated with these curves are becoming trapped in the pendulum-like $M = 1$ primary resonance that forms as ϵ increases from 0. Husimi plots of states with these quasienergies are localized inside this resonance (see Fig. 3.4b below). The curve that looks like the ground state of the Mathieu equation is connected to the $n=16$ square well state at $\epsilon = 0$. Note that $J = 16$ is the exact position of the $M = 1$ resonance in the strobe plots of Fig. 3.1. At higher values of ϵ , ACs begin to appear. At the avoided crossing itself there is a significant change in the slope of the quasienergy curves, but at these moderate values of ϵ the AC seems to result only in an exchange of slopes between the two curves. At the highest values of ϵ shown in Fig. 3.2 the avoided crossings result

in dramatic changes in the slopes of the quasienergy curves, not just an exchange of slope. One may also note that the Mathieu curves are no longer identifiable at these values of ϵ . At these high values of ϵ the $N = 1$ resonance has become highly distorted and is beginning to disappear into the chaotic sea (see Fig. 3.1b). Thus we see that there is a strong connection between changes in the classical phase space and changes in the quasienergy spectrum.

3.3 Changes in Floquet State Structure

This connection between chaos and quasienergy curves is interesting, but it is not entirely clear. For one thing, only the connection between very large changes in the classical phase space and correspondingly large changes in the quasienergy spectrum has been established. We would like to study the changes that take place at a single avoided crossing. Additionally, we would like to see changes in the structure of the Floquet states, rather than changes in the quasienergy curves. We can use the Husimi distributions of Floquet states to visualize these structural changes that take place at an AC. We will examine the Husimi distributions of Floquet states at values of ϵ slightly less than, slightly greater than, and at the value at which that state undergoes an AC. This will allow us to determine what changes occur at the AC and to what extent these changes survive at higher values of ϵ .

A close inspection of Fig. 3.2 reveals that not all avoided crossings look the

same. As discussed in Sec. 3.2 there are crossings where the curves simply exchange slopes and crossings where the slopes change. We will refer to the crossings that exchange slopes as sharp ACs. The states involved in such an AC are weakly coupled and usually lie in different regions of the phase space (inside a resonance and in the chaotic region, for instance). The other type, broad ACs, involve strongly coupled states that usually reside in the same region of phase space. In fact, most broad ACs occur between states that are associated with the region of chaos.

3.3.1 Sharp Crossing

Figure 3.3 is a detail from Fig. 3.2 that focuses on a sharp avoided crossing at $\epsilon \approx 175$. The two curves that participate in the avoided crossing are labeled A and B. In Fig. 3.4 we show the Husimi distributions of the two Floquet states at $\epsilon = 170, 175.5$, and 180 . At $\epsilon = 170$ we can see that state A is contained within the $n=1$ primary resonance (see Fig. 3.1a for a picture of the classical dynamics near this field strength) while state B lies in the low-energy chaotic region. At $\epsilon = 175.5$, the center of the avoided crossing, the Husimi distributions for both states appear to be mixtures of the states shown for $\epsilon = 170$. Clearly the AC has a dramatic impact on the structure of these states at this particular value of ϵ . However, the Husimi distributions at $\epsilon = 180$ show that these changes do not persist at higher field strengths. The two states simply exchange their structure, so that the net effect is a

relabeling of the Floquet states. So away from the AC itself the overall structure of the quantum phase space is unchanged. Others have found similar results in other systems [37].

These dynamics can be understood quite well using a two-level approach [38]. These sharp ACs only involve the two Floquet states whose curves nearly come together. The rest of the Hilbert space has very little influence on the structure of these two states. Without any contribution from other states, these two levels can only exchange their structure. These types of crossings play an important role in tunneling, since a state originally confined to a resonance has become a chaotic state after the AC [39], but they do not play a significant role in altering the structure of the quantum phase space.

3.3.2 Broad Crossing

In a broad AC several states make significant contributions to the dynamics. A particularly striking example of this is shown in Fig. 3.5, where two ACs (at $\epsilon \approx 750$ and $\epsilon \approx 765$) actually overlap. Here there are three states (labeled C, D, and E) that are strongly influencing each others' dynamics. There is no simple exchange of slopes between the curves in this AC. Hence, we might expect to find more interesting (and permanent) structural changes in this crossing than in the previously studied one. Figure 3.6 shows the effect of the avoided crossing on the structure of the three

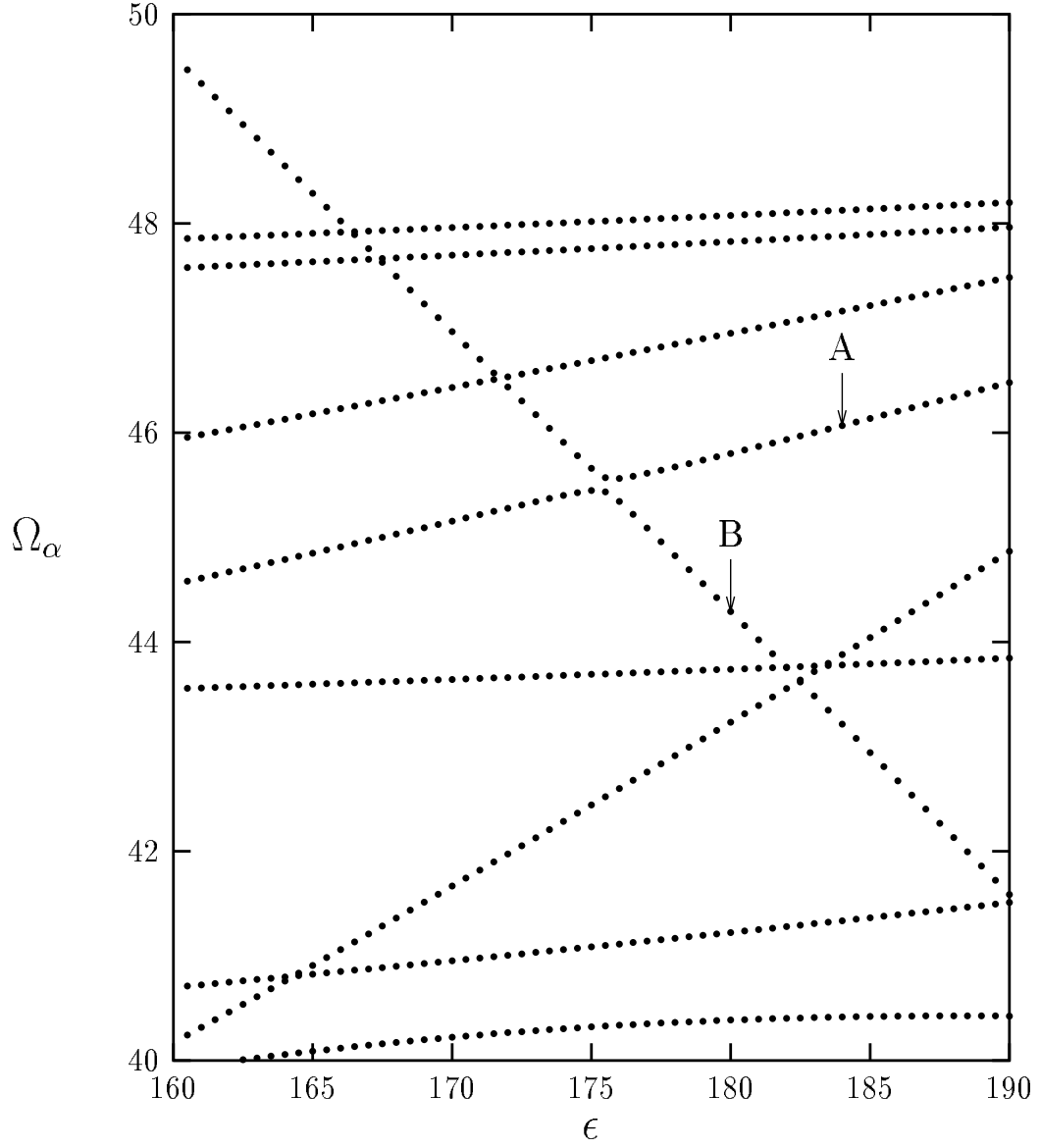


Figure 3.3: Detail from Figure 3.2 showing a sharp avoided crossing near $\epsilon = 175.5$. The quasienergy curves involved in the avoided crossing are labeled A and B.

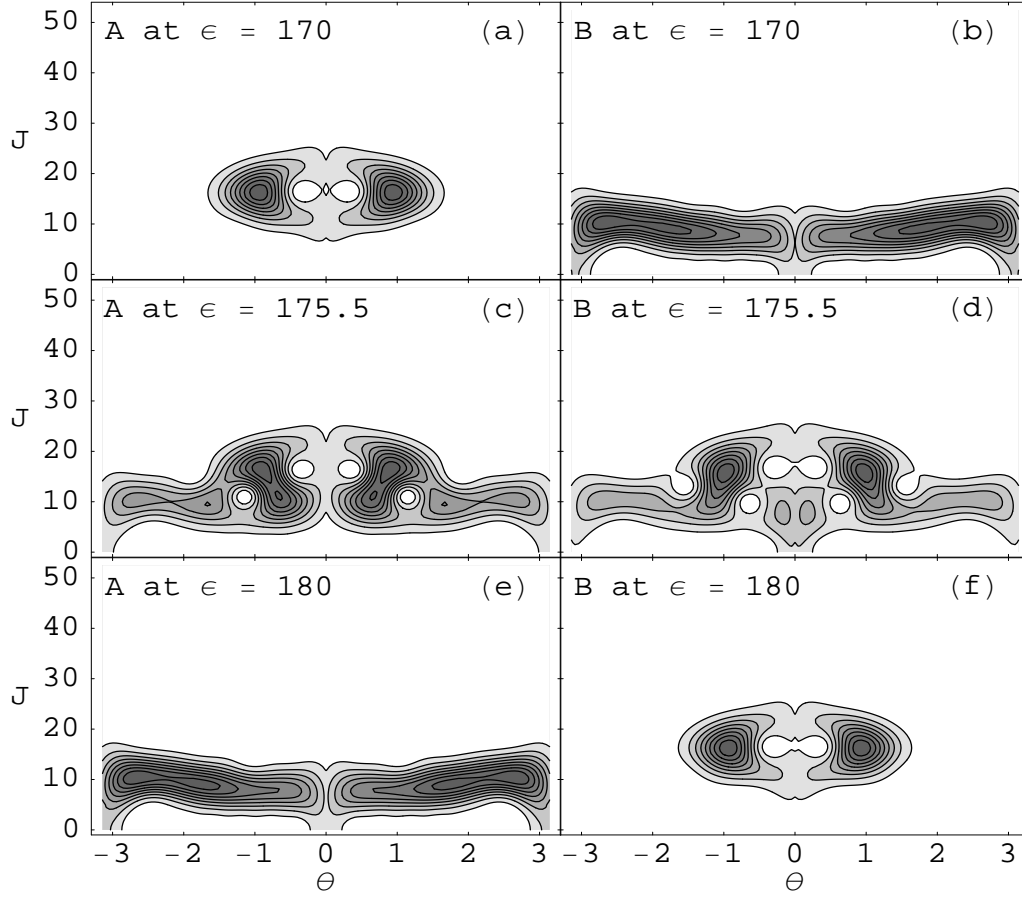


Figure 3.4: Husimi distributions of the Floquet states involved in the avoided crossing shown in Figure 3.3. The labels A and B indicate the quasienergy curve in Fig. 3.3 with which each state is associated. The ϵ values indicate the field strength at which the Floquet state was calculated. At $\epsilon = 175.5$ (the center of the avoided crossing) both Floquet states are mixtures of the two states at $\epsilon = 170$. By $\epsilon = 180$ A and B have exchanged their structure completely. Note that the coordinates for all of the Husimi plots are the dimensionless action-angle variables used in Fig. 3.1.

states that are involved. As in the sharp crossing there is a mixing of structures for values of ϵ that lie within the crossing region. However, in this case the changes do not disappear when we look at larger values of field strength. With this type of AC the states are not simply “reabeled”, but undergo actual changes in their phase space structure. Particularly striking is the difference between Figs. 3.6c and 3.6h. These states would be identical if there was a complete exchange of structure as seen in the sharp AC. Instead, before the crossing state E is localized at very low energies, but after the crossing state D (which is the state most closely associated with the low- ϵ state E) has spread into the higher energy portion of the region of chaos. The avoided crossing has delocalized this particular Floquet state. We find this result to be quite general, that broad ACs lead to permanent changes in the structure of Floquet states that tend to delocalize the states. Of course, since the region of chaos is bounded the states can only delocalize until they reach the boundaries of the chaos. At extremely high values of ϵ , where nearly every “chaotic” state has undergone many broad avoided crossings, we find that all of these states are delocalized and fill the chaotic region [40].

3.4 Effect on Radiation Spectra

Now that we have seen how avoided crossings can affect the structure of Floquet states we would like to see how they effect an experimentally observable quantity,

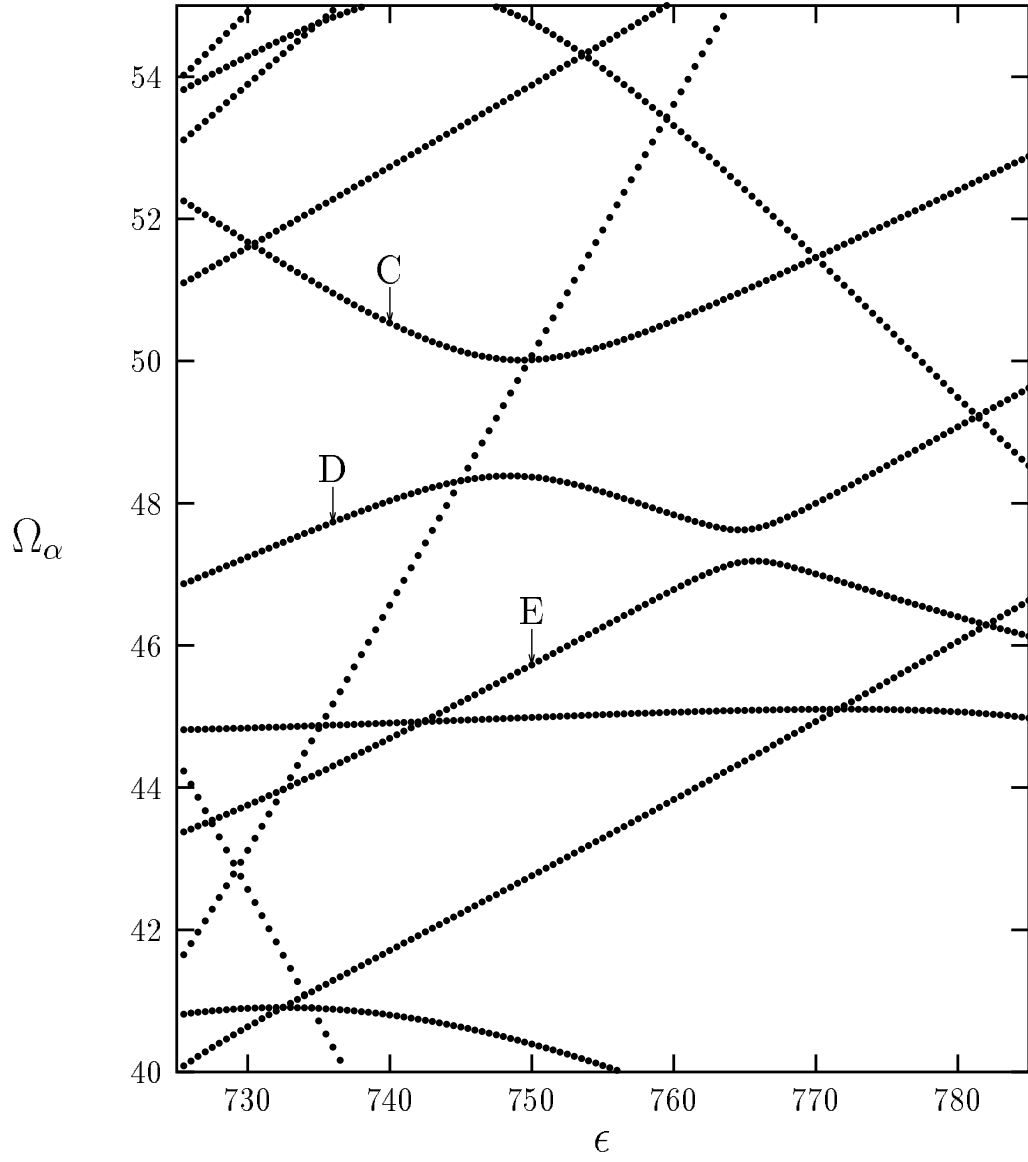


Figure 3.5: Detail of Figure 2.8 showing a pair of broad avoided crossings near $\epsilon = 760$. The three quasienergy curves that are involved in the avoided crossing are labeled C, D, and E.

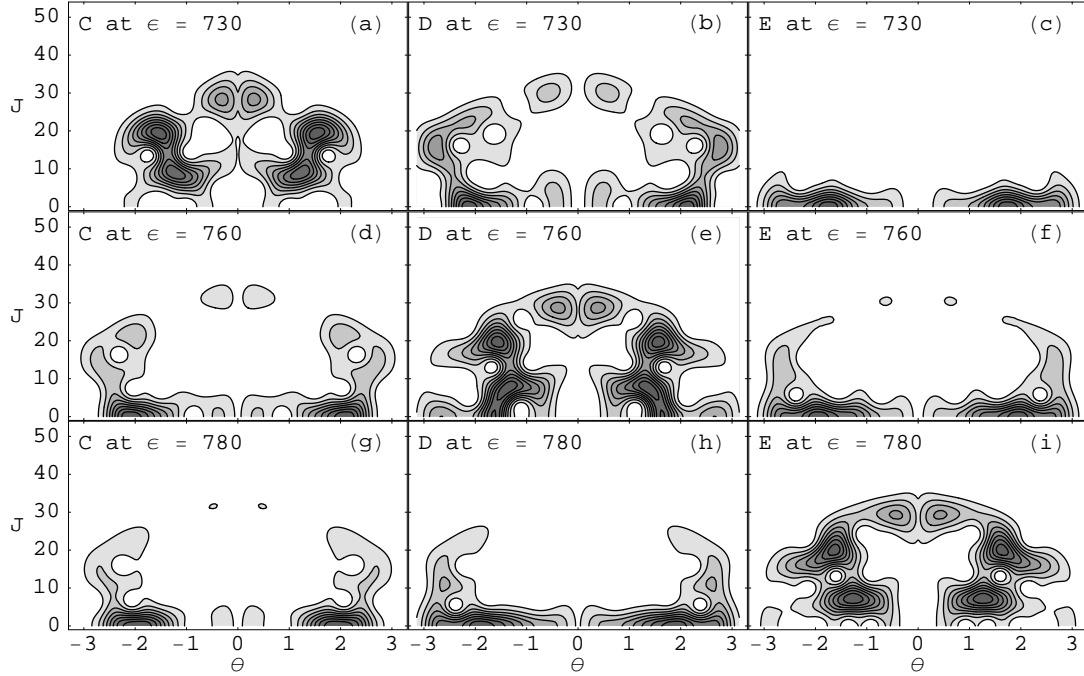


Figure 3.6: Husimi distributions of the three Floquet states involved in the crossings shown in Figure 3.5. The labels C, D, and E indicate the quasienergy curve in Fig. 3.5 with which each state is associated. At $\epsilon = 760$ all three states are mixtures of the states at $\epsilon = 740$. By $\epsilon = 780$ the states have exchanged most of their structure, but there are significant differences from the $\epsilon = 740$ states. In particular, we expect the states (c) and (h) to have similar structure but instead find that (h) is much less localized than (c).

namely the radiation spectrum. In Chapter 2 we found that the generation of high harmonics increased as the system, initially in a single Floquet state, passed through an avoided crossing [40]. However, this effect was caused by population transfer from the original Floquet state to another state as the field strength was increased. This population transfer creates a superposition of two Floquet states that displays increased radiation at high frequencies (albeit shifted away from the harmonic frequencies). In this study we would like to focus on changes in the radiation spectrum that are caused by the changing structure of a single Floquet state. For this reason we will calculate radiation spectra by starting the system in a single Floquet state and maintaining a constant field strength for 128 cycles of the driving field. The expectation value of the acceleration for the state is calculated during this time interval. We then calculate the Fourier transform, $\chi(\omega)$, of this acceleration time series. The square modulus of the Fourier transform gives us the radiation spectrum. Because the Floquet states are periodic with period $2\pi/\omega_0$ it is not truly necessary to calculate for 128 cycles of the driving field. However, this long integration time exposes numerical errors that might be hidden in a shorter calculation.

To study the effect of structural changes on radiation spectra we cannot simply study the spectrum of a single Floquet state for various values of ϵ . Avoided crossings cause states to exchange structure, effectively relabeling the states. If true structural

changes are to be distinguished from simple relabeling, one must account for this relabeling when comparing different spectra. At the midpoint of the avoided crossing this is nearly impossible to do, since the relabeling has not fully taken effect. For values of ϵ that are beyond the AC, the relabeling can easily be taken into account. Our procedure in the following is to calculate spectra for a state before the AC, the same state (on the same curve) at the midpoint of the AC, and the relabeled state (now on a different quasienergy curve) after the AC. This separates the changes in the radiation spectrum that occur because of structural change in the Floquet state from the apparent changes that occur because the states have been relabeled.

3.4.1 Sharp Crossing

We first calculate radiation spectra for the states whose Husimi distributions are shown in Fig. 3.4(a,c, and f). The first two states are associated with the curve A in Fig. 3.3, while the third is associated with curve B. By changing from A to B after the avoided crossing we can account for the effects of relabeling as described above. The spectra are shown in Fig. 3.7. Between $\epsilon = 170$ and $\epsilon = 175.5$ there is a significant increase in the radiation at the highest harmonics (11-19). However, these harmonics have decreased at $\epsilon = 180$. This increase and subsequent reduction is easier to see in Fig. 3.8, which shows the differences between the spectrum at $\epsilon = 170$ and the spectra at $\epsilon = 175.5$ and 180. This temporary increase in high

harmonic generation is exactly what we expect from the temporary changes in the phase space structure seen in Fig. 3.4. At the midpoint of the AC both states are a mixture of the two states at $\epsilon = 170$ and both are spread over a wider region of phase space. This leads to an increase in harmonic generation at this value of ϵ . After the avoided crossing, however, these structural changes disappear (with the exception of the relabeling) and the harmonic generation subsides. Thus, sharp ACs only affect the radiation spectrum of a Floquet state for field strengths that lie within the crossing.

3.4.2 Broad Crossing

Now we investigate the radiation spectra for the states shown in Fig. 3.6(c, f, and h). Again we switch from state E to state D for values of ϵ that are beyond the avoided crossing, to account for the relabeling that takes place. Fig. 3.9 shows the spectra for these states. There is a steady increase in the radiation at the highest harmonics (31-45) as ϵ is increased. This is more easily seen in Fig. 3.10 which shows the differences between the spectra. The changes in the spectra are quite complicated, but there is clearly no reversal in the increase of high harmonics as was observed in the sharp crossing. This broad AC permanently increases the high harmonic generation. This is closely tied to the delocalization that is observed in Fig. 3.6, since the generation of high harmonics depends on the number of energy

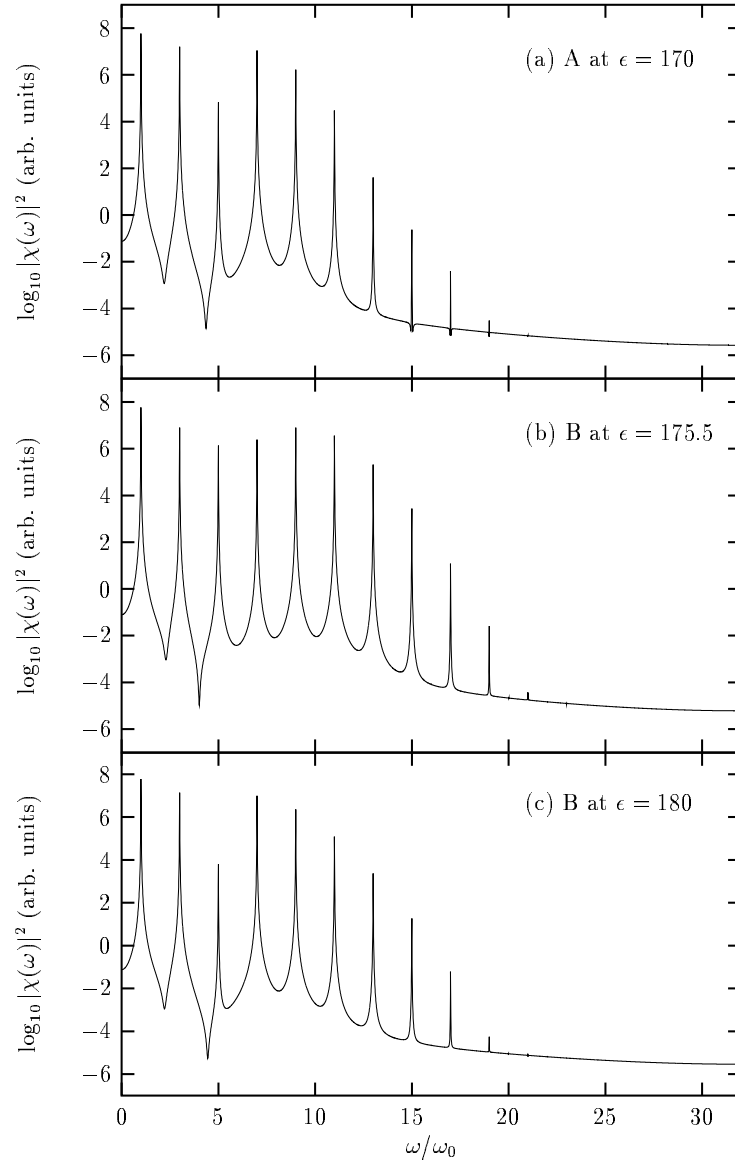


Figure 3.7: Radiation spectra generated by the Floquet states shown in Figure 3.4(a,c,e). There is a significant increase in harmonic generation from (a) $\epsilon = 170$ to (b) $\epsilon = 175.5$. However, by (c) $\epsilon = 180$ this increase has disappeared. All spectra have been normalized so that they have the same power at the fundamental frequency ω_0 .

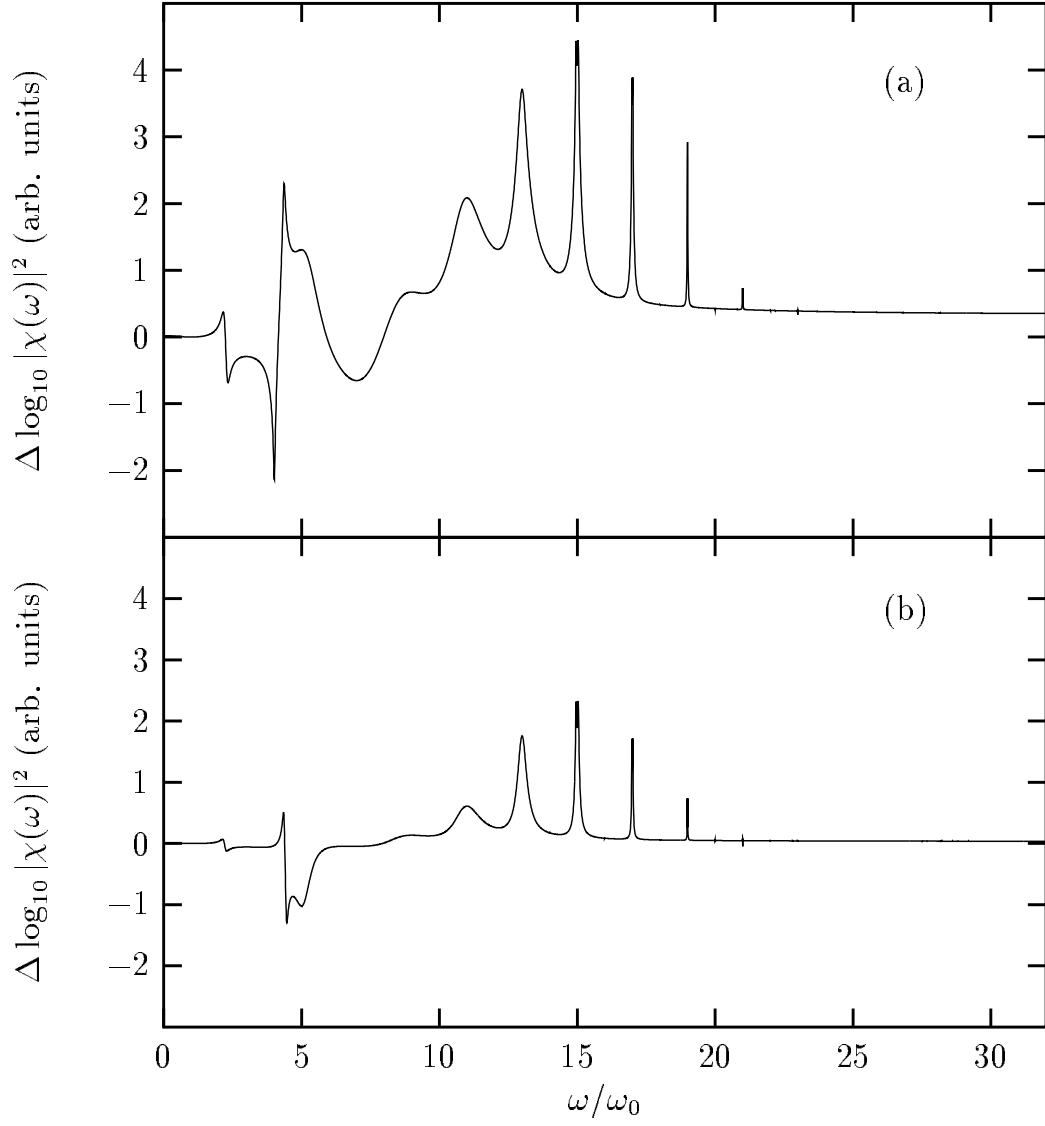


Figure 3.8: Differences between spectra shown in Figure 3.7. The difference between Fig. 3.7b and Fig. 3.7a is shown in (a). The difference between 3.7c and 3.7a is shown in (b). The increase and subsequent decrease in harmonic generation is apparent.

levels over which the Floquet state is spread [40].

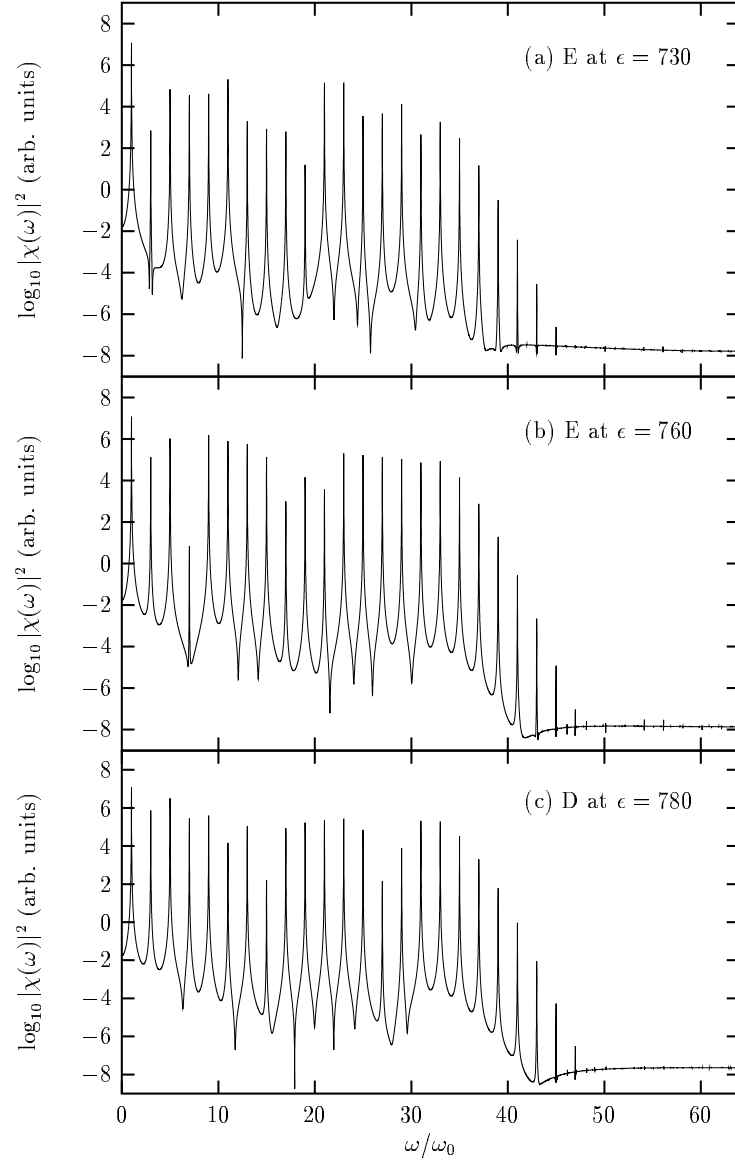


Figure 3.9: Radiation spectra generated by the Floquet states shown in Figure 3.6(c,f,h). There is a significant increase in harmonic generation from (a) $\epsilon = 740$ to (b) $\epsilon = 760$ and by (c) $\epsilon = 780$ the harmonic generation has increased even further. All spectra have been normalized so that they have the same power at the fundamental frequency ω .

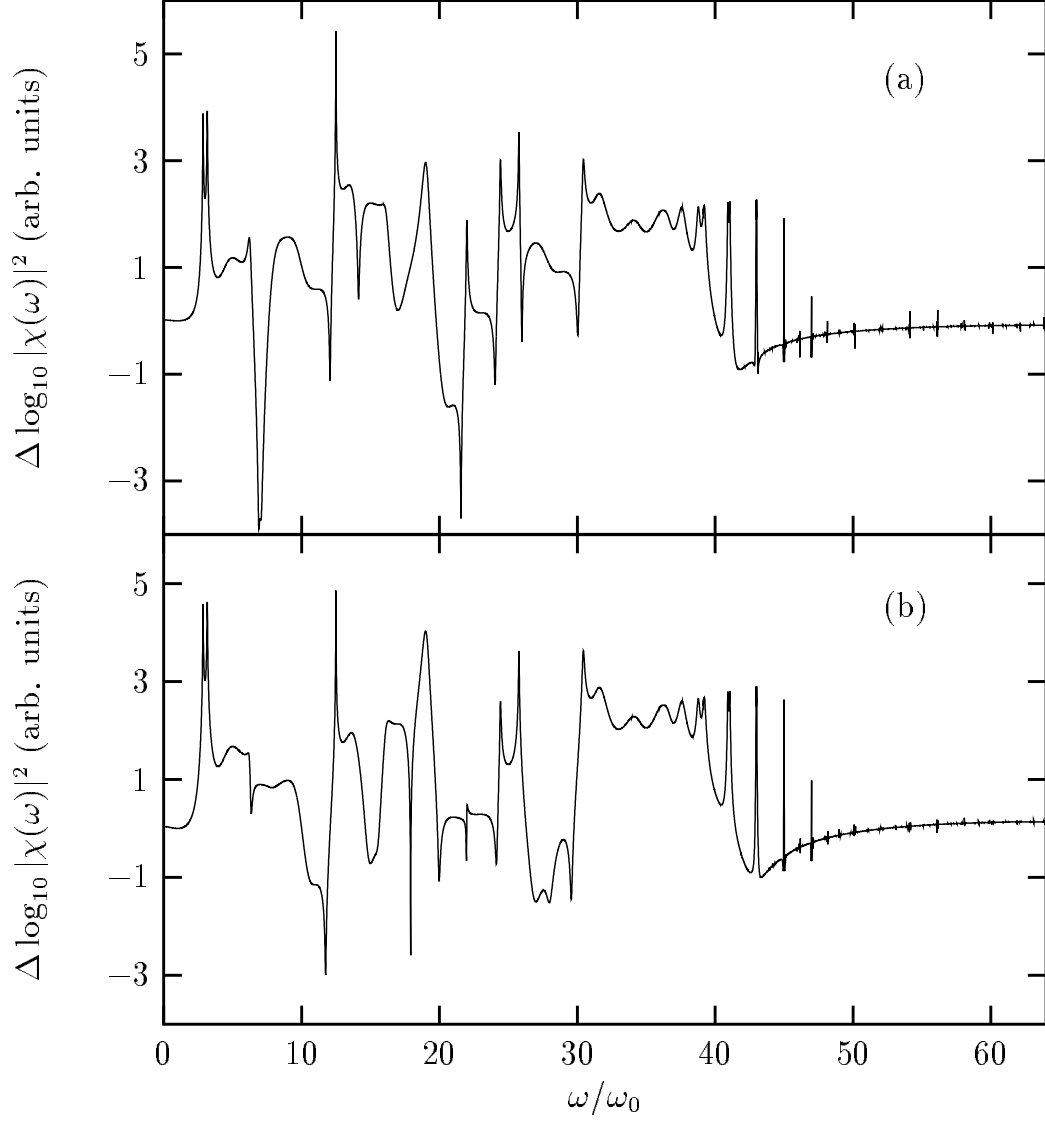


Figure 3.10: Differences between spectra shown in Figure 3.9. The difference between Fig. 3.9b and Fig. 3.9a is shown in (a). The difference between 3.9c and 3.9a is shown in (b). The increase in harmonic generation seen in (a) clearly persists in (b).

Chapter 4

The Transition to Chaos

In the previous chapter we saw that Floquet eigenstates change as ϵ is increased in the driven square well system. In particular, we saw that these states tend to delocalize as they pass through overlapping avoided crossings. In this chapter we will use the same model, but examine how the overall quantum system changes as ϵ is increased. We show that overlapping avoided crossings play a key role in increasing information entropy in the system and destroying localization. However, localized states still exist at relatively high values of ϵ . We propose a possible classical explanation for this phenomenon and show that it is consistent with the complete lack of localization that is seen at extremely high values of ϵ .

The results presented in the first part of this chapter, and those presented in earlier chapters indicate that overlapping avoided crossings play an important

role in the transition of this system from a regular quantum system to a chaotic one. We discuss how these results fit with what has been said about quantum chaos in the literature. At the end of the chapter we present a unified description of the dynamics of harmonically-driven, bound, one-dimensional quantum systems. This description accounts for many of the observed phenomena in these systems and highlights the close connection between the quantum systems and their chaotic classical counterparts.

4.1 Entropy and Delocalization

The results shown in the previous chapter show that sharp, isolated avoided crossings result in an exchange of structure between the two states involved while broad, overlapping avoided crossings can result in genuine changes to the states involved. These overlapping avoided crossings seem to cause the states to become delocalized, as can be seen qualitatively in the Husimi distributions shown in Fig. 3.6. To get a quantitative measure of how overlapping avoided crossings lead to delocalization we must have a quantitative measure of localization. One of the most commonly used quantitative measures of the localization of a quantum state is its information entropy, or Shannon entropy [41, 42] which is defined as

$$S_\alpha = - \sum_n |c_{n\alpha}|^2 \ln(|c_{n\alpha}|^2) \quad (4.1)$$

where the $c_{n\alpha}$ are the coefficients in the basis expansion of the wavefunction. In this chapter we will continue to study the driven square well system and we will use the eigenstates of the undriven square well as the basis with which we calculate the Floquet states of the driven system. The Floquet-state wavefunction can then be written as

$$|\psi_\alpha\rangle = \sum_n c_{n\alpha} |n\rangle \quad (4.2)$$

where α is an index used to label the Floquet states and $|n\rangle$ is an eigenstate of the undriven square well.

Low values of S_α indicate a state that is relatively localized in the basis of unperturbed energy eigenstates while high values indicate a state that is delocalized. In this system, though, the Shannon entropy is not enough by itself to identify the localized states we are interested in. This is because the classical dynamics of this system is always regular at high values of action. A full description of the classical dynamics of this system can be found in Chapter 2, but here we present a few strobe plots of the classical dynamics in Fig. 4.1. At very low field strengths ($\epsilon = 100$), only trajectories at very low J are chaotic while the $M = 1$ primary resonance dominates the dynamics around $J = 16$ and trajectories above $J \approx 20$ are regular. At $\epsilon = 960$ the chaotic region has grown considerably and the $M = 1$ resonance is less prominent, but the motion above $J \approx 35$ is still regular. For extremely high field strengths ($\epsilon = 6400$) the $M = 1$ resonance has been completely destroyed but

there is still regular motion at high values of J . Based on these observations we expect the quantum system to have delocalized eigenstates at low energies (at least for high values of ϵ), but localized regular eigenstates at high energies. For this reason a low value of the Shannon entropy for a Floquet state may indicate that the state is a high-energy regular state rather than a localized state in the chaotic region.

We need an additional quantity to help us identify states that are localized in the chaotic region, and that quantity is the expectation value of H_0 , the Hamiltonian for the undriven square well. This quantity is defined as

$$H_\alpha = \langle \psi_\alpha | H_0 | \psi_\alpha \rangle = \sum_n |c_{n\alpha}|^2 E_n \quad (4.3)$$

and the E_n are given in Eq. 2.8. Plots of energy versus entropy have often been used to identify localized states in quantum systems whose classical counterpart is chaotic [42, 43]. States that have low values of H_α will be located in the low energy chaotic region. Any of these states that also have low values of S_α will be localized. Plots of H_α versus S_α for our system are shown in Fig. 4.2.

In Fig. 4.2a ($\epsilon = 100$) we see that the states with high values of H_α form a regular sequence that decreases in entropy as the energy increases. These are the high energy regular states discussed above. Near $H_\alpha = 600$ there is a line of points that all have about the same energy but a spread of entropies. Each of the states in this line is associated with the $M = 1$ resonance seen in Fig. 4.1a. The state in

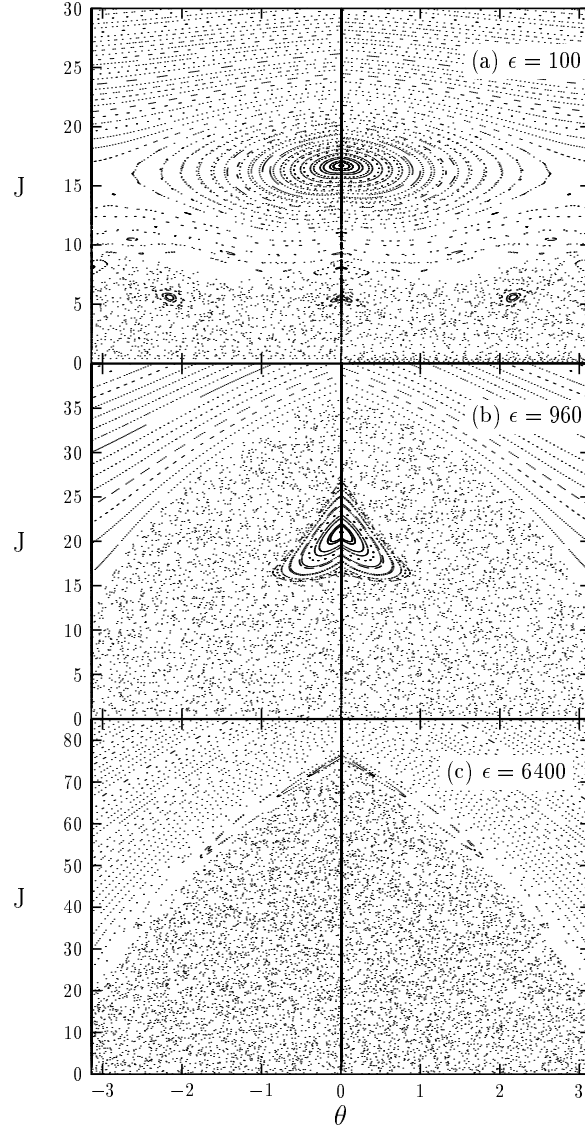


Figure 4.1: Strobe plots of the classical dynamics of the driven square well at three field strengths. J and θ are the dimensionless action-angle variables for the undriven square well. At (a) $\epsilon = 100$ and (b) $\epsilon = 960$ the $M = 1$ primary resonance is still visible near $J = 16$ and $J = 20$, respectively. At (c) $\epsilon = 6400$ the resonance has been completely destroyed, but a higher order resonance is beginning to form at the top of the chaotic region.

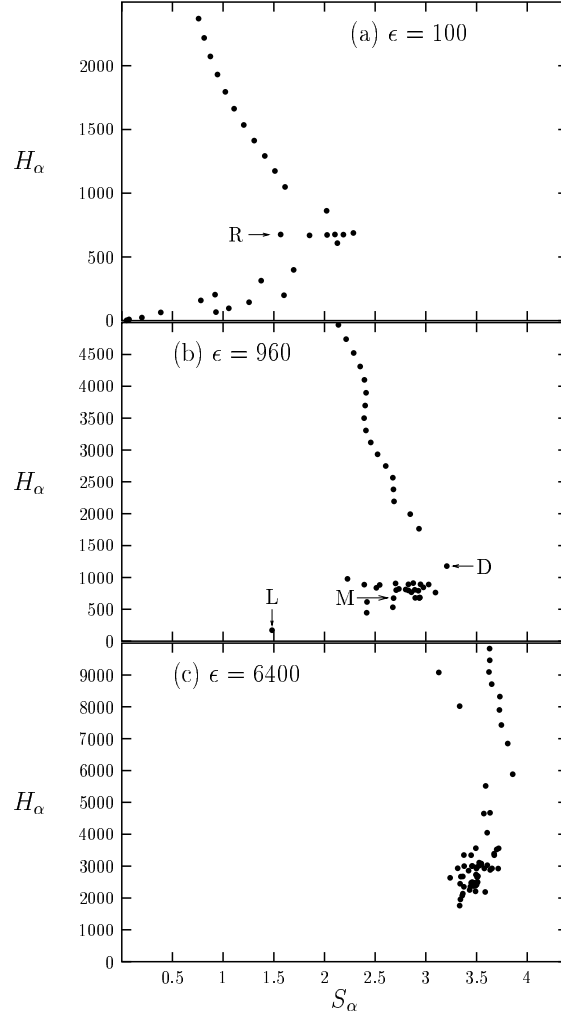


Figure 4.2: Plots of H_α vs. S_α (see Eqs. 4.3 and 4.1) at three different field strengths. At (a) $\epsilon = 100$ the sequence of regular states is clearly visible at high H_α , while at low H_α the states in the chaotic region do not form an organized sequence. The states associated with the $M = 1$ primary resonance form a line at $H_\alpha \approx 600$ indicated by the label R in the plot. At (b) $\epsilon = 960$ most of the low H_α states are in a cluster between $S_\alpha = 2$ and $S_\alpha = 3$. One strongly localized state is indicated by the label L in the plot. The labels M and D indicate moderately delocalized and strongly delocalized states, respectively. At (c) $\epsilon = 6400$ all low H_α states are clustered around $S_\alpha = 3.5$ and there are no clearly visible localized states.

this line that has the lowest entropy is the "ground state" of that resonance, and each point to the right of that represents an excited state of the resonance. Below $H_\alpha = 600$ the states form a somewhat irregular sequence as one might expect from the fact that the classical dynamics is a mix of regular and chaotic motion for low energies at this field strength. Fig. 4.2b is quite different. Here the high energy states still form a regular, if slightly distorted, sequence. However, the resonance feature is no longer clearly visible and the low energy states are mostly bunched together near $H_\alpha = 750$ and $S_\alpha = 2.75$. This grouping occurs as the states become delocalized and spread throughout the chaotic region. This tends to move all of the states toward some average value of H_α (because they are all spread evenly over the entire energy range of the chaotic region) and toward higher values of S_α (because all of the states are delocalized). At this field strength, though, not all the states in the chaotic region are fully delocalized. The label L in the plot indicates a state that is still highly localized, the label M indicates a state that is only moderately delocalized, and the label D indicates a state that is fully delocalized (very high entropy). Husimi distributions for these three states are shown in Fig. 4.3 and they support our characterization of these states. Finally, in Fig. 4.2c ($\epsilon = 6400$) we see that localization has been completely destroyed. All of the low energy states are in a cluster near $H_\alpha = 2500$ and $S_\alpha = 3.5$. The high energy states still form a regular sequence, although there are irregularities at the low energy end of that sequence.

At this high field strength we would expect to find no localized states in the chaotic region.

It is clear from Fig. 4.2 that there is a trend toward higher entropy as ϵ is increased. To illustrate that trend we show, in Fig. 4.4, a plot of the average entropy in the system versus field strength. The average entropy is calculated by first ordering the states by increasing value of H_α and then using the entropies of the 60 states with the lowest values of H_α to calculate the average entropy, \bar{S} . At $\epsilon = 0$ all states have an entropy of 0, because the Floquet states at $\epsilon = 0$ are the eigenstates of the undriven square well. As ϵ is increased, \bar{S} increases rapidly as the chaotic region forms and grows in the classical dynamics and the quantum Floquet states begin to delocalize. At high values of ϵ the curve begins to flatten, because at high ϵ most of the states are already fully delocalized. Most of the increase in entropy that occurs for ϵ greater than about 3200 is due to the increase in the size of the chaotic region. This brings more basis states into the strongly coupled chaotic group, thus allowing each chaotic eigenstate to be spread over a greater number of basis states and thereby increase its entropy.

4.2 Avoided Crossings and Entropy

In Chapter 3 we saw how overlapping avoided crossings lead to delocalization of quantum Floquet states. Others have found that eliminating avoided crossings in

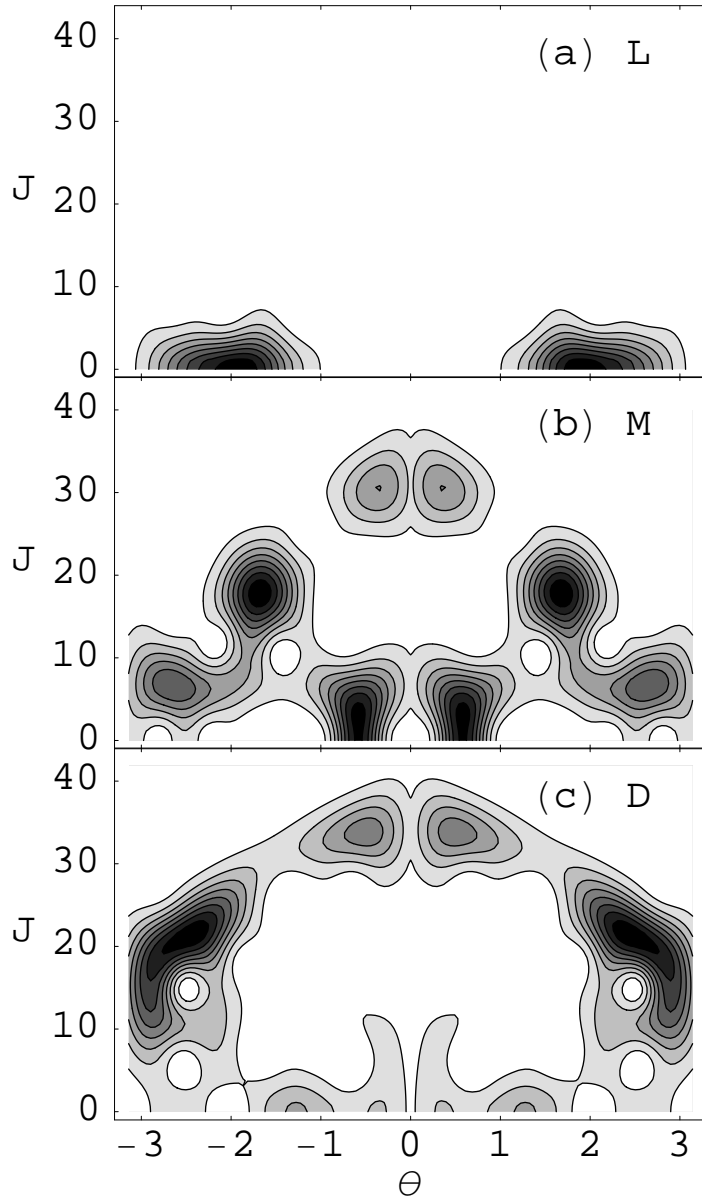


Figure 4.3: Husimi distributions of the states labeled in Fig. 4.2(b). The state (a) L is strongly localized near $J = 1$. The state (b) M is much less localized than L , but still has most of its probability at low J . The state (c) D is fully delocalized in J .

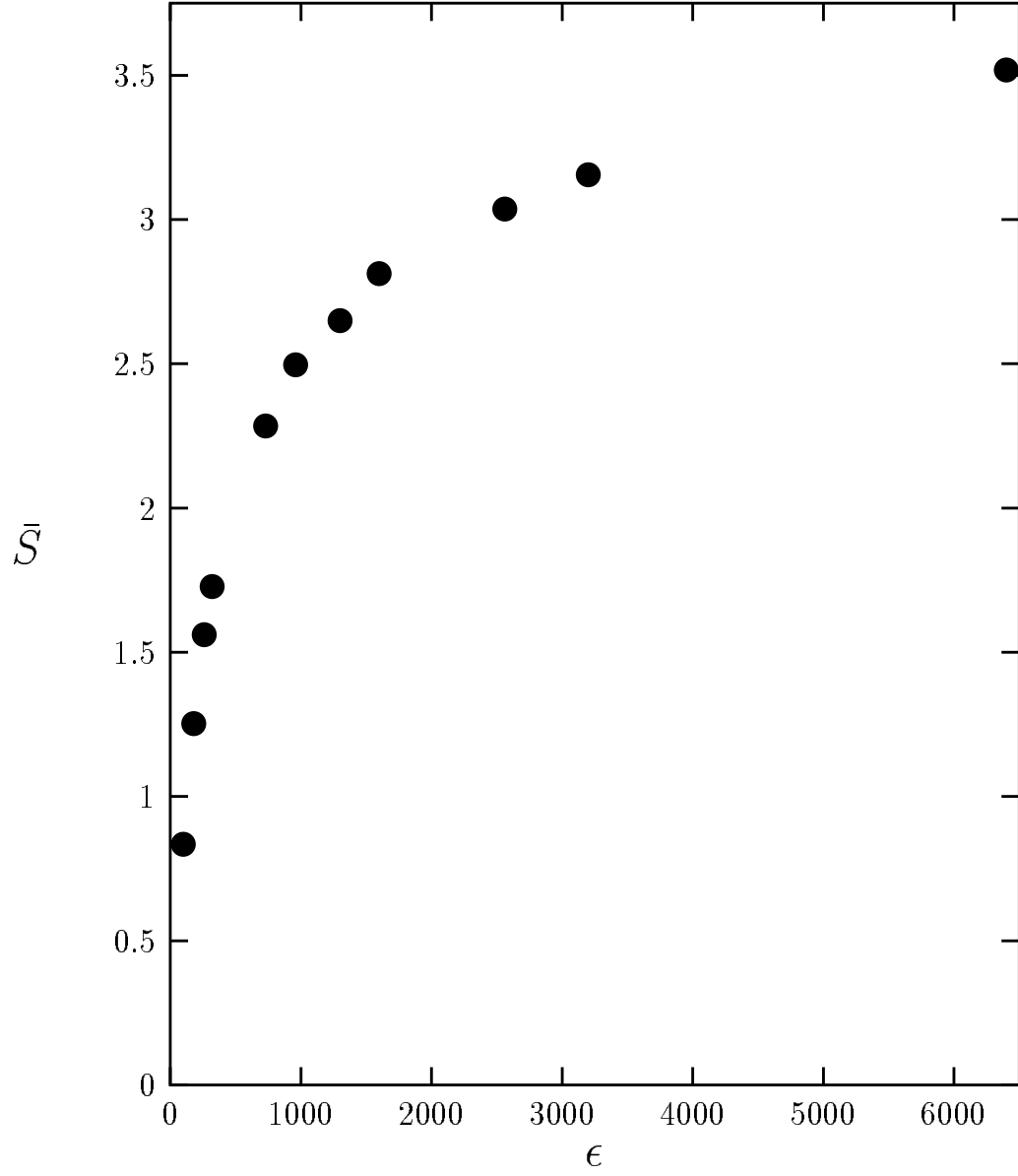


Figure 4.4: Average entropies (\bar{S}) as a function of field strength ϵ . At each field strength the average entropy is calculated using only the 60 states with the lowest values of H_α (see Eq. 4.3). At $\epsilon = 0$ the entropy is 0 for all states. As ϵ is increased \bar{S} rises rapidly at first but more slowly at high ϵ .

a quantum system preserves localization of the eigenstates [44]. It has been proposed [10, 45] that overlapping avoided crossings lead the eigenstates of a classically chaotic quantum system to take on a statistical character. The idea is that in the semiclassical limit, an avoided crossing in the quantum system corresponds directly to a resonance in the classical system. Just as overlapping resonances lead to classical chaos [25], overlapping avoided crossings lead to quantum chaos and stochastic eigenvectors. Delocalization and stochasticity are essentially the same thing (a stochastic eigenvector is spread randomly over some subset of the basis and will thus represent a delocalized state). Both delocalization and stochasticity can be measured by the Shannon entropy. Based on our findings and the proposal of [10, 45], we expect to see a significant increase in entropy for states involved in overlapping avoided crossings.

First we will examine what happens in an isolated, sharp avoided crossing. Fig. 4.5 shows an isolated avoided crossing in the quasienergy spectrum of our system centered near $\epsilon = 175.5$. The labels A and B refer to the continuously connected states associated with the two indicated quasienergy curves. Based on our findings in Chapter 3 we expect these two states to simply exchange their entropies and energies. Fig. 4.6 shows that this is exactly what happens. At $\epsilon = 174$, before the avoided crossing, state A sits at $(S_\alpha = 1.6, H_\alpha = 220)$ and state B is located at $(2.2, 680)$. At $\epsilon = 175.5$, near the center of the avoided crossing, both states are

located around $(2.5, 450)$. At this field strength each state is an approximately equal superposition of the two initial states from $\epsilon = 174$. This leads each state to have an energy that is close to the average of the initial energies and a significantly higher entropy, because the superposition is spread over a larger number of basis states. However, at $\epsilon = 177$, after the avoided crossing, the two states have exchanged their places in the plot as predicted. This example shows that isolated, sharp avoided crossings lead to only a temporary increase in entropy at the center of the avoided crossing. This entropy increase does not remain at values of ϵ that are beyond the avoided crossing. For this reason, isolated avoided crossings do not contribute to the overall delocalization and increasing stochasticity of the eigenstates.

Next we examine what happens when a broad avoided crossing overlaps with another avoided crossing. Fig. 4.7 shows a sequence of overlapping avoided crossings between the states labeled C , D , and E in the range $\epsilon = 250$ to $\epsilon = 330$. The broad avoided crossing between states C and D overlaps with the sharper avoided crossings between D and E at $\epsilon \approx 298$ and between D and C at $\epsilon \approx 305$. Based on our findings in Chapter 3 we expect these overlapping avoided crossings to result in a permanent increase in entropy that remains at field strengths that are beyond the avoided crossing region. Fig. 4.8 shows the (S_α, H_α) values for these states at four different field strengths. As ϵ is increased the motion of the states in the $S_\alpha - H_\alpha$ plane is quite complicated. The basic result is that the overall entropy

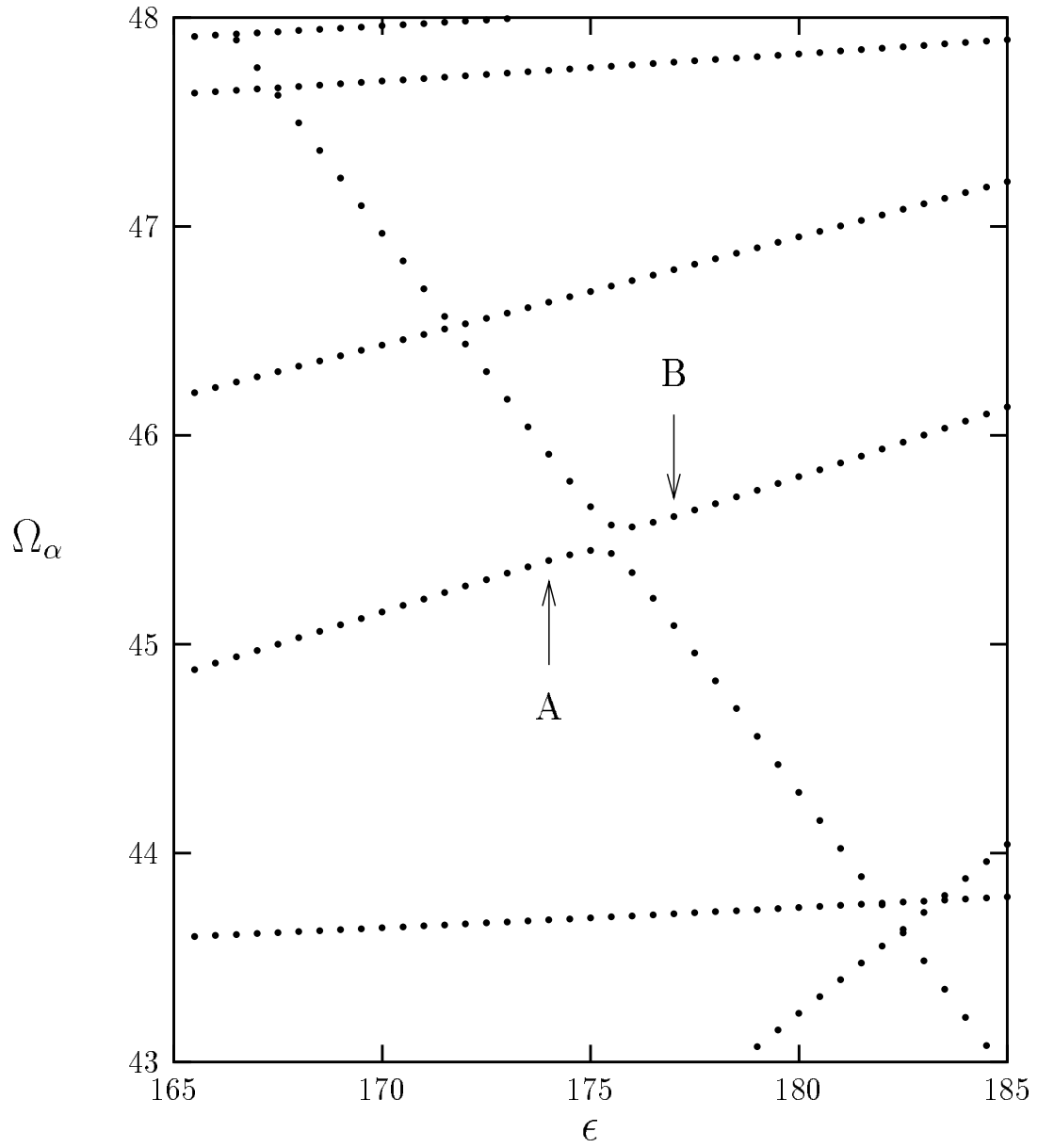


Figure 4.5: Plot of quasienergies Ω_α as a function of field strength showing a sharp avoided crossing near $\epsilon = 175.5$. The labels *A* and *B* indicate the two continuously connected states involved in the avoided crossing.

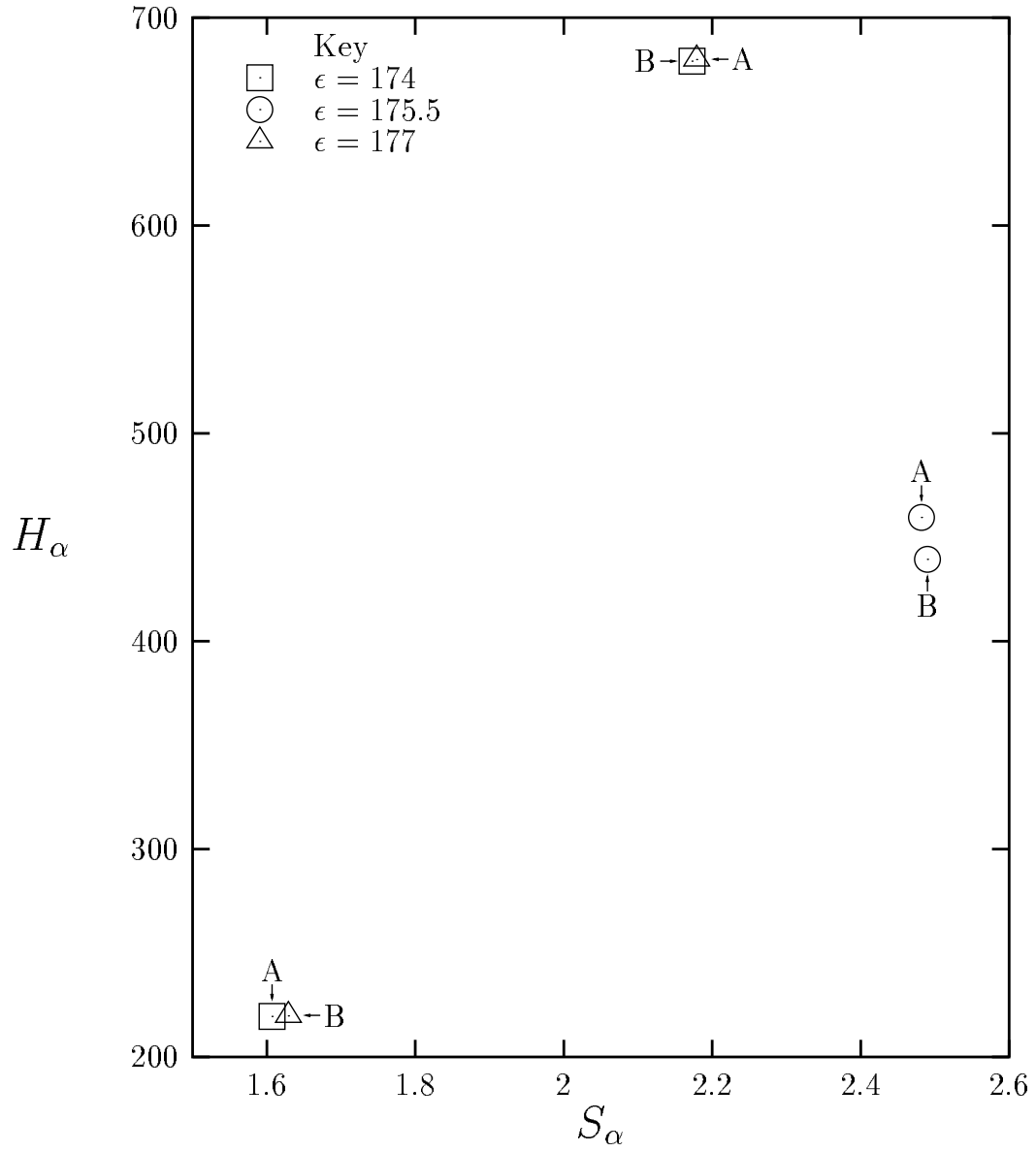


Figure 4.6: Plot of H_α vs. S_α for the states labeled A and B in Fig. 4.5 at three field strengths. The different markers indicate different field strengths. At $\epsilon = 175.5$, at the center of the avoided crossing, the two states both have high entropies and energies that are close to the average of their energies at $\epsilon = 174$. By $\epsilon = 177$ the two states have exchanged places in the plot.

of the three states is increased by the overlapping avoided crossings. State C at $\epsilon = 320$ occupies the same spot that state E occupied at $\epsilon = 260$, so state C has just taken the place of state E . However, states D and E at $\epsilon = 320$ do not occupy the same locations on the graph as did states C and D at $\epsilon = 260$. State E is at a higher entropy at $\epsilon = 320$ than is state C at $\epsilon = 260$, and its energy is near the average of the energies of the initial C and E states. State D has also been shifted to higher entropy and a slightly higher energy after passing through the overlapping avoided crossings. In this case the increase in entropy does not disappear at field strengths beyond the avoided crossing, but remains for all higher field strengths. So we see here that overlapping avoided crossings tend to increase the entropy of the states involved and move their energies toward some average value. It is easy to see how several such overlapping avoided crossings could lead to the clumping of states at high entropy and moderate energy that is seen in Figs. 4.2b and 4.2c. At sufficiently high field strengths every eigenstate in the chaotic region will have passed through many overlapping avoided crossings. The result is that at these field strengths all states in the chaotic region will be delocalized and stochastic in nature.

Clearly there is a relationship between classical chaos on one hand, and delocalization and stochasticity of eigenvectors on the other. But from Figs. 4.2b and 4.3a we see that localized states can exist even in regions of the phase space that are fully chaotic. In the following section we will explore how the classical dynamics of

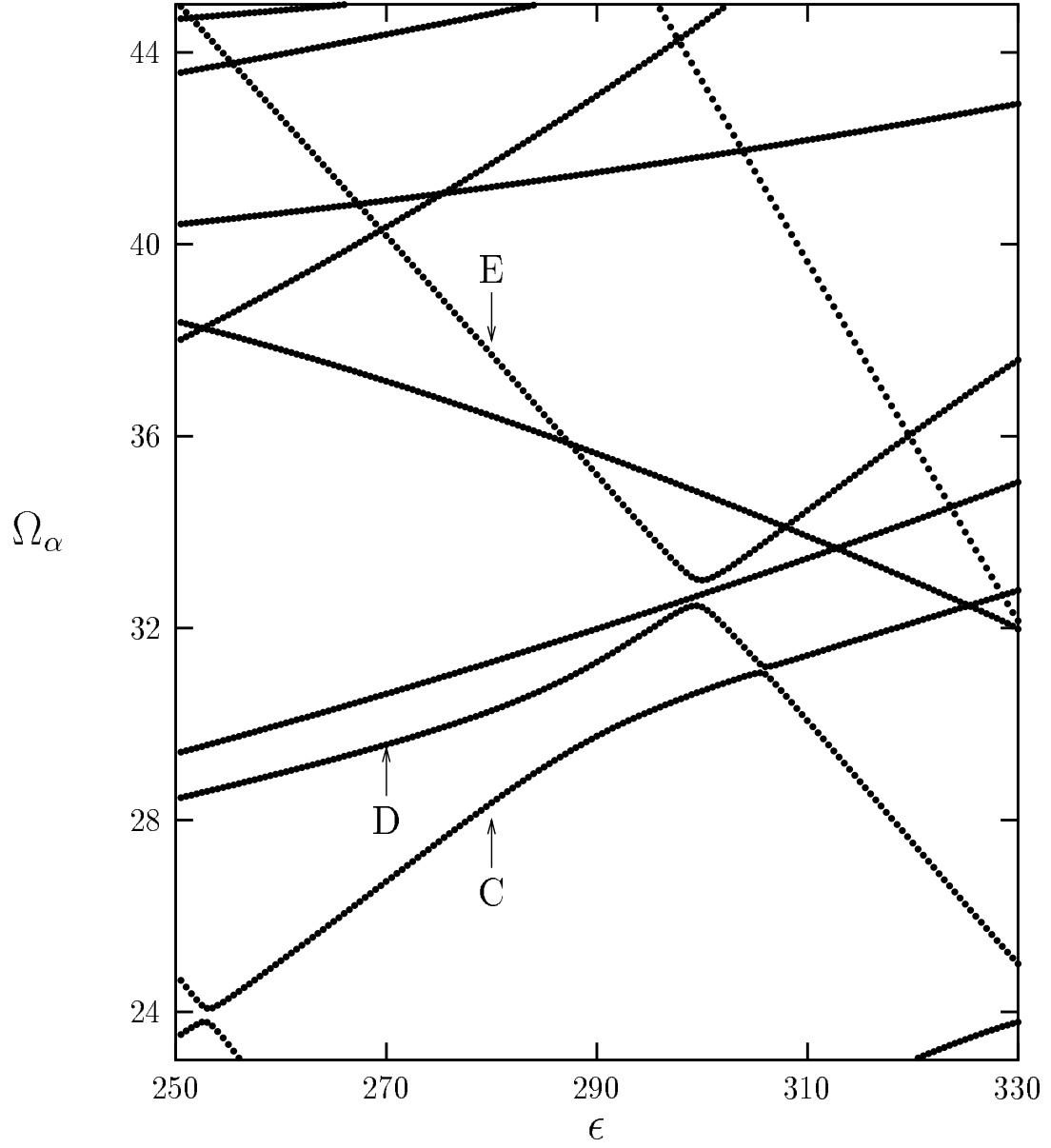


Figure 4.7: Plot of quasienergies Ω_α as a function of field strength showing overlapping avoided crossings involving the states labeled C , D , and E .

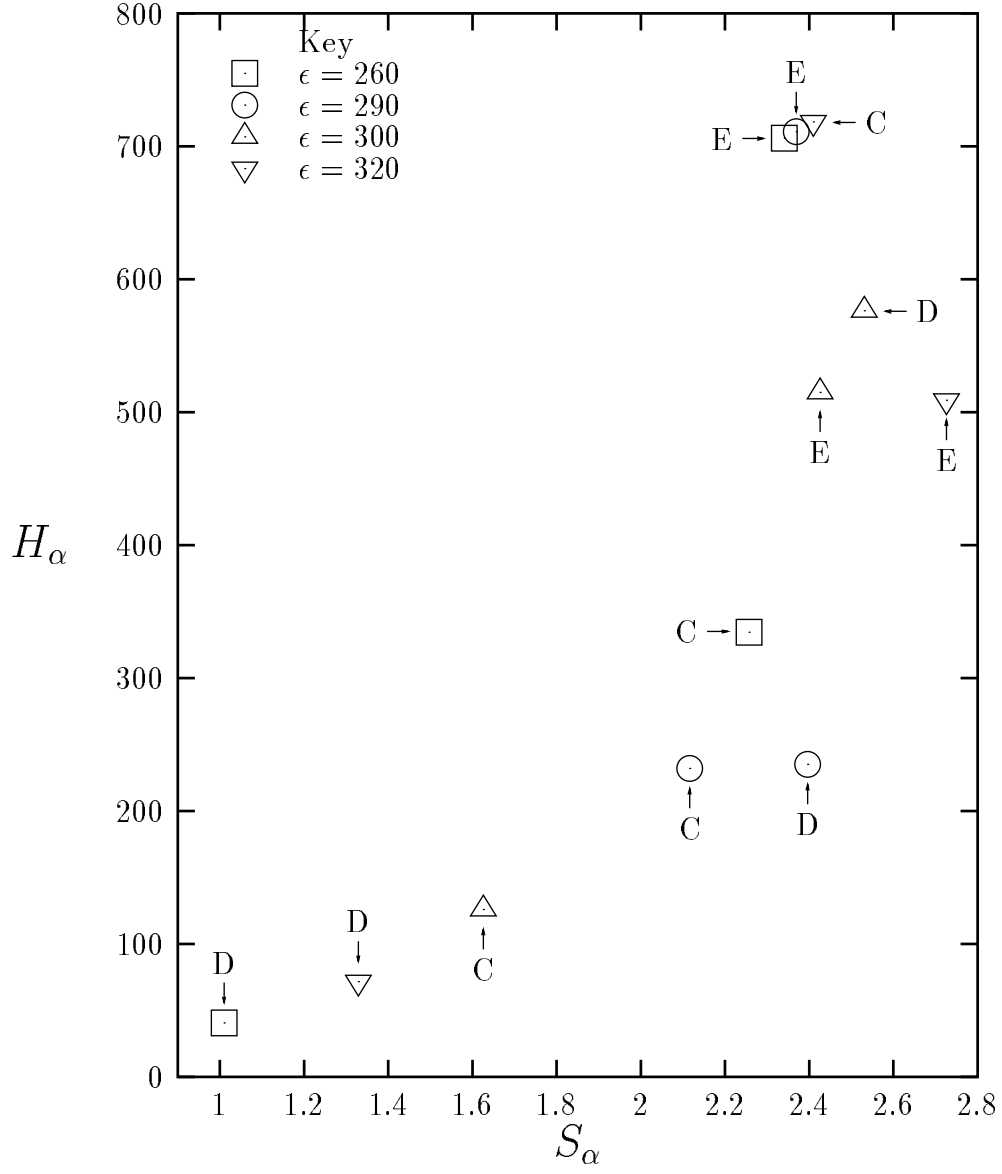


Figure 4.8: Plot of H_α vs. S_α for the states labeled C , D , and E in Fig. 4.7 at four field strengths. The points for each state undergo complicated motions as ϵ is increased through the overlapping avoided crossings. States C , D , and E at $\epsilon = 320$ should be compared to states E , D , and C , respectively, at $\epsilon = 260$. Note that although C at $\epsilon = 320$ occupies the same spot as E at $\epsilon = 260$, the other two states have moved to higher entropies and more moderate energies.

the system can explain why localized states persist even when the system is highly chaotic.

4.3 Classical Dynamics and Localization

4.3.1 Review of classical dynamics

All time-independent one-dimensional Hamiltonian systems are integrable, but with the addition of a harmonic driving force the possibility for chaos exists in the classical dynamics. In this section we will give a quick review of the classical dynamics of a driven, bound, one-dimensional system. We will focus on how the dynamics changes from regular to chaotic as the strength of the driving field is increased.

As the driving field is increased from zero in these systems, the unperturbed motion of the system is distorted. In certain regions of phase space this distorted motion may have a frequency which is an integral multiple of the driving frequency. This leads to a strong coupling between the system and the driving field, and the creation of a resonance region in strob plots of the classical phase space. Within the resonance region the dynamics of the system is strongly modified so that it resembles the motion of a pendulum. The motion inside these resonance regions is still regular and integrable. However, as the field strength is increased the resonances grow larger and as the two resonances grow toward each other daughter resonances form between them. These daughter resonances form a fractal set that can destroy

the regular motion, causing the dynamics in that region of phase space to become chaotic. It is the creation of this set of daughter resonances leading to chaos that is often referred to as resonance overlap.

Before the resonances overlap the phase space is dominated by Komolgorov-Arnol'd-Moser (KAM) tori, invariant curves that represent fully integrable motion. These KAM tori form an impenetrable boundary which no classical trajectory can cross. When resonances overlap, these KAM tori are destroyed and trajectories can pass through them. Initially the KAM tori will change from a continuous curve to a fractal set of points known as a Cantorus. Chaotic trajectories can diffuse through Cantori, but only very slowly. As the resonances overlap further the fractal set that remains from the original KAM torus will be so small as to provide no barrier to classical trajectories. At this point chaotic trajectories may freely roam throughout the region of resonance overlap.

Periodic orbits also play an important role in the dynamics of these systems. In a driven, 1-D system a periodic orbit means an orbit that returns to its starting point in phase space after an integral number of periods of the driving field. At zero field strength, all periodic orbits are stable, but as soon as the driving field is turned on some periodic orbits will become unstable. When two resonances begin to overlap the periodic orbits in the overlap region may be stable or unstable. Eventually, after the resonance overlap has destroyed all KAM tori in the region and the motion is

fully chaotic, all periodic orbits in the region will be unstable. These periodic orbits play a very important role in determining the dynamics of the corresponding quantum system.

4.3.2 Superscars: classical dynamics and localization

In this section we would like to examine the classical dynamics that underlies the localization of Floquet states in this system. However, we must first distinguish among two different types of localization. Exponentially localized states, such as those described by Anderson localization in disordered systems, are characterized by wavefunctions that fall off exponentially outside of some region of the phase space. At the other end of the localization spectrum is weak localization, often referred to as scarring, in which the quantum state has a high probability density in some particular region of the phase space. Looking at Figure 4.3 it is easy to see that even the state we refer to as delocalized has areas of high probability density, and is thus weakly localized. The state we call localized does not meet the stringent requirements of exponential localization, but it is clearly more localized than the other two states shown in Fig. 4.3 because it occupies a much smaller region of phase space (and covers a much smaller range of energies). We will show in this section that the underlying classical dynamics of the system is responsible for the strong (but not exponential) localization of this state.

Localization of Floquet states can often be directly related to certain properties of the classical dynamics. Floquet states that are in regular regions of the phase space are always localized because they lie along invariant KAM tori. States associated with large (area $> \hbar$) resonances are still localized, because the resonance region is itself regular and so the states are again confined by KAM tori. Resonances that are smaller than \hbar will not usually have localized quantum states associated with them. When resonances overlap, which leads to chaos in the classical motion, the quantum states can delocalize and occupy a larger region of the phase space. However, this does not always happen as soon as there is any overlap. Quantum states can still be confined by Cantori in the classical phase space, even though Cantori do not confine classical trajectories [5, 33, 46]. This is because the localization length of a quantum state, which is the characteristic distance over which the state is spread, is a function of the classical flux through a particular region of phase space. If the flux through a Cantorus is smaller than \hbar , then the quantum state will be blocked by that Cantorus just as it would be blocked by a KAM torus [46]. Even when states are not blocked by KAM tori or Cantori they may remain weakly localized, or scarred, near the unstable periodic orbits of the classical system [39, 47].

All of these explanations revolve around the flow of classical trajectories. If the classical flow of trajectories from the region is prevented or inhibited by some

mechanism (KAM tori or Cantori) then quantum states will likely be localized in that region. Even without any classical barrier some states may be scarred on unstable periodic orbits. Scarring is also associated with the flow of classical trajectories because it occurs when orbits that are near the unstable periodic orbits diffuse through phase space more slowly than those that are not close to a periodic orbit [48]. If nearby trajectories tend to remain close to the unstable periodic orbit for short times then it is more likely that a quantum state will be scarred on that unstable periodic orbit.

In our system we find at least one strongly localized state at $\epsilon = 960$, even though there are no KAM tori or Cantori apparent in the classical dynamics at this field strength. However, there is some inhibition on the flow of classical trajectories from very low energies to higher energies. The reason for this is that the excursion parameter, which is the amplitude of oscillation for a free electron in a periodic electric field, is still small at $\epsilon = 960$. The excursion parameter is given by ϵ/ω^2 in the scaled units of our model. For $\omega = 80$ and $\epsilon = 960$ this is only 0.15 units. This means that an electron placed at rest near the center of the square well would never hit either wall of the well. Its motion would be regular and it would come back to the same point in phase space after each cycle of the driving field. Even for trajectories that have non-zero initial momentum it can sometimes take many cycles of the field before the trajectory collides with one of the walls. For trajectories that

start near the center of the well, the lower their initial energy the longer it will take them before they collide with one of the walls. This phenomenon restricts the flow of classical trajectories from very low energy to higher energies, at least for some finite period of time. This phenomenon is related to scarring because there is a continuous line of unstable (with respect to J) periodic orbits at $J = 0$. Scars from these non-isolated orbits overlap to form the “superscar” [49] observed in Fig. 4.3a.

If this is truly the mechanism that leads to localization in our system, we would expect all localized states to have their support on low-energy basis states, while delocalized states could have support on a wide range of basis states. Fig. 4.9 shows the occupation probabilities for the three states labeled L , M , and D in Fig. 4.2b. State L , which is a strongly localized state, has over 80% of its support on the $n = 1$ and $n = 2$ basis states. State M , which is moderately delocalized, has its support mainly on the $n = 7$ and $n = 3$ basis states but it has some support on several other basis states as well. State D , which is fully delocalized, displays what appears to be a random eigenvector with approximately equal support on every basis state in the chaotic region.

If the Floquet state seen in Fig. 4.3a really is a “superscar”, we would expect trajectories near the line of periodic orbits at $J = 0$ to remain at low values of J for some time while trajectories that are far from $J = 0$ should diffuse rapidly throughout the chaotic region. To see if this actually takes place we calculated

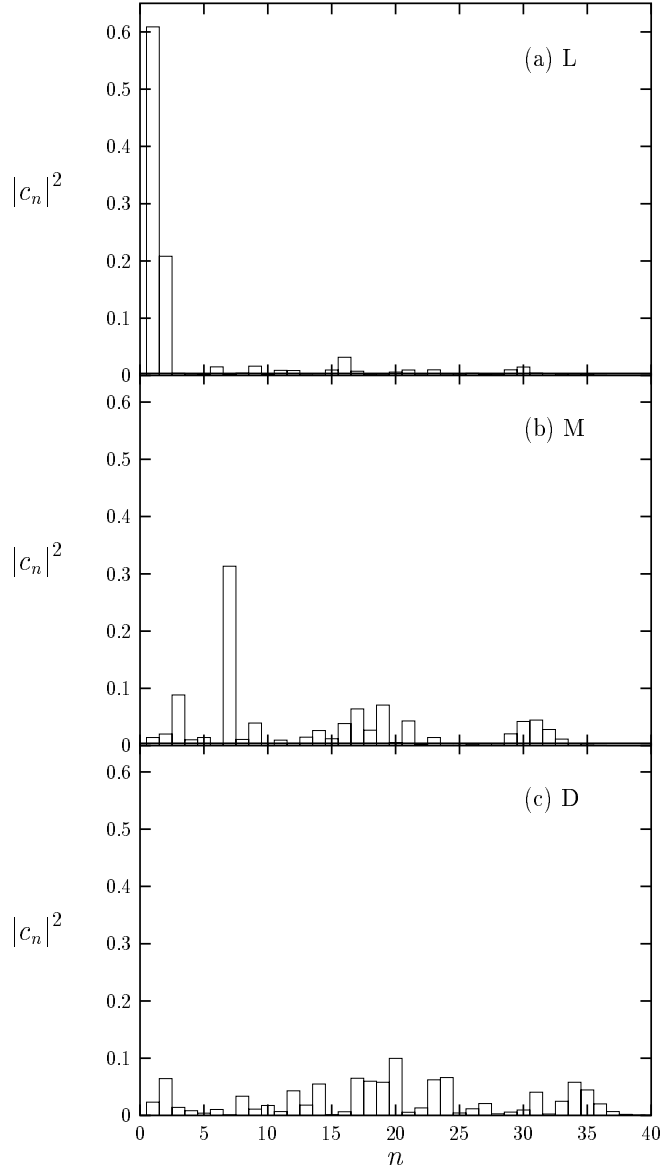


Figure 4.9: Occupation probabilities for the states labeled L , M , and D in Fig. 4.2(b). The n index refers to the eigenstates of the undriven square well, which are used as a basis for calculating these Floquet states (see Eq. 4.2). State (a) L is strongly peaked at $n = 1$ and state (b) M is moderately peaked at $n = 7$, but state (c) D shows no prominent peaks for any n .

8000 trajectories with $\epsilon = 960$ and initial conditions $J_0 = 1$, $J_0 = 7$, or $J_0 = 12$ and evenly distributed over the interval $-\pi \leq \theta \leq \pi$. We plotted the location of these trajectories at times $t = T$ and $t = 5T$, where $T = 2\pi/\omega$ is the period of the driving field. We grouped the resulting points into bins of width $\kappa = 1$ (κ is the effective \hbar of this system) and created a histogram to show the probability (p_j^{cl}) for the resulting points to have a particular value of the action $j = J/\kappa = J$. The results are shown in Figs. 4.10 through 4.12. Each figure shows the plot of the resulting trajectories on the left and the corresponding histogram of probabilities on the right. For trajectories with $J_0 = 1$ (Fig. 4.10) we see that the histogram displays a strong peak at $j = 1$ when $t = T$ and a weaker but still very noticeable peak at $j = 1$ when $t = 5T$. So trajectories near $J = 0$ do tend to remain at low J for several cycles of the field. This behavior accounts for the observed “superscar” state. In Fig. 4.11 we see that trajectories with $J_0 = 7$ have a weak tendency to remain at $j = 7$ after one cycle of the field, but after five cycles the probability is evenly spread across all values of j in the chaotic region. This may explain why state M , which is peaked on $n = 7$, is only moderately delocalized. In Fig. 4.12 we see that trajectories with $J_0 = 12$ have no tendency to remain at $j = 12$ even after only one cycle of the field. This is typical of trajectories that have a high initial value of J and this may be why all strongly localized states at this field strength are low-energy states.

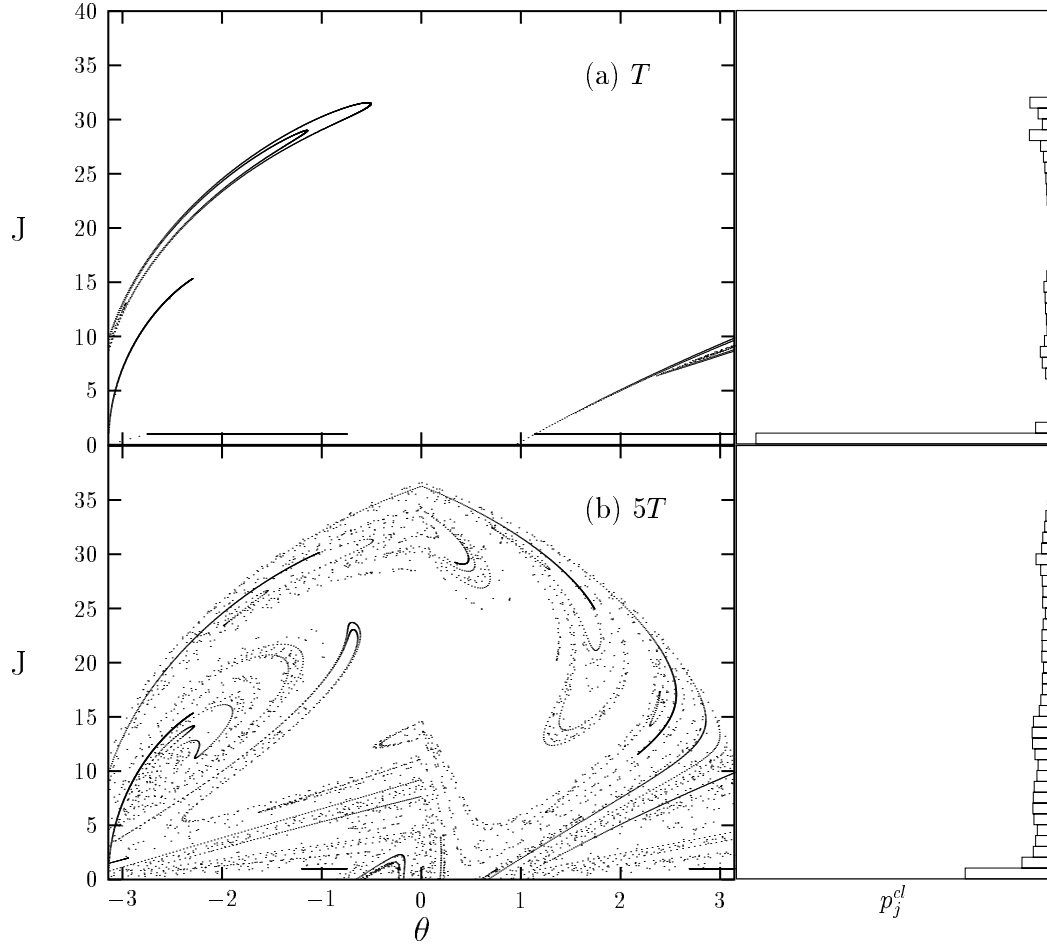


Figure 4.10: Surfaces of section for $\epsilon = 960$ resulting from 8000 classical trajectories with initial conditions $J_0 = 1$ and uniformly spread over the interval $-\pi \leq \theta \leq \pi$. These surfaces of section are shown at times (a) $t = T$ and (b) $t = 5T$, where $T = 2\pi/\omega$ is the period of the driving field. To the right of each surface of section is a histogram showing the distribution of points as a function of $j = J/\kappa$, where $\kappa = 1$ is the effective \hbar . This distribution is strongly peaked at $j = 1$ for $t = T$ and moderately peaked for $t = 5T$.

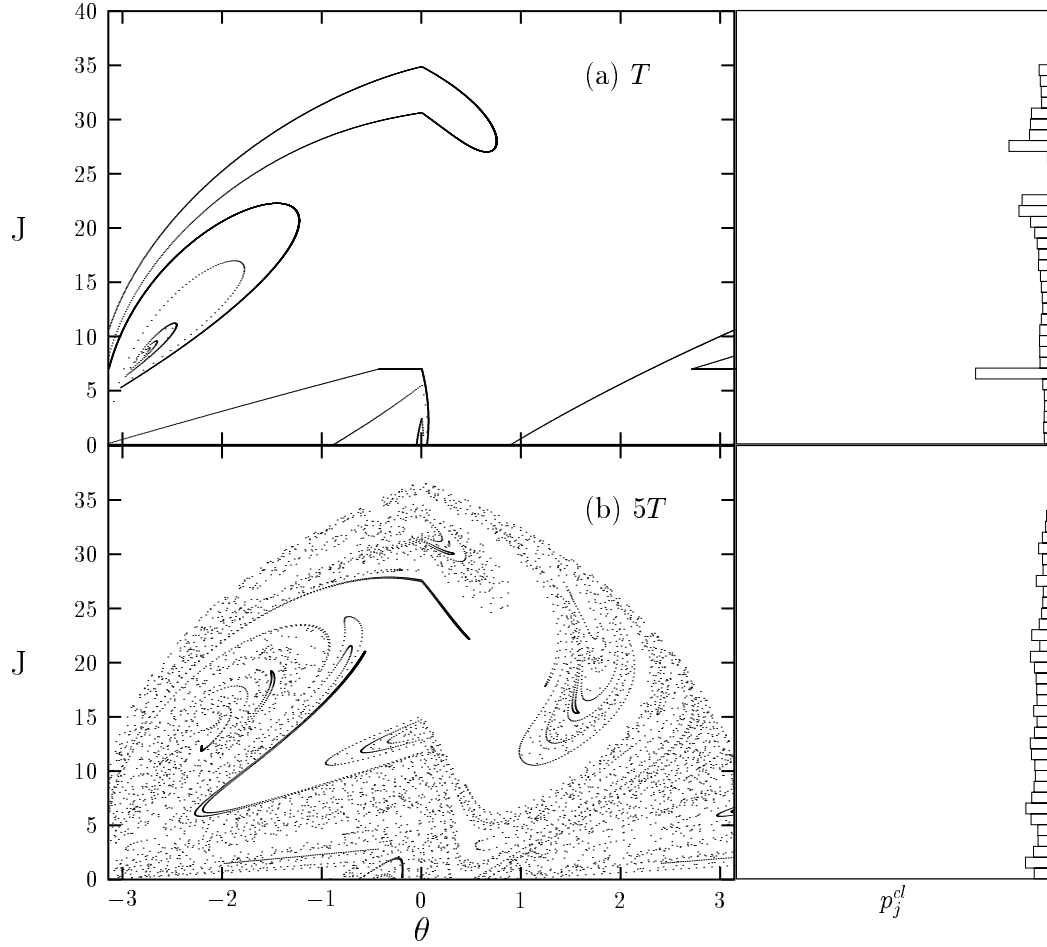


Figure 4.11: Surfaces of section for $\epsilon = 960$ resulting from 8000 classical trajectories with initial conditions $J_0 = 7$ and uniformly spread over the interval $-\pi \leq \theta \leq \pi$. These surfaces of section are shown at times (a) $t = T$ and (b) $t = 5T$, where $T = 2\pi/\omega$ is the period of the driving field. To the right of each surface of section is a histogram showing the distribution of points as a function of $j = J/\kappa$, where $\kappa = 1$ is the effective \hbar . This distribution is moderately peaked at $j = 7$ for $t = T$ but shows no prominent peaks for $t = 5T$.

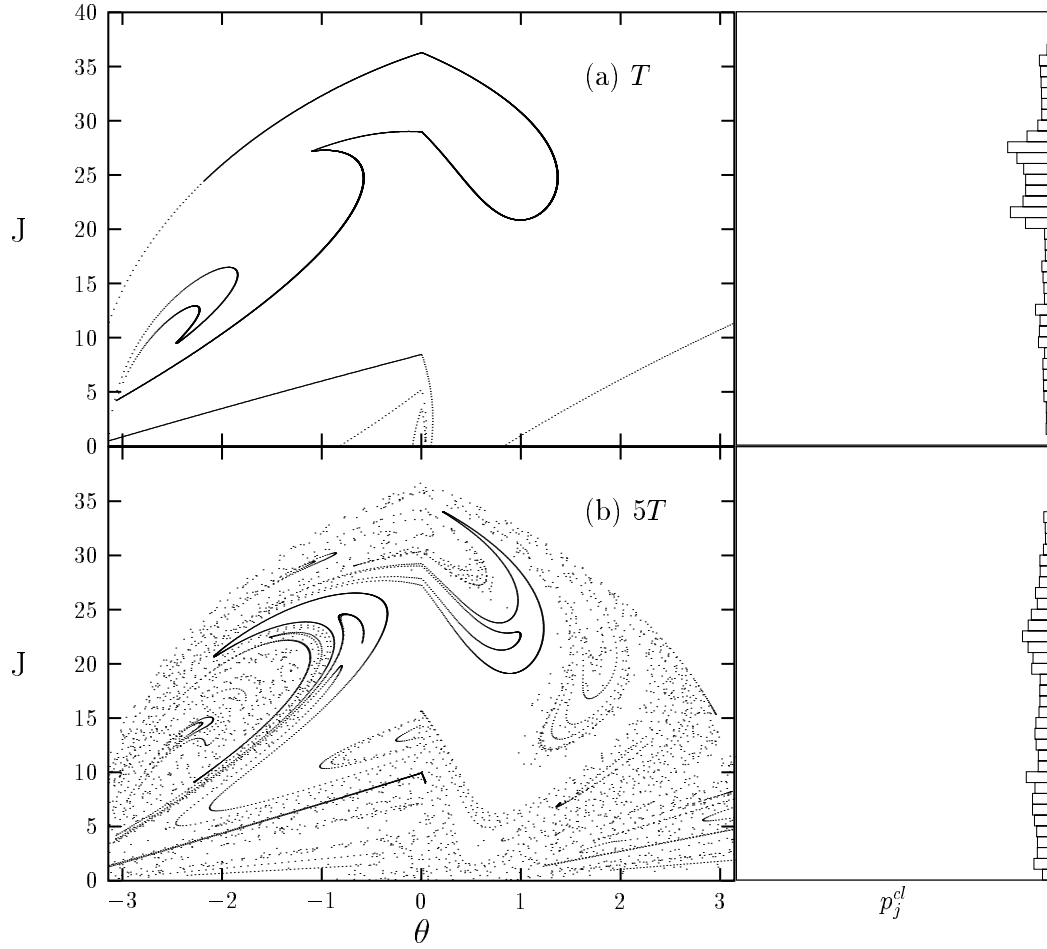


Figure 4.12: Surfaces of section for $\epsilon = 960$ resulting from 8000 classical trajectories with initial conditions $J_0 = 12$ and uniformly spread over the interval $-\pi \leq \theta \leq \pi$. These surfaces of section are shown at times (a) $t = T$ and (b) $t = 5T$, where $T = 2\pi/\omega$ is the period of the driving field. To the right of each surface of section is a histogram showing the distribution of points as a function of $j = J/\kappa$, where $\kappa = 1$ is the effective \hbar . This distribution shows no prominent peaks for $t = T$ or $t = 5T$.

This “superscar” mechanism works well at $\epsilon = 960$ when the excursion parameter is only 0.15 units. But at much higher field strengths the excursion parameter can be 1 or greater and there will no longer be a line of periodic orbits at $J = 0$. At these extremely high field strengths every orbit will be driven into one of the walls each cycle of the field, regardless of the value of J_0 . In Fig. 4.13 we show plots of 8000 trajectories with initial conditions $J_0 = 1$ and evenly distributed in θ . For both $t = T$ and $t = 5T$ it is clear that there is no tendency for the trajectories to remain at $j = 1$. This may explain why there are no strongly localized states visible in Fig. 4.2c.

4.4 Eigenvalue Statistics and Chaos

So far we have primarily discussed the changes in the eigenstates of a quantum system that are brought about by classical chaos. In this section we will review some research on qualitative changes that occur in the spectrum of quantum eigenvalues as a result of chaos in the classical system.

A time-independent one-dimensional system needs only one constant of motion to be integrable, and in these systems energy is always conserved. Hence all one-dimensional systems are integrable. A driven one-dimensional system, though, can be viewed as a two-dimensional system in what is known as extended phase space, where time is treated as a second coordinate variable. These driven systems,

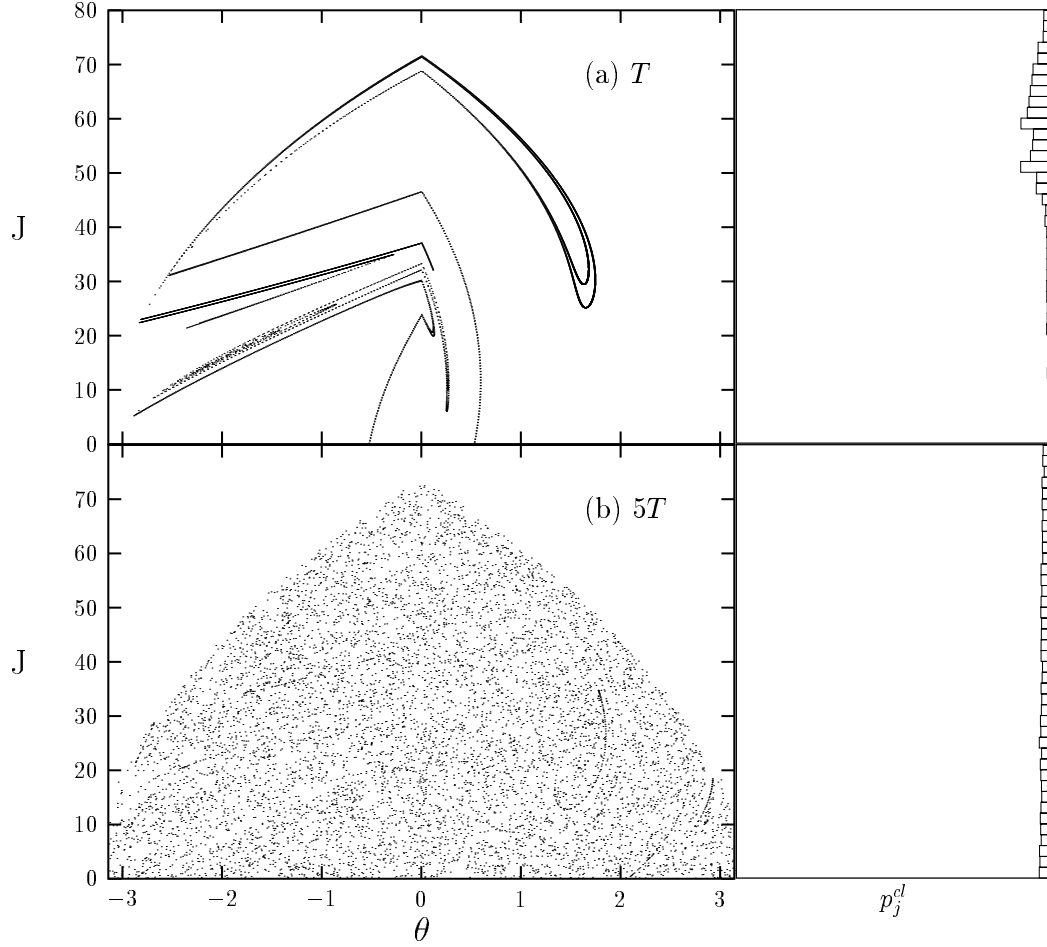


Figure 4.13: Surfaces of section for $\epsilon = 6400$ resulting from 8000 classical trajectories with initial conditions $J_0 = 1$ and uniformly spread over the interval $-\pi \leq \theta \leq \pi$. These surfaces of section are shown at times (a) $t = T$ and (b) $t = 5T$, where $T = 2\pi/\omega$ is the period of the driving field. To the right of each surface of section is a histogram showing the distribution of points as a function of $j = J/\kappa$, where $\kappa = 1$ is the effective \hbar . This distribution shows no prominent peaks for $t = T$ or $t = 5T$.

then, generally do have one “conserved” quantity in this extended phase space, but they must have two in order to be integrable. Similarly, the quantum versions of these systems have properties that depend upon whether two good quantum numbers exist in the system or only one. In particular, it is known that regular states that have two good quantum numbers will form a series of uncorrelated eigenvalue sequences known as a mixed sequence. For each value of the first quantum number, there will be a sequence of values for the second quantum number. However, if one quantum number is destroyed then the entire system will be comprised of a single pure sequence. This change can be easily identified by studying the statistical distribution of the spacing between neighboring eigenvalues. Mixed sequences have spacings that follow the Poisson distribution, while pure sequences have spacings that follow a distribution derived from random-matrix theory [50]. Thus, the change from Poisson to random-matrix statistics indicates a change from integrable (2 good quantum numbers) to chaotic (only 1 good quantum number).

Just as the overlap of classical resonances destroys a local constant of motion, it is the overlap of the corresponding quantum resonances that destroys one of the quantum numbers of the system. As mentioned earlier, the overlap of avoided crossings in the eigenvalue spectrum is the signature of quantum resonance overlap [10]. Spectral repulsion, which is the tendency of eigenvalues in a pure sequence to repel each other, is associated with the extended states that are found after quantum reso-

nances overlap [33]. So there is a close relationship between eigenvalue statistics and localization. When the eigenstates are strongly localized the eigenvalues statistics tend toward a Poisson distribution, but for delocalized eigenstates the distribution is of the random-matrix type [9, 51].

4.5 Avoided crossings and classical dynamics

We have shown the importance of avoided crossings, and particularly overlapping avoided crossings, in creating delocalized and stochastic eigenstates in a quantum system. We have also discussed how quantum resonance overlap, which is associated with overlapping avoided crossings, leads to changes in the eigenvalue spectrum of the quantum system. Clearly avoided crossings play a key role in the transition from regular quantum dynamics to quantum chaos. Since avoided crossings are associated with quantum resonances, and those quantum resonances are related to resonances in the classical phase space, we expect a relationship between avoided crossings and the motion in the classical phase space. In fact, semiclassical methods have even been used to predict the occurrence of avoided crossings in the corresponding quantum system [52]. In this section we will review what is known about the relationship between avoided crossings and classical dynamics.

In Section 2.3 we saw that at very low field strengths the eigenvalue curves of our system crossed each other frequently, but at higher field strengths we begin to

see avoided crossings in the spectrum. This is an indication that avoided crossings are associated with classical chaos, which only becomes prominent at higher field strengths. It has been found that avoided crossings only occur between states that occupy regions in the phase space that are very close together [37]. This proximity is best seen by plotting Husimi distributions for the states that are involved. If the Husimi distributions are close together then the states can have an avoided crossing. If two states do not have Husimi distributions that are close together then they can only have an apparent crossing, where the two eigenvalue curves actually cross [39]. A state that is fully enclosed by KAM tori generally cannot overlap with a state that is outside the KAM tori and thus can only be involved in apparent crossings with these outside states [53], although quantum tunneling can sometimes permit states confined by KAM tori to have avoided crossings with other states. The destruction of classical KAM tori, and the corresponding overlap of quantum resonances, allows previously isolated states to occupy the same region of phase space and thus have avoided crossings [37]. As the field strength is increased and the classical system becomes increasingly chaotic, the eigenvalue curves of the quantum system undergo more frequent avoided crossings and fewer apparent crossings. It is generally true that pure sequences have only avoided crossings, while mixed sequences have mostly apparent crossings. So the proliferation of avoided crossings as the field strength is increased is an indication of the change from Poisson to random-matrix statis-

tics. Thus we see that overlapping avoided crossings, which are closely related to resonance overlap and chaos in the classical system, lead directly to delocalization, stochasticity, and changes in eigenvalue spectrum in the quantum system.

4.6 Matrix Picture of the Transition to Chaos

We have seen that avoided crossings occur when two states that are located close to each other in phase space exchange their structure as ϵ is increased. Obviously changes of this nature should be reflected in the Floquet matrix (the time evolution operator over one cycle of the field). The structure of any matrix, though, is basis dependent. To examine how the Floquet matrix changes its structure as ϵ is increased we must choose some basis in which to represent the Floquet matrix. A clear choice of basis is provided by a quick look at the perturbation theory for time-periodic systems.

Our driven square well system has a Hamiltonian of the form $H = H_0 + \epsilon \hat{x} f(t)$, where H_0 is a time independent Hamiltonian, \hat{x} the dipole operator, ϵ is the field strength, and $f(t + T) = f(t)$. For a slightly higher value of the field strength, $\epsilon + \delta\epsilon$, the Hamiltonian is $H = H_0 + \epsilon \hat{x} f(t) + \delta\epsilon \hat{x} f(t)$, or $H^{\epsilon+\delta\epsilon} = H^\epsilon + \delta\epsilon \hat{x} f(t)$, where H^ϵ stands for the full Hamiltonian when the field strength is ϵ . Using an extended phase space approach, where time is treated as a second spatial coordinate, we can apply *time-independent* perturbation theory to find the quasienergies and

Floquet states associated with $H^{\epsilon+\delta\epsilon}$ provided we know the Floquet states and quasienergies associated with H^ϵ [54]. If we denote the eigenstates of H^ϵ by $|\psi_\alpha^\epsilon\rangle$ and the quasienergies associated with these states by Ω_α^ϵ , we have

$$\Omega_\alpha^{\epsilon+\delta\epsilon} = \Omega_\alpha^\epsilon + \delta\epsilon \langle \langle \psi_\alpha^\epsilon | \hat{x} f(t) | \psi_\alpha^\epsilon \rangle \rangle + O(\delta\epsilon^2) \quad (4.4)$$

and

$$|\psi^{\epsilon+\delta\epsilon}\rangle = |\psi^\epsilon\rangle + \delta\epsilon \sum_\beta \frac{\langle \langle \psi_\beta^\epsilon | \hat{x} f(t) | \psi_\alpha^\epsilon \rangle \rangle}{\Omega_\alpha^\epsilon - \Omega_\beta^\epsilon} |\psi_\beta^\epsilon\rangle + O(\delta\epsilon^2) \quad (4.5)$$

where

$$\langle \langle f | g \rangle \rangle \equiv \frac{1}{T} \int_0^T dt \langle f | g \rangle. \quad (4.6)$$

Inspection of these equations shows that it is the matrix $\langle \langle \psi_\beta^\epsilon | \hat{x} f(t) | \psi_\alpha^\epsilon \rangle \rangle$ that determines the change in the eigenvalues and eigenvectors as the strength of the field is increased. This matrix describes the coupling between Floquet states and we will refer to this matrix as the coupling matrix during the remainder of this chapter. Looking at how this matrix changes as the field strength is increased provides a good picture of how the quantum dynamics changes from regular to chaotic.

At very low ϵ the Floquet states will be almost identical to the eigenstates of H_0 , so the coupling matrix is essentially just the dipole matrix in the basis of square well eigenstates (see Eq. 2.10). This matrix has large elements only near the diagonal. As the field strength is increased the coupling matrix begins to change. When a resonance forms in the classical phase space the quantum states associated

with that resonance will become strongly coupled. As these resonances overlap and KAM tori are destroyed, the classical flow between different regions of phase space increases and this allows for stronger coupling between the Floquet states that occupy those regions. As the chaotic region in the phase space grows large the coupling between all of the eigenstates associated with the chaotic region will become strong. If the eigenstates are ordered by increasing energy, this gives the coupling matrix a block-diagonal form, with the low-energy chaotic states forming one block that is essentially random while the high-energy regular states form another block which still has large elements only near the diagonal. As the chaotic region grows in the classical phase space, the chaotic block of the coupling matrix will also grow as new states are added to the chaotic group. A matrix of this form will have eigenvalue statistics intermediate between Poisson and random-matrix, because the states in the chaotic block will have eigenvalues that conform to random-matrix statistics while those in the regular block will follow Poisson statistics. A model for eigenvalue statistics in systems that exhibit distinct regular and chaotic regions was suggested by Berry and Robnik [55]. At intermediate field strengths, when there is still some localization, the eigenvalue statistics may deviate significantly from the Berry-Robnik model. Some studies have shown that localization can lead to eigenvalue spectra that have band-random matrix statistics [9].

This progression from an essentially diagonal matrix to a matrix with a ran-

dom chaotic block and a diagonal regular block is illustrated in Fig. 4.14. We calculated the matrix $\langle \psi_\alpha^\epsilon | \hat{x} | \psi_\beta^\epsilon \rangle$ for four different field strengths. While this is not exactly the same as the coupling matrix described above (since it leaves out $f(t)$ and it is not time-averaged), it suffices to illustrate the qualitative changes in the coupling matrix. Fig. 4.14 shows contour plots of $|\langle \psi_\alpha^\epsilon | \hat{x} | \psi_\beta^\epsilon \rangle|^2$. At $\epsilon = 100$ (Fig. 4.14a) the matrix elements are large mainly on the diagonal, but the strong coupling of the states associated with the $M = 1$ classical resonance (see Fig. 4.1a) is visible at $\alpha = \beta = 16$. At $\epsilon = 320$ (Fig. 4.14b) the chaotic block is beginning to form, but the mixed phase space still provides some barriers to the classical flow of trajectories and this causes the matrix to have a patchy appearance. The patchiness of the matrix is directly related to the fact that there are still several localized states at this field strength. In Fig. 4.14c, we see that the chaotic block is fully formed for $\epsilon = 960$. Finally, at $\epsilon = 6400$ (Fig. 4.14d) we see that the chaotic block has grown much larger, just as the chaotic region in the classical phase space has grown (see Fig. 4.1c).

The progression from regular classical motion to chaos in this system is very similar to that seen in other bound, 1-D, time-periodic systems. We expect that the quantum dynamics of this system is also characteristic of this class of systems. The matrix description of our system that is given above provides a clear picture of how the quantum system follows the dynamics of the classical system by increasing

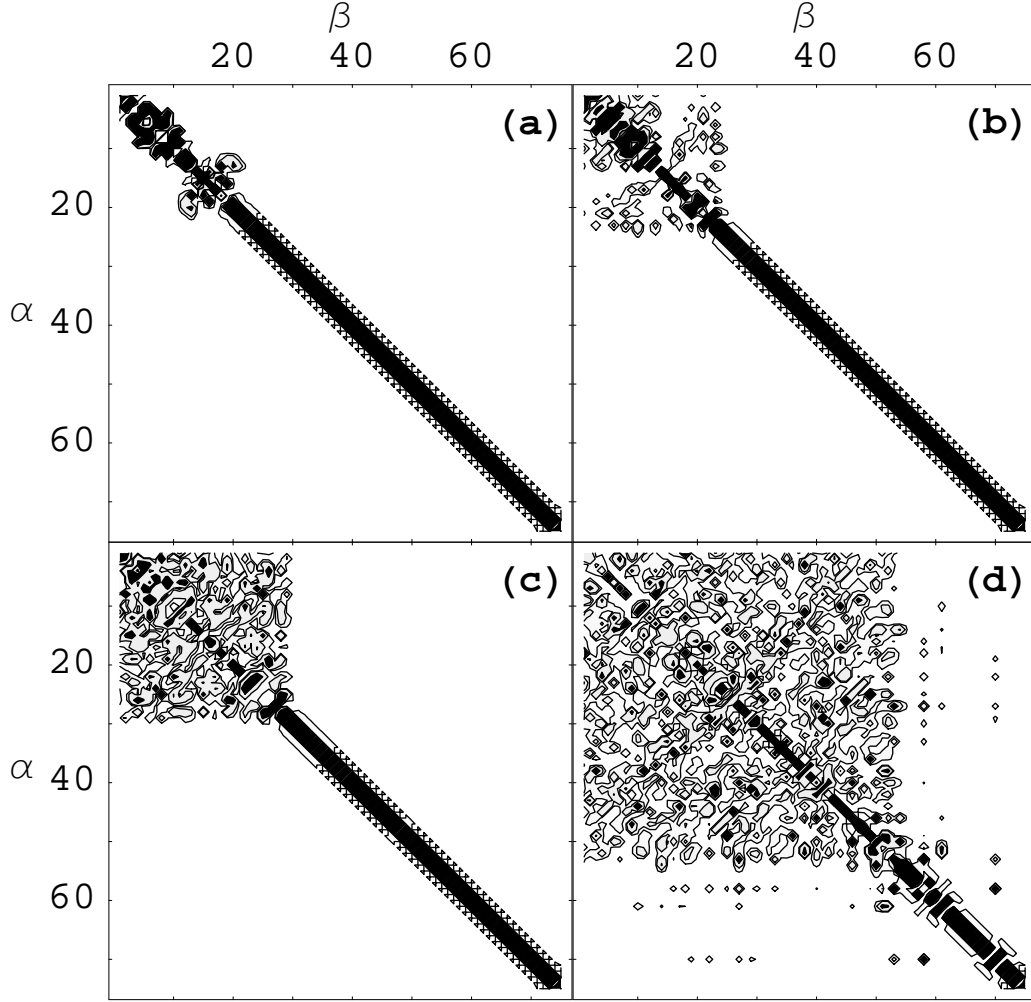


Figure 4.14: Dipole matrix $|\langle \psi_\alpha^\epsilon | \hat{x} | \psi_\beta^\epsilon \rangle|^2$ in the Floquet basis for four different field strengths. The Floquet states are ordered by values of H_α (see Eq. 4.3), with state $\alpha = 1$ having the lowest value of H_α . The dipole matrix is shown as a contour plot with contours at 0.001, 0.005, and 0.0025. The matrix is shown for field strengths (a) $\epsilon = 100$, (b) $\epsilon = 320$, (c) $\epsilon = 960$, and (d) $\epsilon = 6400$. At $\epsilon = 320$ the states in the chaotic region (low α and β) are not all strongly coupled, but at $\epsilon = 960$ and $\epsilon = 6400$ all of the chaotic states are strongly coupled. The region of strong coupling grows as the size of the chaotic region grows. Refer to Figs. 2.1 and 4.1 for strobe plots at these field strengths.

the coupling between states inside the chaotic region of phase space. This stronger coupling leads these states to have numerous overlapping avoided crossings with each other, causing them to mix their structure and eventually take on a statistical character. As the coupling between the states becomes stronger and the eigenvectors become increasingly stochastic, the eigenvalue spectrum will undergo a transition from Poisson to random-matrix statistics and the transition to chaos in the system will be complete.

The relationship between classical and quantum dynamics in this class of systems could be better understood if the connection between quantum eigenstates and periodic orbits of the classical motion was clearer. At zero field strength the connection between a single quantum eigenstate and a single invariant torus in the classical phase space is made clear by EBK quantization. The Gutzwiller trace formula establishes a connection between the set of all quantum eigenstates and the set of all unstable periodic orbits when the dynamics of the system is fully chaotic. It may be possible to think of periodic orbits as a basis upon which the quantum eigenstates are constructed [56]. At zero field strength each quantum state is built on a single periodic orbit (invariant torus). As the field strength is increased the quantum system passes through avoided crossings which can mix the quantum states so that they are no longer associated with only one periodic orbit. In the limit of global chaos each quantum state would be such a complicated mixture of periodic

orbits that one could only clearly associate the set of all quantum states with the set of all periodic orbits. This picture has a great deal of aesthetic appeal since it would seem to explain the phenomenon of scarring, but at this point the connection between periodic orbits and quantum states is not clear for systems that are intermediate between integrability and global chaos. However, some progress has been made in using semiclassical methods to investigate eigenvalue spectra for mixed phase-space systems [57] and avoided crossings [58, 59].

Chapter 5

Creation of Quasienergy

Resonance States

In the previous chapters we have studied a closed quantum system driven by a strong periodic field. Our primary motivation for studying this system was to gain insight into quantum-classical correspondence in a simple quantum system with a chaotic classical counterpart. However, we were also motivated by recent experimental work with ultra-high intensity lasers. Many of these experiments involve irradiating atoms with these intense lasers [15]. Atoms are, of course, open quantum systems. The possibility of ionization, which does not exist in the model discussed in the previous chapters, leads to many new phenomena.

One of the new phenomena observed in these systems is the stabilization of

atoms in intense laser fields. Stabilization is characterized by a *decrease* in the probability for an electron to ionize as the laser intensity is *increased*. This effect was first discovered in theoretical studies of the interaction between high-frequency lasers and atoms [60], but this stabilization has been observed in recent experiments [16, 17]. Studies of the underlying classical dynamics of these systems using one- and two-dimensional models have shown that the classical motion can often account for the increased stability of the atom at higher laser intensities [16, 61].

Floquet theory (see App. A) provides the natural framework in which to study these systems, as it did for the driven square well system. In open quantum systems, though, the Floquet eigenstates have finite lifetimes. In some cases the Floquet states of the system can be localized on stable structures in the classical phase space [62], and this can lead to stabilization because these Floquet states have very long lifetimes. In this case, stabilization would also be predicted by the classical dynamics. However, there are often significant differences between the classical and quantum dynamics of chaotic systems. One of the most striking examples of this is scarring, where quantum eigenstates have higher probability to be found near the locations of unstable periodic orbits in the classical phase space [13, 44]. The scarring of Floquet states on unstable periodic orbits might make it possible for a quantum system to exhibit stabilization even when the corresponding classical dynamics is unstable. Some earlier studies indicate that stabilization can be associated with

states that are scarred on unstable or weakly stable periodic orbits [47, 63].

In this chapter we use two versions of complex-coordinate scaling to calculate the Floquet eigenvalues and eigenstates of a system consisting of an inverted Gaussian potential and a monochromatic driving field. The number of resonance states, which are localized Floquet states, increases as the field strength is increased. This behavior is a sign of stabilization in this system. By examining the Husimi distributions (see App. B) of the resonance states we have determined that the newly created states are associated with unstable periodic orbits of the classical motion. The behavior of these periodic orbits as the field strength is increased may explain why there are more resonance states at high field strengths than at low field strengths. In this chapter we also examine an avoided crossing between resonance states. We find that this avoided crossing is very similar in character to the sharp avoided crossing studied in Ch. 3 and does not result in permanent delocalization of the resonance states that are involved.

5.1 Driven Inverted Gaussian Model

The model we will study is an inverted Gaussian potential interacting with a monochromatic driving field. In the previous chapters we have used the length gauge for describing the interaction between the electron and the driving field, but in this chapter we will use instead the radiation gauge because it is easier to carry out

complex-scaling calculations in this gauge. The length gauge and radiation gauge are related by a canonical transformation described in Appendix C. The Hamiltonian of the system in atomic units (which are used throughout the chapter) is

$$H = \frac{1}{2} \left(p - \frac{\epsilon}{\omega} \sin(\omega t) \right)^2 - V_0 \exp(-(x/a)^2) \quad (5.1)$$

where $V_0 = 0.63$ a.u. and $a = 2.65$ a.u. The strength of the driving field is ϵ and the driving frequency is ω . It is useful to write this as $H = H_0 + V$, where

$$H_0 = \frac{p^2}{2} - V_0 \exp(-(x/a)^2) \quad (5.2)$$

and

$$V = -\frac{\epsilon}{\omega} p \sin(\omega t) + \frac{\epsilon^2}{2\omega^2} \sin^2(\omega t). \quad (5.3)$$

The second term on the right-hand side of Eq. 5.3 has no effect on the classical dynamics of the system and only results in an overall phase shift in the quantum system.

Figure 5.1 illustrates the classical dynamics of this system. The strobe plots in Fig. 5.1 are calculated by evolving a set of trajectories, all with initial momentum $p = 0$, over many cycles of the field and plotting the location of each trajectory when $t = 2\pi n/\omega$ (after each full cycle of the field). For $\epsilon = 0$ the motion is regular and bounded for negative energies. Motion at positive energies is unbounded. Figs. 5.1a, 5.1b, and 5.1c show the classical strobe plots for $\omega = 0.0925$ a.u. and $\epsilon = .038$, .065, and .09 a.u., respectively. As ϵ is increased the region near $(x = 0, p = 0)$

remains stable, but the size of the stable region gets smaller as ϵ is increased. The filled squares in Fig. 5.1 indicate the locations of the periodic points in the strob plot and the arrows show $x = \alpha$ and $x = 2\alpha$, where $\alpha = \epsilon/\omega^2$ is the excursion parameter of a free electron in the field. The trajectories of these periodic orbits are shown in Figures 5.2, 5.3, and 5.4. At these parameter values the periodic orbit at $(0, 0)$ is stable while the other two periodic orbits are unstable. As ϵ is increased the unstable periodic orbits move toward larger values of x , remaining close to $x = \alpha$ and $x = 2\alpha$. For very high frequency driving fields two of the periodic orbits can be stable while the third is unstable. This is illustrated in Fig. 5.1d, which shows the classical strob plot for $\omega = 2$ a.u. and $\epsilon = 42$ a.u. The value of α in Fig. 5.1d is the same as in Fig. 5.1c, but at the higher frequency the periodic orbit located near $x = 2\alpha$ is a stable elliptic orbit surrounded by regular motion. The periodic orbit at $x = \alpha$ is hyperbolic.

The quantum dynamics of this system has been the subject of several investigations during the past decade. The resonance states of this system were first calculated by Bardsley and Comella in 1989 [64]. More recent studies have focused on high-harmonic generation (HHG) in this system [65, 66]. It is the findings of , Moiseyev, and Kosloff [67], hereafter BMK, that have the most relevance to our work. They found that the number of resonance states in this system increased as the field strength was increased over a certain range. BMK explain the cre-

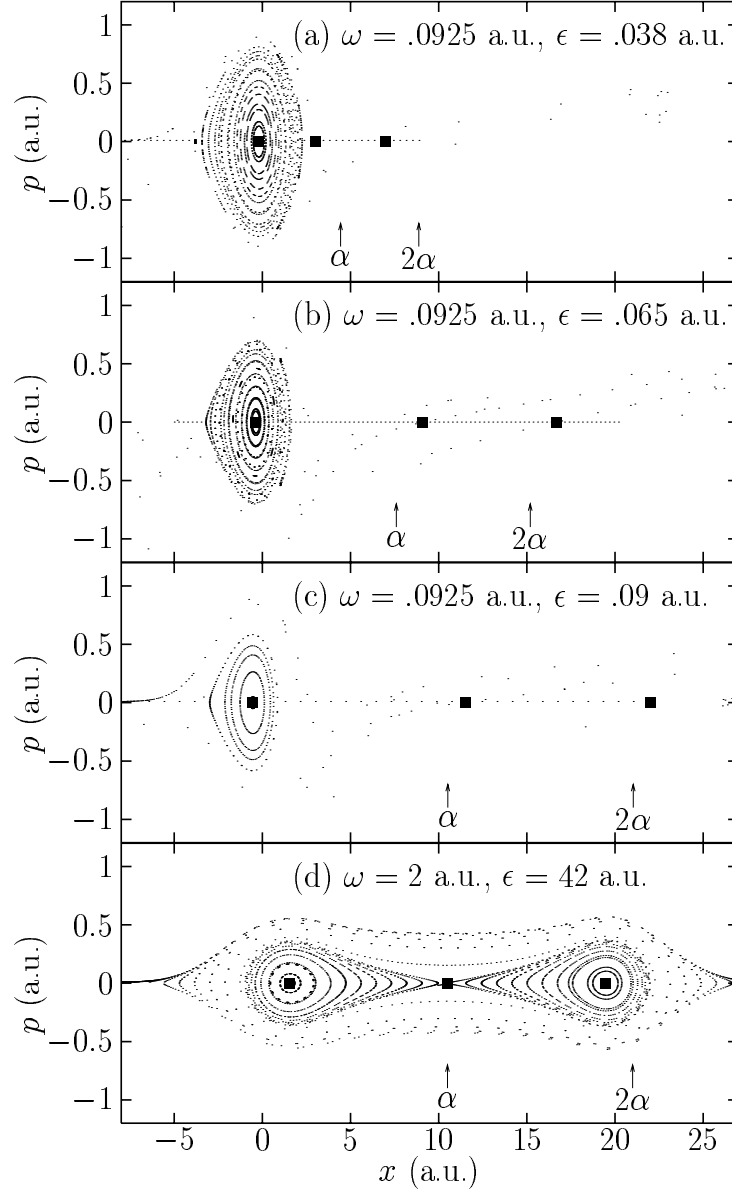


Figure 5.1: Strobe plots of the classical dynamics for the driven inverted Gaussian system. The initial conditions used to generate the plots all lie on the line $p = 0$. α is the classical excursion parameter for a free electron the field. The locations of the periodic orbits (stable and unstable) are indicated by filled squares.

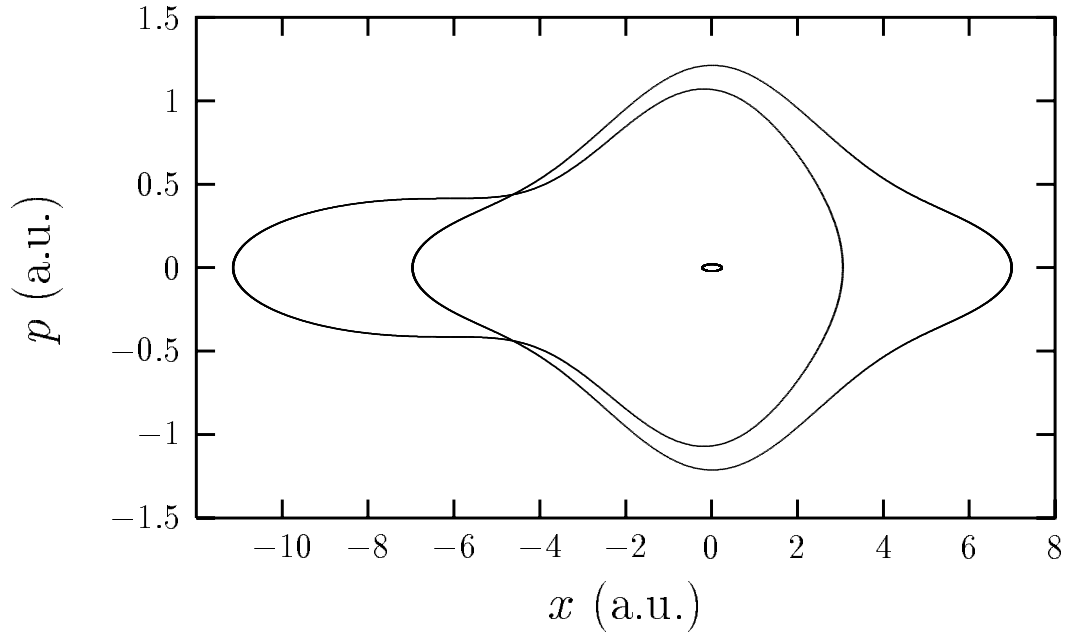


Figure 5.2: Trajectories of periodic orbits in the driven inverted Gaussian system for $\omega = 0.0925$ a.u. and $\epsilon = 0.038$ a.u. The small oval near $(x = 0, p = 0)$ is the stable periodic orbit. The larger orbits are unstable. The initial conditions for these periodic orbits are $(x = -0.224, p = 0)$, $(x = 3.046, p = 0)$, and $(x = 6.977, p = 0)$ in atomic units.

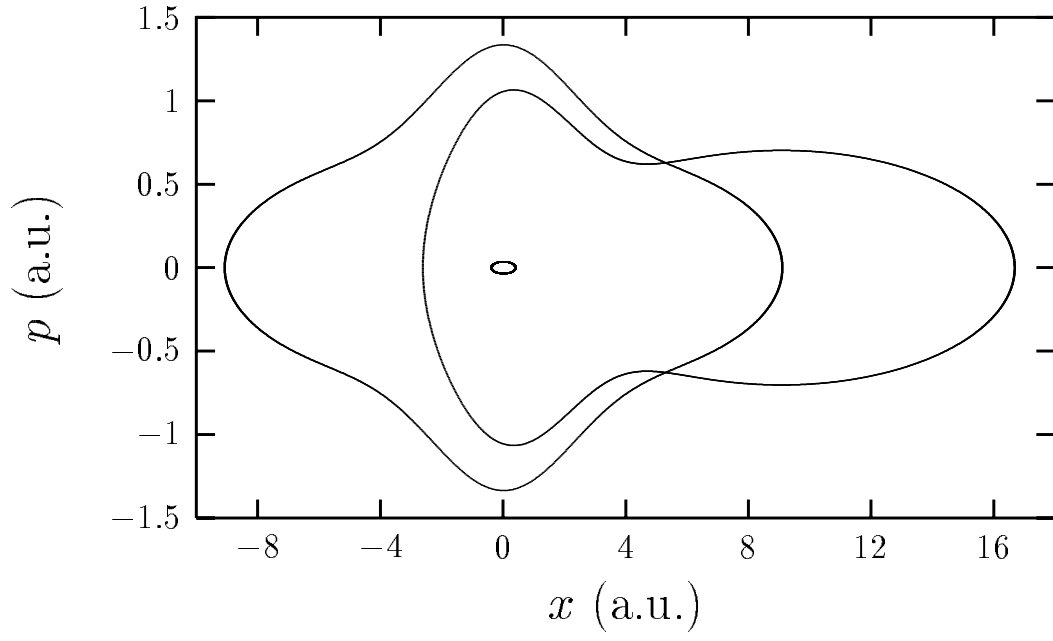


Figure 5.3: Trajectories of periodic orbits in the driven inverted Gaussian system for $\omega = 0.0925$ a.u. and $\epsilon = 0.065$ a.u. The small oval near $(x = 0, p = 0)$ is the stable periodic orbit. The larger orbits are unstable. The initial conditions for these periodic orbits are $(x = -0.390, p = 0)$, $(x = 9.092, p = 0)$, and $(x = 16.668, p = 0)$ in atomic units.

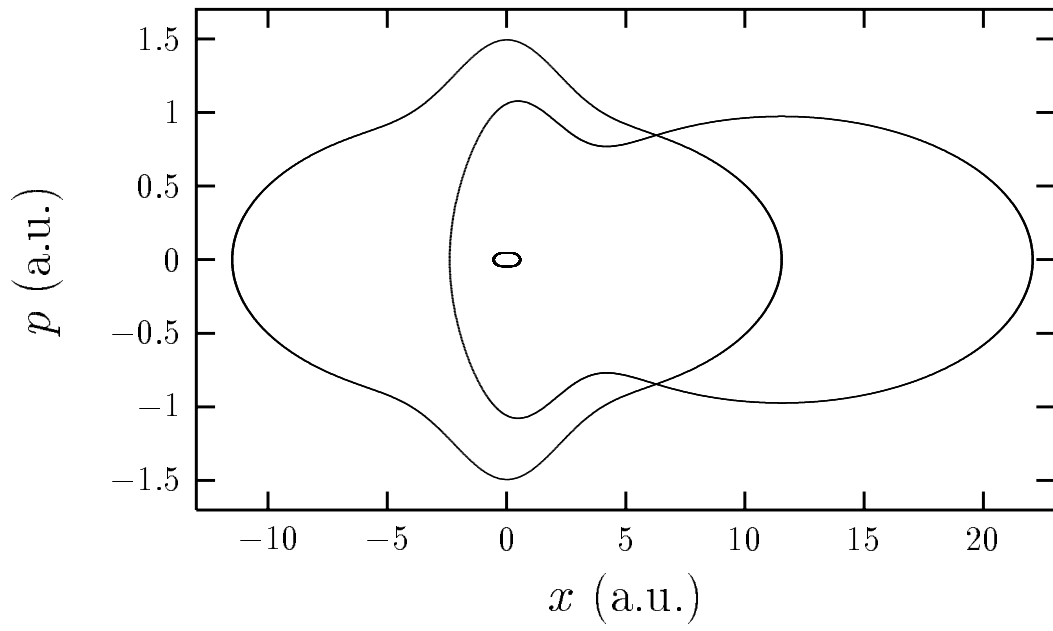


Figure 5.4: Trajectories of periodic orbits in the driven inverted Gaussian system for $\omega = 0.0925$ a.u. and $\epsilon = 0.09$ a.u. The small oval near $(x = 0, p = 0)$ is the stable periodic orbit. The larger orbits are unstable. The initial conditions for these periodic orbits are $(x = -0.555, p = 0)$, $(x = 11.517, p = 0)$, and $(x = 22.040, p = 0)$ in atomic units.

ation of new resonance states as the field strength is increased by analyzing the dynamics of the time-averaged system in a reference frame that oscillates with a free electron in the driving field, known as the Kramers-Henneberger or K-H frame [68]. They found qualitative agreement in that the number of bound states in the time-averaged potential increases as the field strength is increased. However, the quantitative agreement was not very good. This is not surprising since the time-averaged K-H description is only accurate for very high frequency driving fields. Since the frequency of the driving field used by BMK and in this work ($\omega = .0925$ a.u.) is lower than the frequency of motion for two of the bound states in the undriven system (.4451 a.u. and .1400 a.u.), the time-averaged K-H description is not quantitatively accurate. It is somewhat surprising that the time-averaged K-H description is qualitatively accurate because the classical motion of the system in the time-averaged K-H frame is stable while the classical motion of the exact system is largely unstable. For $\alpha > 1$ the time-averaged potential in the K-H frame is a double well with minima separated by approximately 2α . Motion in this double well would be quite different from that seen in the strobe plots in Fig. 5.1a-c (although it would closely resemble the motion shown in Fig. 5.1d, which is at a frequency that is high enough for the time-averaged K-H description to be valid). Our goal in this chapter is to find an alternative explanation for the creation of resonance states as ϵ is increased in this system, an explanation that does not rely on the time-averaged

K-H description.

5.2 Complex Coordinate Scaling

In recent years the technique of complex coordinate scaling has been used extensively in the study of open quantum systems. In this section we will review two versions of complex coordinate scaling (standard and exterior scaling) and show how these techniques can be used to compute the resonance states of an open, time-periodic system. Results from the standard and exterior scaling versions are compared, for both time-independent and time-dependent calculations.

5.2.1 Standard complex coordinate scaling (CCS)

We first examine how the eigenvalues and eigenstates of a time-independent open system can be calculated using standard complex coordinate scaling (CCS), a technique that is examined in detail in Refs. [69, 70]. In this chapter we will use a basis of particle-in-a-box states for our calculations. These states are defined by

$$\langle x|n\rangle = \sqrt{\frac{2}{L}} \sin\left(\frac{n\pi x}{L} - \frac{n\pi}{2}\right), \quad (5.4)$$

where $-L/2 \leq x \leq L/2$. Calculations using CCS are performed just as they are in traditional quantum mechanics, except that the coordinate is scaled in the Hamiltonian so that $x \rightarrow xe^{i\theta}$ ($0 \leq \theta < \pi/4$). Scaling the coordinate in this fashion allows us to represent resonance states, which are not in the Hilbert space, using square

integrable eigenfunctions. As a result of this scaling the new time-independent Hamiltonian is

$$\tilde{H}_0 = H_0(xe^{i\theta}) = \frac{p^2 e^{-2i\theta}}{2} - V_0 \exp\left(-(xe^{i\theta}/a)^2\right). \quad (5.5)$$

The kinetic energy operator is easily evaluated using the basis states in Eq. 5.4. As long as our box is sufficiently large ($L \gg 2a/\sqrt{\cos(2\theta)}$) we find that

$$\langle m | -V_0 \exp\left(-(xe^{i\theta}/a)^2\right) | n \rangle = V(m+n) - V(|m-n|) \quad (5.6)$$

where

$$V(j) = \frac{V_0 a \sqrt{\pi} e^{-i\theta}}{L} \exp\left(-\frac{j^2 \pi^2 a^2 e^{-2i\theta}}{4L^2}\right) \cos\left(\frac{j\pi}{2}\right). \quad (5.7)$$

Once these matrix elements are calculated the \tilde{H}_0 matrix can be constructed. Diagonalizing \tilde{H}_0 yields the energy eigenvalues of the time-independent system as well as the eigenvectors

$$|\psi_i\rangle = \sum_{n=1}^N c_{ni} |n\rangle. \quad (5.8)$$

Fig. 5.5a shows the energy eigenvalues of H_0 calculated without complex scaling ($\theta = 0$). The potential supports three bound states at $E = -0.4451, -0.1400$, and -0.00014 a.u. Without complex scaling all eigenvalues lie on the real axis. When the coordinate is scaled, though, the Hamiltonian becomes non-Hermitian and it is possible for eigenstates of the scaled system to have complex eigenvalues. This can be seen in Fig. 5.5b, which shows the eigenvalues calculated using CCS with $\theta = 0.3$. The bound state eigenvalues remain on the real axis but the positive-energy

continuum states are rotated into the lower half plane by an angle of 2θ . It is this rotation of the continuum that will allow us to identify resonances. No resonances exist for the system with Hamiltonian \tilde{H}_0 , only bound states and a continuum.

5.2.2 Exterior complex coordinate scaling

The basic idea of exterior complex coordinate scaling (ECCS) is to scale the x coordinate by a factor $e^{i\theta}$ as in CCS, but only in the region $|x| \geq x_s$ where the potential is zero. Discontinuities at $\pm x_s$ are avoided by using a smooth scaling relation $x \rightarrow F(x)$, where

$$F(x) = x + (e^{i\theta} - 1) \left[x + \frac{1}{2\lambda} \ln \left(\frac{\cosh(\lambda(x - x_s))}{\cosh(\lambda(x + x_s))} \right) \right] \quad (5.9)$$

with $\lambda = 5$ a.u. and $x_s = 25$ a.u. This exterior scaling method is given a thorough presentation in [70, 71]. Because the potential is zero in the region where the coordinate is scaled, the potential matrix elements can be calculated without any complex scaling (i.e. using Eq. 5.6 and 5.7, but with $\theta = 0$). The scaled time-independent Hamiltonian then becomes $\tilde{H}_0 = H_0 + V_{CAP}$, where

$$V_{CAP}(x) = V_0(x) + V_1(x) \frac{\partial}{\partial x} + V_2(x) \frac{\partial^2}{\partial x^2} \quad (5.10)$$

acts as a complex absorbing potential. The coordinate-dependent factors in Eq. 5.10 are defined by

$$V_0(x) = \frac{1}{4} f^{-3}(x) \frac{\partial^2 f}{\partial x^2} - \frac{5}{8} f^{-4}(x) \left(\frac{\partial f}{\partial x} \right)^2, \quad (5.11)$$

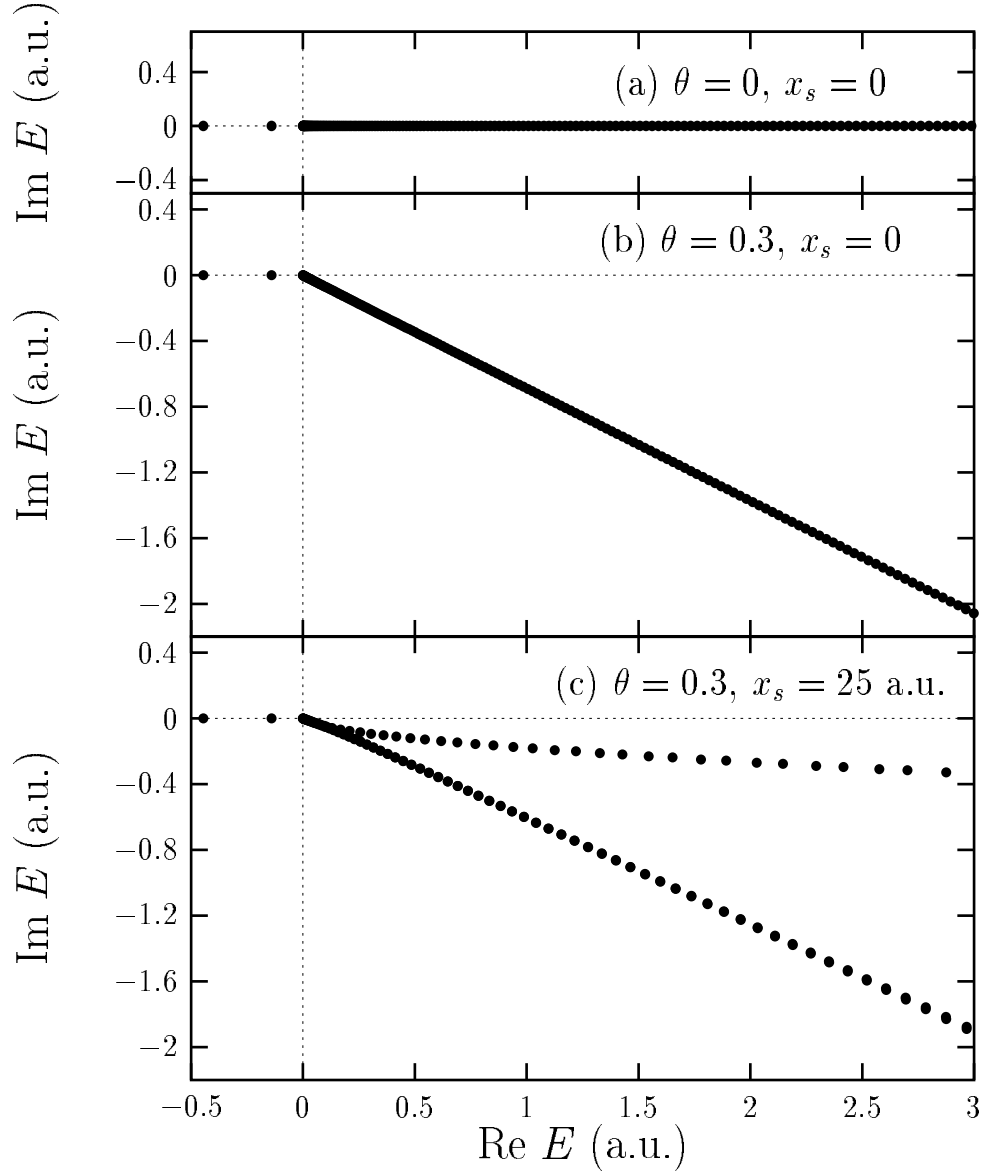


Figure 5.5: The complex-scaled energies of the undriven inverted Gaussian system. The unscaled energies are shown in (a), the CCS energies in (b), and the ECCS energies in (c). The bound states of the system have energies -0.4451, -0.1400, and -0.0001 a.u. All calculations were performed using a box size $L = 200$ a.u. and 400 basis states.

$$V_1(x) = f^{-3}(x) \frac{\partial f}{\partial x}, \quad (5.12)$$

and

$$V_2(x) = \frac{1}{2}(1 - f^{-2}(x)), \quad (5.13)$$

where $f(x) = \partial F / \partial x$. Plots of $F(x)$, $V_0(x)$, $V_1(x)$, and $V_2(x)$ are shown in Figures 5.6, 5.7, 5.8, and 5.9.

We will again use a basis of particle-in-a-box states to calculate \tilde{H}_0 . Matrix elements for the potential energy term are calculated without any complex scaling, while the kinetic energy and V_{CAP} matrix elements are calculated numerically. Diagonalizing \tilde{H}_0 gives the complex energy eigenvalues for the exterior scaled system, which are shown in Fig. 5.5c. Note that the bound state eigenvalues are still on the real axis and most of the continuum states have been rotated into the lower half plane by 2θ . However, several of the positive energy states have been rotated into the lower half plane by considerably less than 2θ . We refer to these as “partially scaled” continuum states. Figure 5.10 shows the wavefunction of one fully scaled continuum state and one partially scaled continuum state. The partially scaled state is strongly peaked near $x = x_s$ and it is non-zero only within the region $-x_s \leq x \leq x_s$, while the fully scaled state is zero within this region. As x_s is decreased toward 0, the number of partially scaled states decreases. At $x_s = 0$ the ECCS eigenvalues exactly match the CCS eigenvalues as expected.

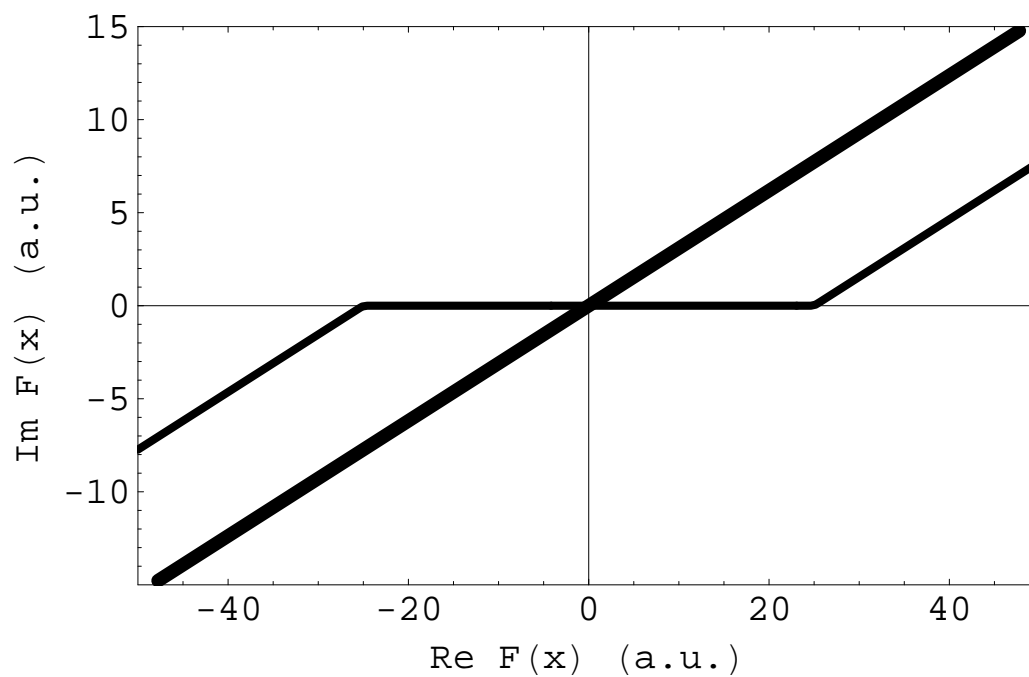


Figure 5.6: The scaled x coordinate, $F(x)$, for standard and exterior complex scaling. The thick line shows the scaled coordinate for CCS with $\theta = 0.3$. The thinner line shows the ECCS coordinate with $\theta = 0.3$ and $x_0 = 25$ a.u.

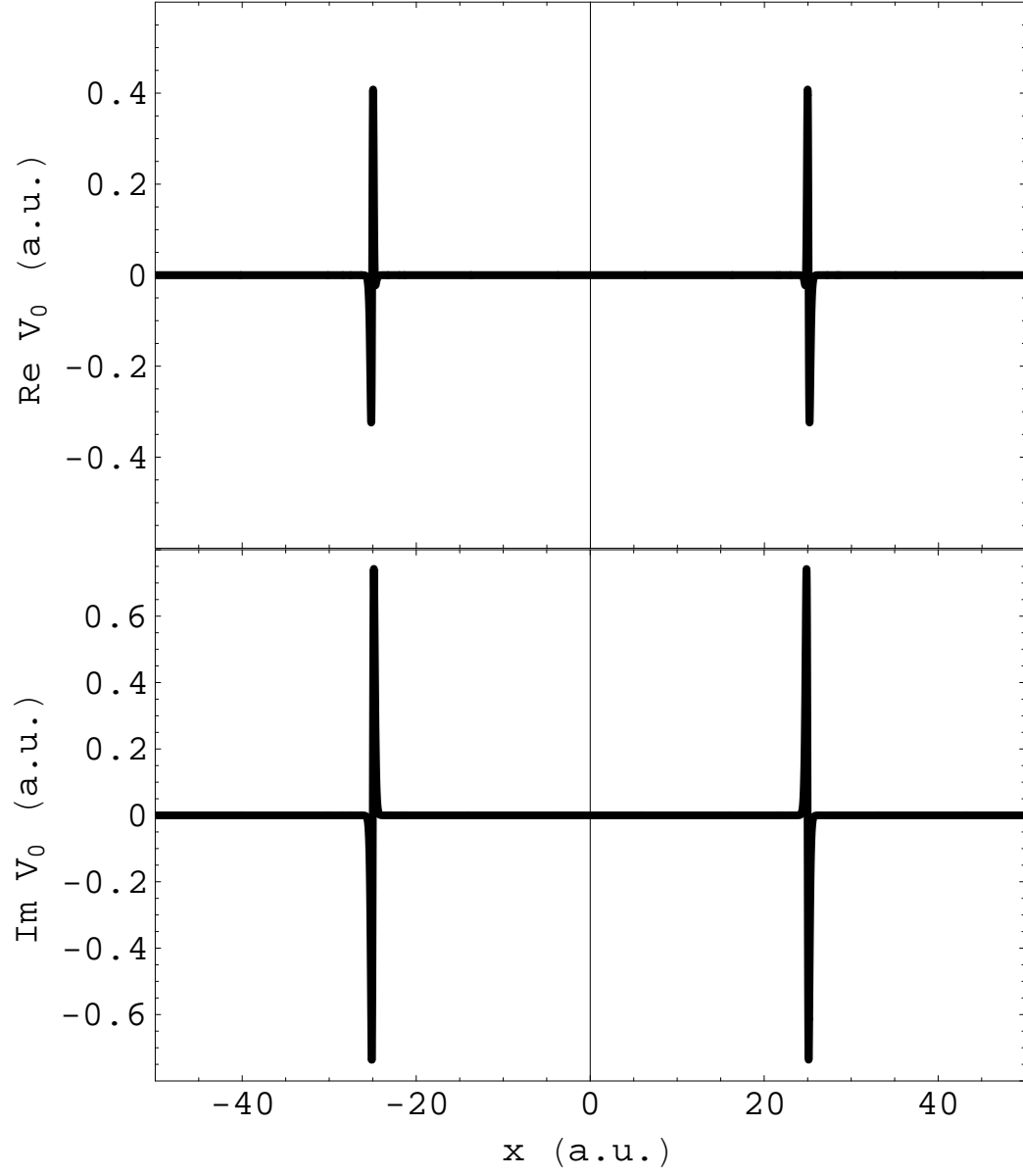


Figure 5.7: The complex local potential $V_0(x)$ which is included in \hat{V}_{CAP} to preserve the volume element. The potential is shown for $\theta = 0.3$ and $x_0 = 25$ a.u.

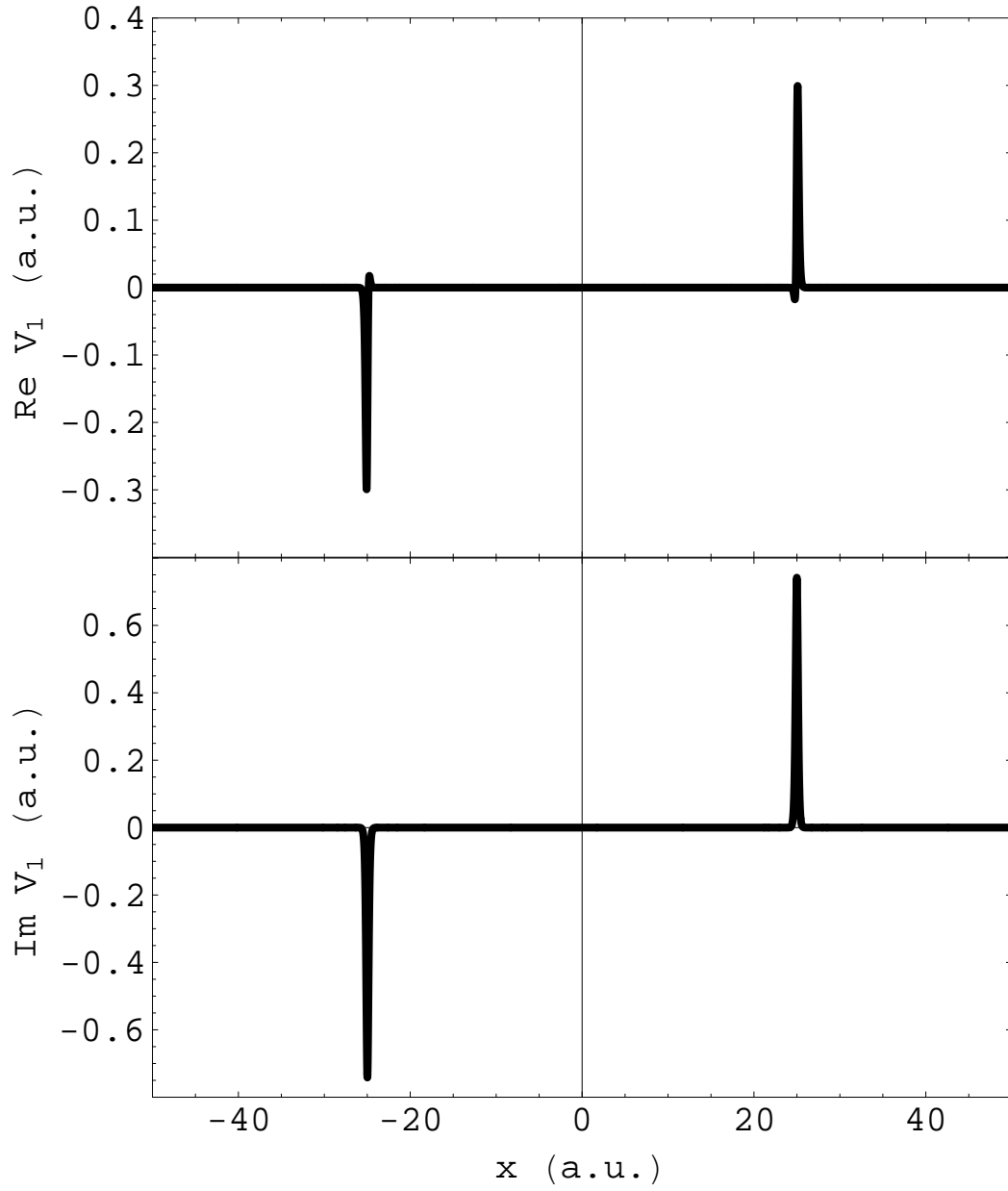


Figure 5.8: The complex local potential $V_1(x)$ which is the coordinate-dependent factor multiplying $\partial/\partial x$ in \hat{V}_{CAP} . The potential is shown for $\theta = 0.3$ and $x_0 = 25$ a.u.

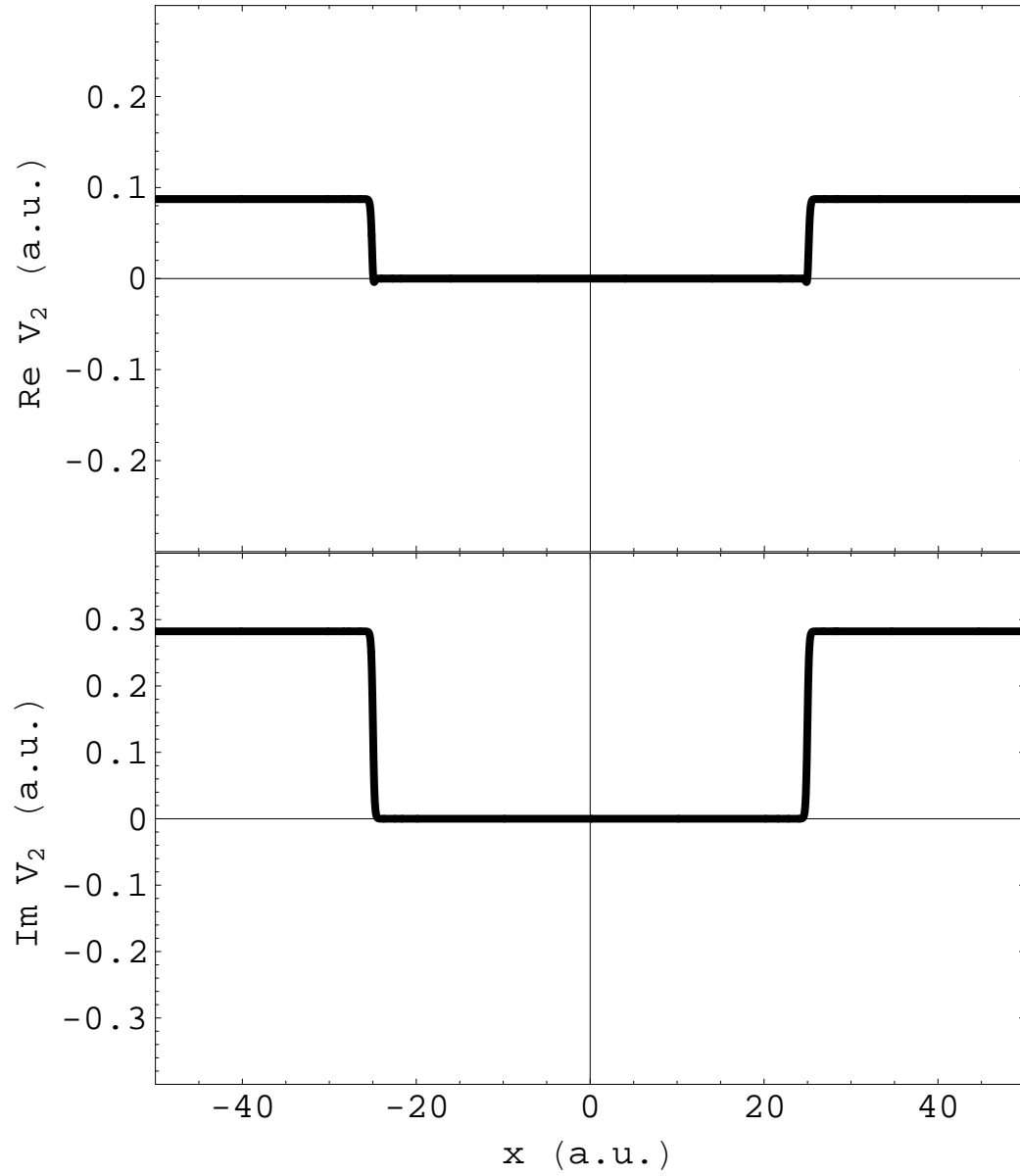


Figure 5.9: The complex potential $V_2(x)$ which is the coordinate-dependent factor multiplying $\partial^2/\partial x^2$ in \hat{V}_{CAP} . This potential vanishes in the interaction region, where the physical potential is non-zero. The potential is shown for $\theta = 0.3$ and $x_0 = 25$ a.u.

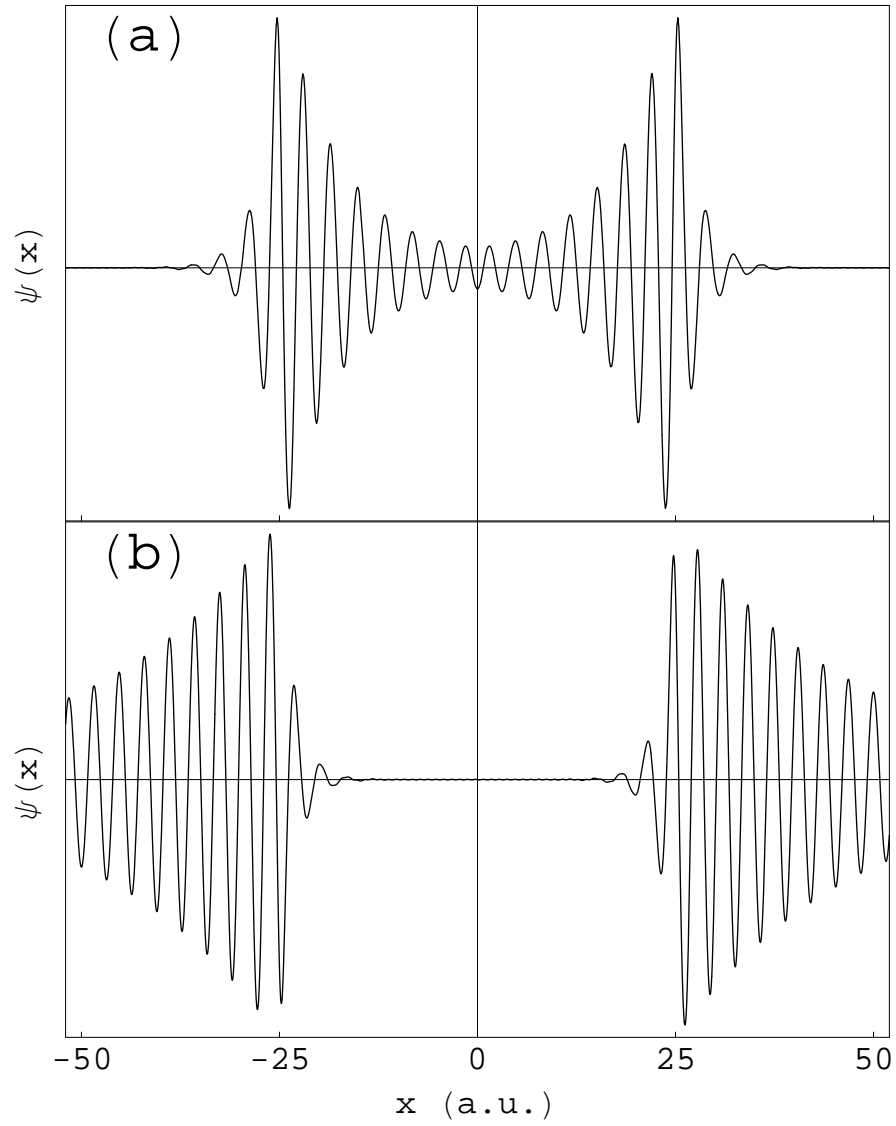


Figure 5.10: Wavefunctions of two ECCS continuum states. The state shown in (a) is a partially-scaled continuum state whose eigenvalue is rotated by less than 2θ from the real axis. The state in (b) is a fully-scaled continuum state whose eigenvalue is rotated the full 2θ from the real axis. The partially-scaled state is localized between $-x_s$ and x_s ($x_s = 25$ a.u.), while the fully-scaled state is almost excluded from this region. Both states are peaked near $\pm x_s$.

5.2.3 Husimi distributions and CCS

Since we will want to examine the structure of the resonance states in the periodically driven system it is important first to examine the structure of the eigenstates of \tilde{H}_0 . We can accomplish this by calculating Husimi distributions (see App. B) for each of the three bound states. In this chapter we construct all Husimi distributions using Gaussian wavepackets with $\sigma = 2$, where σ is defined as in App. B. This gives each wavepacket a width of 1.41 a.u. in x and 0.35 a.u. in p .

Calculating Husimi distributions for complex-scaled states is not completely straightforward. One cannot simply apply Eq. B.1 to the states calculated using CCS because the wavefunctions are not functions of the real spatial coordinate, but rather of the complex-scaled coordinate. Some authors have attempted to rotate the complex-scaled states back into the real coordinate frame in order to calculate the Husimi distribution [72]. While this is a simple procedure to carry out, as it simply involves replacing $\psi(x)$ with $\psi(xe^{i\theta})$ in Eq. B.1, it does not always work because the complex-scaling transformation is not generally reversible. We avoid these problems by calculating Husimi distributions for ECCS states only. In our ECCS calculations the coordinate is only complex-scaled in the region $|x| > 25$ a.u., so for $|x| < 25$ a.u. there is no complex-scaling of the wavefunction. The ECCS method has been shown to produce the correct time-evolution of a wavepacket within the unscaled region, with reflectionless absorption of the wavepacket in the scaled

region [73]. This allows us to calculate the Husimi distribution of an ECCS state using Eq. B.1, provided that we are only interested in the Husimi distribution in the unscaled region. This procedure is similar to that used in Ref. [62], in which the wavefunctions are calculated on a large grid of points in x and repeatedly projected onto a smaller grid as the wavefunction evolves. As in our method, the Repetitive Projection Method induces non-unitary time-evolution only on the parts of the wavefunction that are outside some small range of x and the Husimi distributions within that small range can be computed normally.

Husimi distributions for the three ECCS bound states of \tilde{H}_0 are shown in Figure 5.11. The Husimi distributions shown in Figs. 5.11a and 5.11b match those that are found without complex scaling the Hamiltonian and hence they are the correct distributions. The distribution shown in Fig. 5.11c shows some very slight asymmetry near $x = \pm 25$ a.u. This is an effect of the complex-scaling and it is not seen in the unscaled bound states. Except for this small deviation the distribution shown in Fig. 5.11c is indistinguishable from the Husimi distribution of the unscaled bound state.

5.2.4 Floquet calculations

As we have seen, complex coordinate scaling can be used to calculate the first N energy eigenstates of \tilde{H}_0 . These eigenstates can then be used as a basis to compute

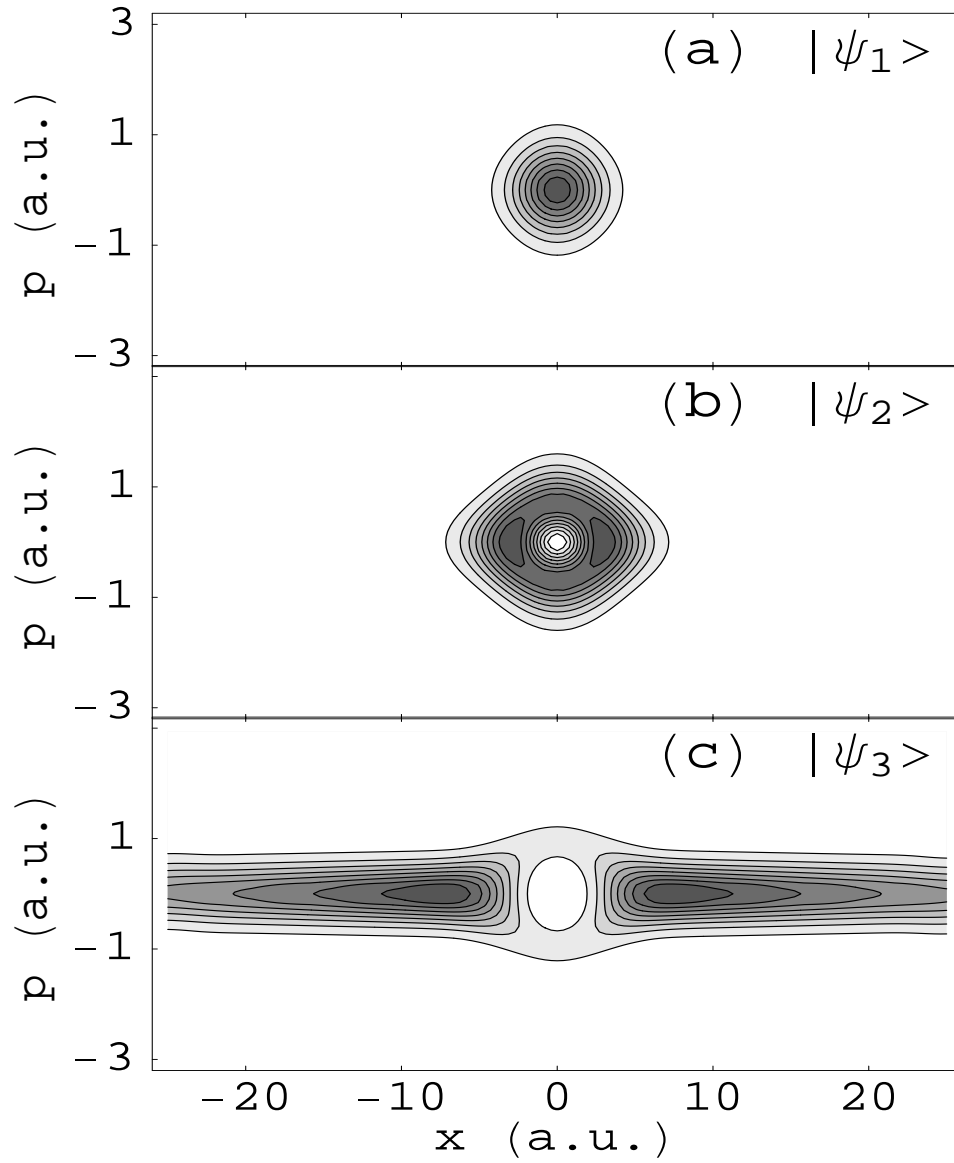


Figure 5.11: Husimi distributions of the bound states of the inverted Gaussian system. The bound state wavefunctions were calculated using ECCS with $x_s = 25$ a.u. The scaling angle is $\theta = 0.3$ for all plots. These distributions match those calculated without complex scaling, except for the very slight asymmetry at the far left and right of (c).

the one-period time evolution (Floquet) matrix, $\hat{U}(T)$, for the driven system (see App. A). This matrix is calculated by numerically integrating the time-dependent Schrödinger equation N times from $t = 0$ to $t = T = 2\pi/\omega$ with initial conditions $|\Psi(t = 0)\rangle = |\psi_i\rangle$, where $|\psi_i\rangle$ is the i th energy eigenstate of \tilde{H}_0 . Diagonalization of this matrix gives the Floquet eigenvalues and eigenstates (in the basis of eigenstates of \tilde{H}_0).

The time-dependent Schrödinger equation for the driven inverted Gaussian system is

$$i\hbar \frac{\partial}{\partial t} |\Psi\rangle = \tilde{H}_0 |\Psi\rangle - \frac{\epsilon}{\omega} \tilde{p} \sin(\omega t) |\Psi\rangle + \frac{\epsilon^2}{2\omega^2} \sin^2(\omega t) |\Psi\rangle \quad (5.14)$$

where \tilde{p} is the complex scaled momentum operator. Since all computations are performed in a basis of eigenstates of \tilde{H}_0 we must first calculate the matrix elements of \tilde{p} . In calculating these matrix elements it is critical to recognize that \tilde{H}_0 is not a Hermitian matrix and thus its eigenvectors do not have the usual properties that eigenvectors of Hermitian matrices have. One cannot obtain the left eigenvectors of a non-Hermitian matrix simply by taking the complex conjugate of the right eigenvectors. In our case, \tilde{H}_0 is complex symmetric and the coefficients of the left eigenvectors are equal to (*not* complex conjugates of) the coefficients of the right eigenvectors, so

$$\langle \psi_i | = \sum_{n=1}^N c_{ni} \langle n |. \quad (5.15)$$

The normalization of the eigenvectors is also different. For our complex symmetric

matrix the eigenvectors should be normalized so that the sum of the squares of the c_{ni} 's is 1, rather than the sum of the absolute squares. With this in mind we can calculate the matrix elements for \tilde{p} using

$$\langle \psi_i | \tilde{p} | \psi_j \rangle = \sum_{m=1}^N \sum_{n=1}^N c_{mi} c_{nj} \langle m | \tilde{p} | n \rangle. \quad (5.16)$$

The $\langle m | \tilde{p} | n \rangle$ are easy to calculate when CCS is used and \tilde{p} is simply $pe^{-i\theta}$. However, when ECCS is used those matrix elements are calculated numerically using

$$\langle m | \tilde{p} | n \rangle = \frac{-i\hbar\pi n}{L^2} [P(m+n) + P(m-n)] \quad (5.17)$$

where

$$P(k) = \int_{-L/2}^{L/2} \sin\left(\frac{k\pi x}{L} - \frac{k\pi}{2}\right) f^{-1}(x) dx \quad (5.18)$$

and $f(x)$ is defined in Sec. 5.2.2.

Since the Floquet eigenstates are calculated in a basis of eigenstates of \tilde{H}_0 we can write them as

$$|q_\beta\rangle = \sum_{i=1}^N d_{i\beta} |\psi_i\rangle. \quad (5.19)$$

Because they are eigenstates of the one-period time evolution operator (Floquet matrix) we can write

$$\hat{U}(T)|q_\beta\rangle = e^{-iq_\beta T}|q_\beta\rangle \quad (5.20)$$

where q_β is the quasienergy of the state $|q_\beta\rangle$. Because the Hamiltonian \tilde{H}_0 is not Hermitian, the time evolution operator is not unitary. This means that the Floquet

eigenvalues do not necessarily have unit modulus, and thus the quasienergies q_β are in general complex. We can write the quasienergies as $q_\beta = \Omega_\beta + i\Gamma_\beta/2$, where $\tau_\beta = 1/\Gamma_\beta$ is the lifetime of the state $|q_\beta\rangle$. Resonance states are easily identified by plotting the Floquet eigenvalues, which we will denote as $\lambda_\beta = \exp(-iq_\beta T)$. Fig. 5.12 shows the Floquet eigenvalues calculated using both CCS and ECCS for the driven Gaussian system with $\omega = 0.0925$ a.u. and $\epsilon = 0.038$ a.u. The continuum eigenvalues that were found with the CCS method form a well-defined spiral from the origin out to the edge of the unit circle. These states are indicated by filled circles in Fig. 5.12a. Resonance states are indicated by filled squares and lie off of the continuum spiral. The continuum spiral is not as well-defined when the ECCS method is used, as shown in Fig. 5.12b. However, only a few eigenvalues near the origin appear to fall out of the spiral. This could cause some difficulty in identifying broad (short-lived) resonances, but narrow (long-lived) resonances can still be easily identified. Fig. 5.12 shows that CCS and ECCS appear to give the same resonance eigenvalues.

The resonance eigenvalues should be independent of the scaling angle θ , while the continuum eigenvalues rotate around the origin as θ is changed. However, when calculations are performed using a finite basis the resonance eigenvalues will be weakly dependent upon θ [74]. To accurately determine the quasienergies (and hence the lifetimes) of these states it is important to optimize θ by finding the stationary

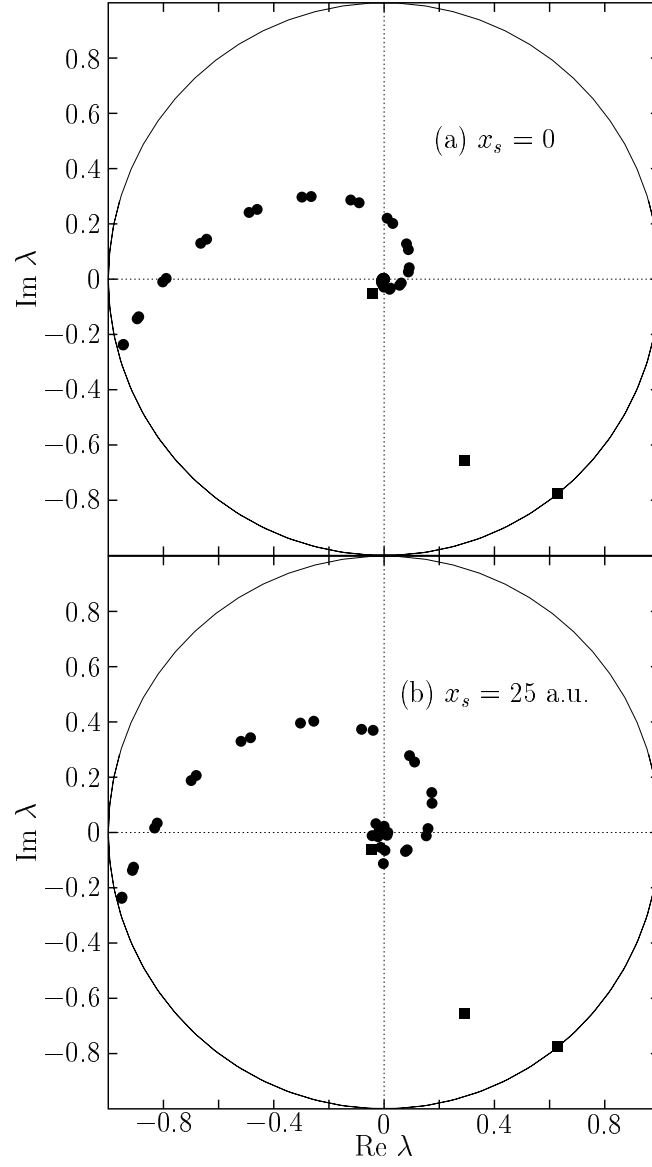


Figure 5.12: Floquet eigenvalues for the driven inverted Gaussian system with $\omega = 0.0925$ a.u. and $\epsilon = 0.038$ a.u. The eigenvalues calculated using CCS are shown in (a). In (b) the ECCS eigenvalues are shown. The scaling angle is $\theta = 0.3$ for both sets of eigenvalues. Resonance states are indicated by filled squares, while continuum states are indicated by filled circles.

point of each resonance eigenvalue as θ is changed. However, since our goal is not an accurate quantitative determination of eigenvalues or lifetimes but a qualitative understanding of the relationship between the quantum dynamics and the classical motion, it is not critical that θ be optimized for our calculations. Optimizing θ presents a problem in this type of study because the optimal value of θ is generally different for different resonance states. We wish to study all of the resonance states of the system and it is impossible to optimize θ for all resonance states within a single calculation of the Floquet matrix. We find that changing θ between 0.3 and 0.7 results in no visible change in the plots of the resonance eigenvalues. There is also no visible change in the Husimi distributions of the states. Not optimizing θ may lead to slight inaccuracies in the calculated lifetimes for the resonance states, but we find that the error in the lifetimes is no greater than $\pm 0.1T$ which is acceptable for our purpose here.

In Figure 5.13 we show the Husimi distributions of the three ECCS resonance states indicated in Fig. 5.12b. Lifetimes of the three states are indicated in units of the driving period $T = 2\pi/\omega$. Filled circles indicate the locations of the classical periodic orbits. The resonance state with the longest lifetime is almost indistinguishable from the ground state of the undriven system shown in Fig. 5.11a. The state shown in Fig. 5.13b has a much shorter lifetime and is beginning to elongate toward the positions of the unstable periodic orbits, with a peak of probability near

the periodic orbit at $(x = 6.98 \text{ a.u.}, p = 0)$. At this field strength the periodic orbits are separated by approximately 3.3 a.u., which is only two times the width of the wavepackets used in calculating the Husimi distribution. This makes it difficult to tell whether or not the Husimi distribution has separate peaks on each periodic orbit. The state shown in Fig. 5.13c has a very short lifetime and its Husimi distribution is similar to that of a continuum state.

5.3 Resonance creation and scarring

Figure 5.14 shows the Floquet eigenvalues for $\epsilon = 0.065$ and 0.09 a.u. Again, resonance states are indicated by filled squares while continuum states are indicated by filled circles. We see that the number of resonance states increases as ϵ is increased, from only three at $\epsilon = 0.038 \text{ a.u.}$ (see Fig. 5.12) to five at $\epsilon = 0.09 \text{ a.u.}$ This is in agreement with BMK [67]. In the classical system, however, the stable structure near $(x = 0, p = 0)$ gets smaller as ϵ is increased. If the resonance states were associated with this stable classical structure then some of the resonances should disappear as ϵ is increased. Instead, the opposite behavior is found. To find the explanation for the increase in the number of resonance states we examine the Husimi distributions of the resonance states indicated in Fig. 5.14.

Figure 5.15 shows HDs for the four resonance states at $\epsilon = 0.065 \text{ a.u.}$ Lifetimes for the states are indicated in units of the driving period and the positions of the

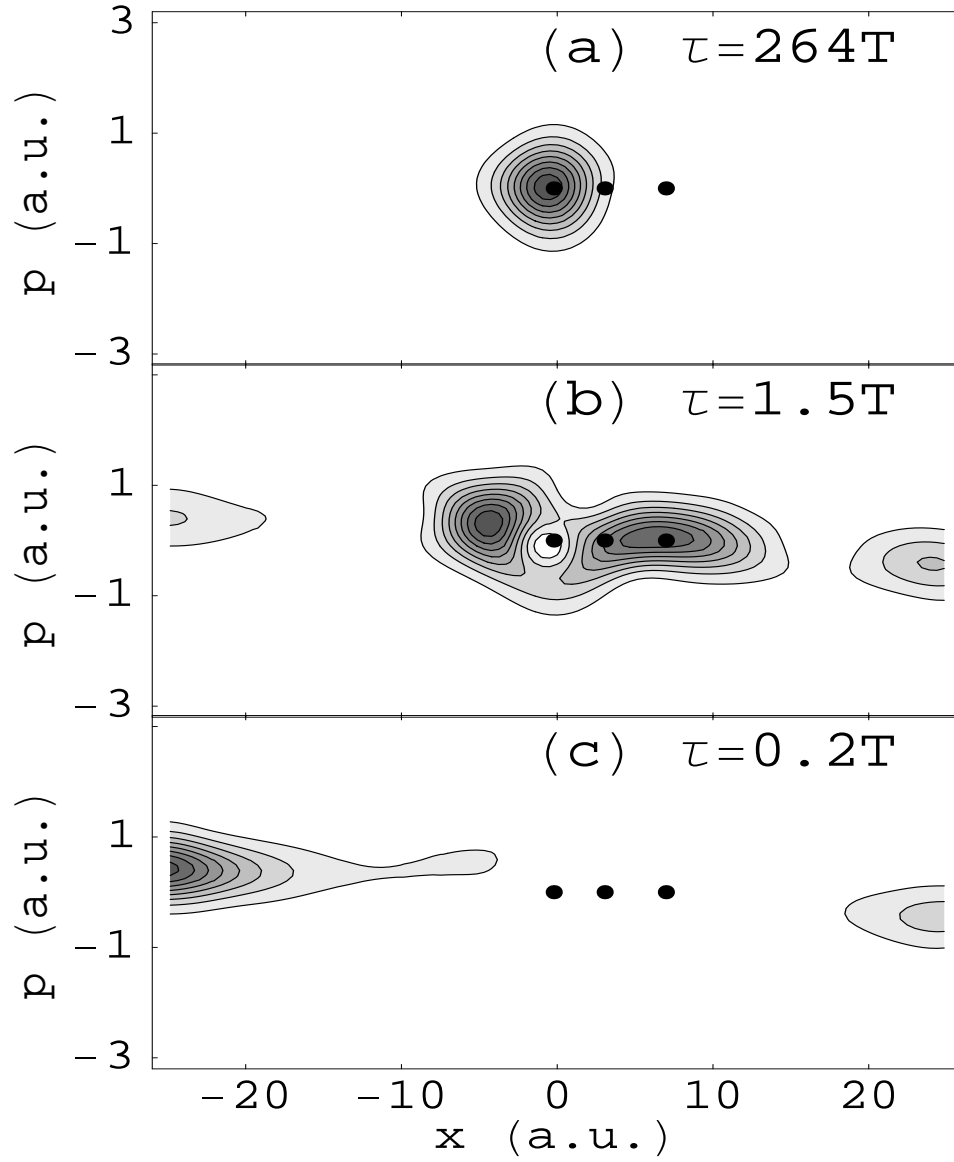


Figure 5.13: Husimi distributions of the resonance states at $\epsilon = 0.038$ a.u. The resonance wavefunctions were calculated using ECCS with $x_s = 25$ a.u. The locations of periodic orbits are indicated by filled circles. The scaling angle is $\theta = 0.3$ for all plots. The lifetimes for each state are given in units of the driving period $T = 2\pi/\omega$.

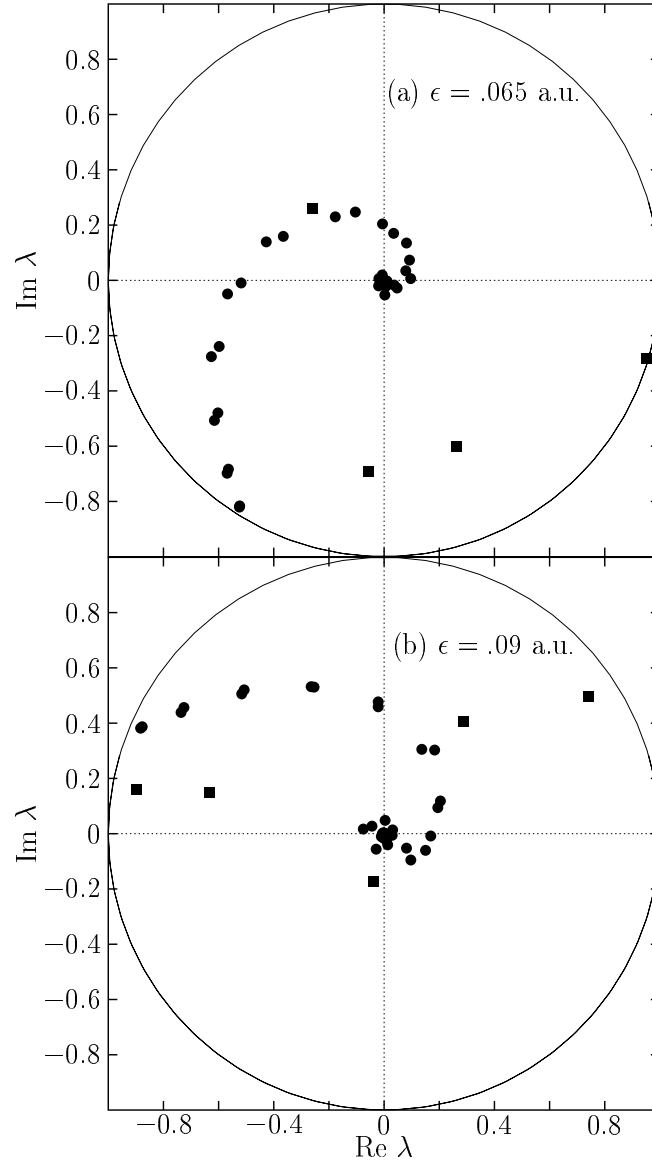


Figure 5.14: Floquet eigenvalues for $\omega = 0.0925$ a.u. and two different field strengths. The eigenvalues are calculated using ECCS with $\theta = 0.3$ and $x_s = 25$ a.u. Resonance states are indicated by filled squares and continuum states by filled circles. At these higher field strengths the number of resonance states is greater than at $\epsilon = .038$ a.u.

periodic orbits are indicated by filled circles. At this field strength the separation between the periodic orbits is about five times the width of the wavepackets used to compute the Husimi distribution. The state with the longest lifetime looks very much like the ground state of the undriven system. The states shown in Figs. 5.15b and 5.15c show some similarities to the excited states of the undriven system, but they have both been elongated in the direction of the unstable periodic orbits. The state shown in Fig. 5.15b has a probability peak near the unstable periodic orbit at $(x = 16.67 \text{ a.u.}, p = 0)$, while the state shown in Fig. 5.15c has a peak between the two unstable orbits. These two states appear to have become at least partially associated with the unstable periodic orbits. The state shown in Figure 5.15d is the newly created resonance and it has the shortest lifetime of the four. It has a modest peak near the periodic orbit at $(x = 9.09 \text{ a.u.}, p = 0)$.

Figure 5.16 shows HDs for four of the five resonance states at $\epsilon = 0.09 \text{ a.u.}$. At this field strength the separation of the periodic orbits is approximately eight times the width of the wavepackets used for the Husimi distribution. The state that closely resembles the undriven ground state (Fig. 5.16b) no longer has the longest lifetime. Instead, the longest-lived state resembles the first excited bound state of H_0 , but with additional peaks near the periodic orbits at $x = 11.52 \text{ a.u.}$ and $x = 22.04 \text{ a.u.}$ The state shown in Fig. 5.16d is similar to the state shown in Fig. 5.15d, but with a more prominent peak near the periodic orbit at $x = 11.52$

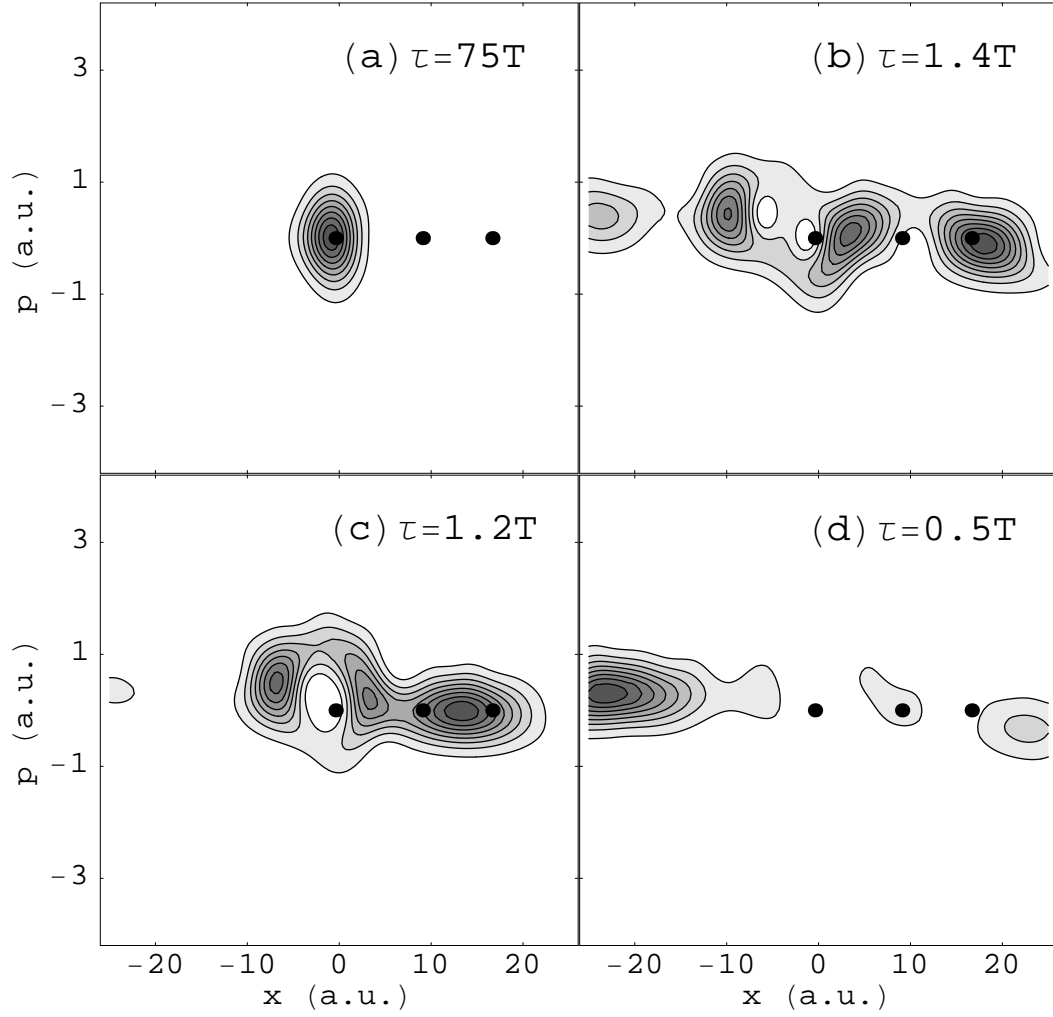


Figure 5.15: Husimi distributions for the four resonance states at $\epsilon = 0.065$ a.u. Lifetimes for each state are given in units of the driving period $T = 2\pi/\omega$. The locations of the periodic orbits are indicated by filled circles.

a.u. Note that the lifetime of this state is also greater than that of the state shown in Fig. 5.15d.

At low values of ϵ all of the resonances have their probability concentrated near $(x = 0, p = 0)$. At these low values of ϵ the two unstable periodic orbits are located close to the stable orbit near $(x = 0, p = 0)$. If any resonance state was associated with the unstable periodic orbits at such low field strengths it would be difficult to tell from its Husimi distribution. As ϵ is increased the unstable periodic orbits move toward larger values of x and some of the resonance states begin to spread in that direction as well. At moderate values of ϵ some states show peaks near the periodic orbit that is farthest from $(x = 0, p = 0)$, close to $x = 2\alpha$. Only at high values of ϵ do we begin to see a state that is peaked on the unstable orbit that is closest to $(x = 0, p = 0)$, near $x = \alpha$. We believe that it is the association between the resonances and the unstable periodic orbits that explains the creation of resonance states as ϵ is increased. At low ϵ all three periodic orbits are too close together to support many quantum states because they all occupy essentially the same region of phase space. As ϵ is increased the unstable periodic orbits move away from the stable one and from each other. This allows quantum states to be associated with these unstable orbits without occupying the same region of phase space as the states associated with the stable orbit, so new resonance states are created. It is the scarring of resonance states on unstable periodic orbits of the classical system

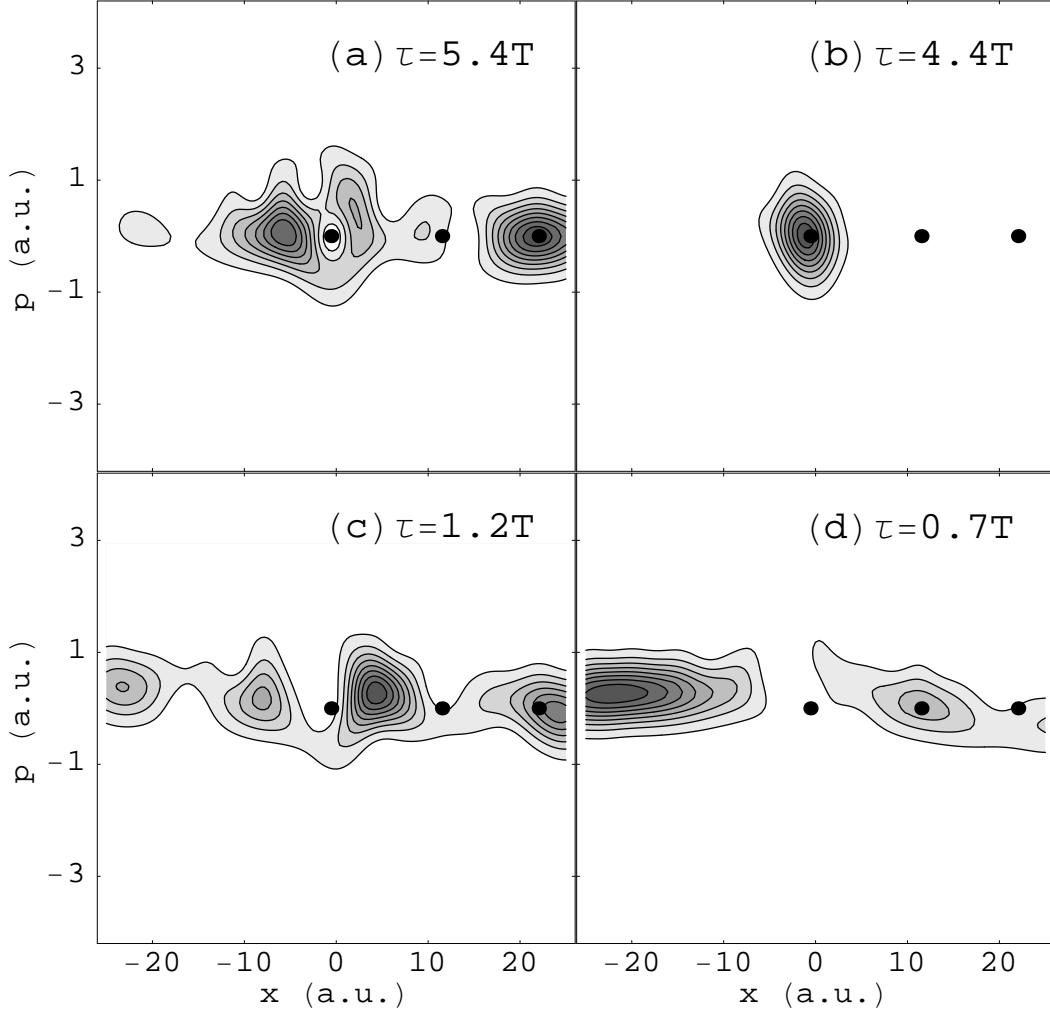


Figure 5.16: Husimi distributions for the four of the five resonance states at $\epsilon = 0.09$ a.u. The resonance state with the shortest lifetime is not shown because its Husimi distribution is indistinguishable from that of a continuum state. Lifetimes for each state are given in units of the driving period $T = 2\pi/\omega$. The locations of the periodic orbits are indicated by filled circles.

that accounts for the increase in the number of resonance eigenstates, even as the stable region in the classical phase space is diminished.

The behavior we see here would be unlikely to stabilize the ground state of the undriven system against ionization in a high intensity field. This is because the lifetime of the resonance state that seems most closely related to the ground state (shown in Figs. 5.13a, 5.15a, and 5.16b) decreases as ϵ is increased. However, the observed behavior could lead to stabilization for an excited state of the undriven system. The excited states have most of their probability away from $(x = 0, p = 0)$ and would thus overlap with resonance states that are not peaked at that point. Since these resonances grow in number and increase their lifetimes as ϵ is increased, an excited state of the undriven system may become stabilized against ionization as ϵ is increased.

5.4 Avoided crossings between resonances

Avoided crossings between resonance eigenvalues have been identified in this system [65, 67]. Avoided crossings between Floquet eigenvalues play an important role in multi-photon ionization [75] and the delocalization of Floquet eigenstates [76]. In this section we investigate the quantum dynamics at one avoided crossing to determine if it leads to delocalization of the resonance eigenstates. Delocalization is closely related to ionization in these systems because long-lived resonance states can

only exist if they are localized within the interaction region. If avoided crossings lead to delocalization they would also lead to a decrease in the lifetime, and eventually the destruction, of the resonance states.

Figure 5.17 shows the Floquet eigenvalues of three resonance states at several field strengths between $\epsilon = 0.076$ and 0.085 a.u. Two of these states (labeled A and B in Fig. 5.17 and indicated by filled circles and squares, respectively) are involved in a prominent avoided crossing at a field strength of about $\epsilon = 0.0805$ a.u. The third resonance eigenvalue (labeled C and indicated by filled triangles) passes close by the other two at this field strength, but it is not clear from Fig. 5.17 if that state is involved in the avoided crossing. The avoided crossing between states A and B appears to be an isolated avoided crossing. This type of avoided crossing has been shown to result in nothing more than an exchange of structure between the two eigenstates [76, 58]. However, this effect has only been observed in closed systems. In open systems the eigenvalues are complex and the structural changes of the eigenstates as they pass through an isolated avoided crossing might lead to delocalization of one or both of the states.

To determine the effect of this avoided crossing on the resonance states we examine the Husimi distributions of the states A , B , and C shown in Figure 5.18. As ϵ is increased from 0.078 a.u. to 0.0805 a.u. the states A and B undergo strong mixing with each other. When the field strength is increased to 0.083 a.u. we find

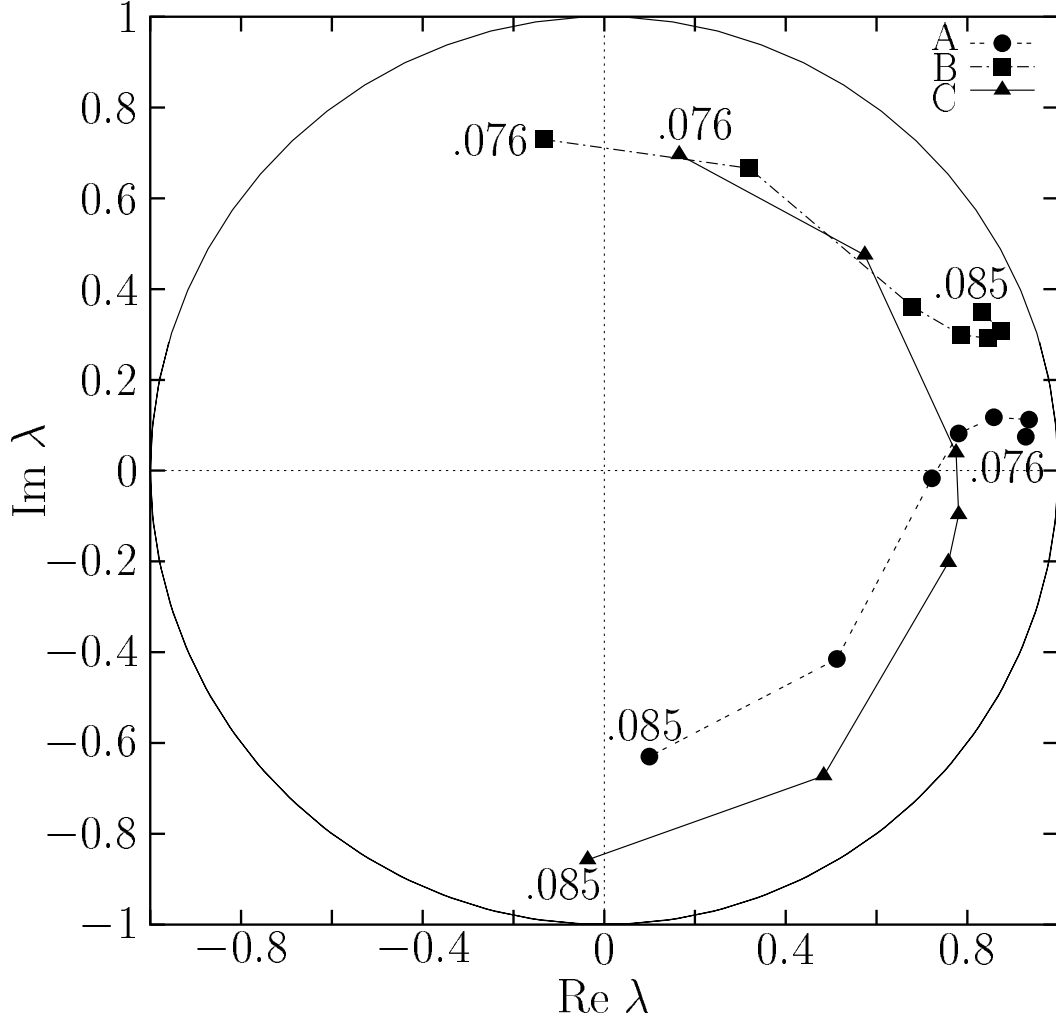


Figure 5.17: Floquet eigenvalues of three resonance states (labeled A , B , and C) that are involved in an avoided crossing around $\epsilon = 0.0805$ a.u. The points show the eigenvalues for $\epsilon = .076, .078, .08, .0805, .081, .083$, and $.085$ a.u. The numbers shown in the plot indicate the field strengths at the end points of each eigenvalue sequence. The lines are intended only as an aid to the eye.

that states A and B have completely exchanged their structure. State C does not appear to have any significant structural changes in this range of field strengths. However, it should be noted that state C has a significant increase in its lifetime as ϵ is increased from 0.078 a.u. to 0.083 a.u. States A and B exchange lifetimes as well as structure, but the lifetimes of both states at $\epsilon = 0.083$ a.u. are somewhat smaller than the corresponding lifetimes at $\epsilon = 0.078$ a.u. It may be that state C somehow gains stability at the expense of states A and B , even though it does not appear to pick up any of the structure of those states. Note that there are slight differences between the Husimi distributions of states A and B at $\epsilon = 0.073$ a.u. and the corresponding distributions at $\epsilon = 0.083$ a.u., but these may be due to a small amount of mixing with state C or with continuum states.

Figure 5.18 does not reveal any significant increase in the delocalization of any of the resonance states. In fact, the structural changes of the Floquet states as they pass through the avoided crossing are identical to those seen in closed systems [76, 58]. This is not surprising, because in this avoided crossing it is the real parts of the eigenvalues (determined by the angular position of the point in Fig. 5.18) that avoid crossing, while the imaginary parts (determined by the distance of the point from the origin in Fig. 5.18) actually cross. This is an indication that the coupling between states A and B is stronger than the coupling of those states to the continuum [75, 77]. Thus, the continuum plays no major role in the avoided crossing

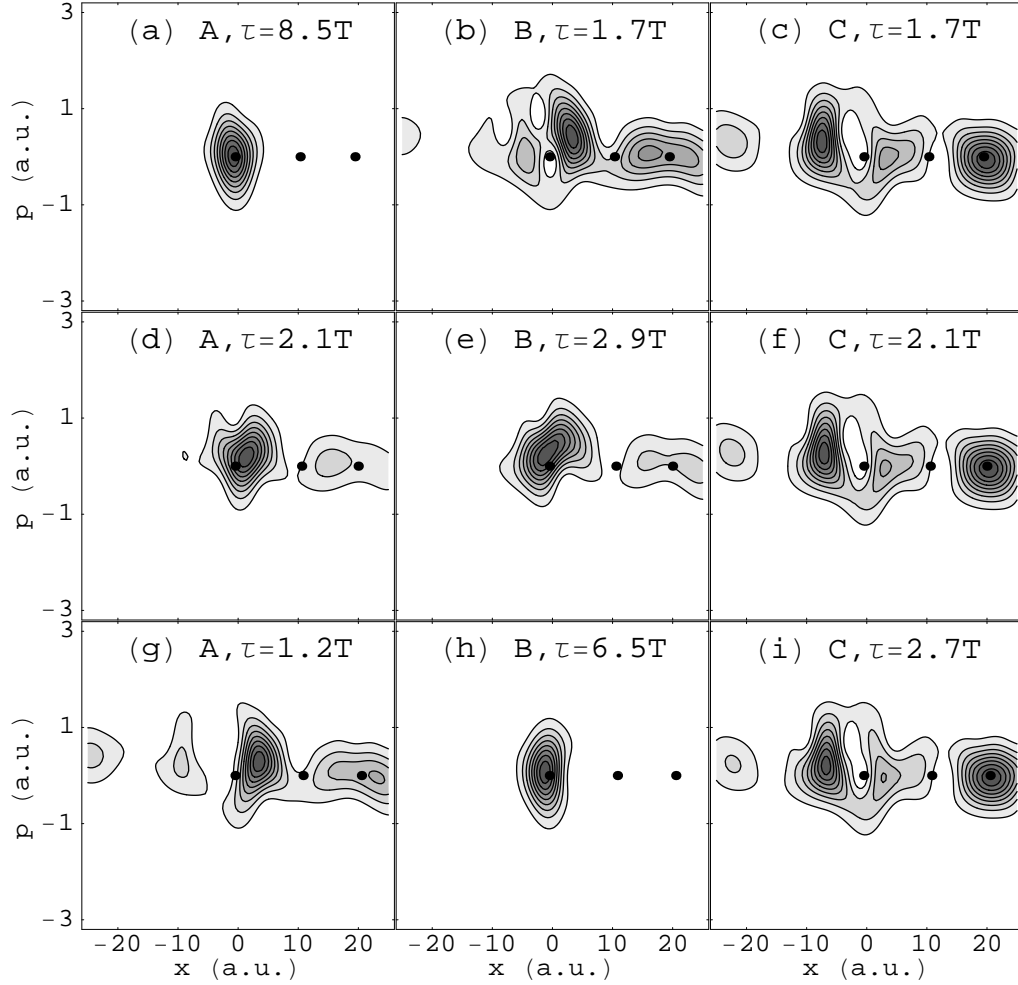


Figure 5.18: Husimi distributions for the states involved in the avoided crossings shown in Fig. 5.17. The labels A , B , and C correspond to the labels in Fig. 5.17. Lifetimes for each state are given in units of the driving period $T = 2\pi/\omega$. The top row (a-c) shows Husimi distributions for the three resonance states at $\epsilon = .078$ a.u. The second row (d-f) shows the distributions at $\epsilon = .0805$ a.u. The bottom row (g-i) shows the distributions at $\epsilon = .083$ a.u. States A and B appear to exchange their structure as they pass through the avoided crossing. State C does not appear to undergo any major changes in its structure, but its lifetime increases dramatically as it passes through the avoided crossing. The locations of the periodic orbits at each field strength are indicated by filled circles.

and one would expect the behavior to be similar to that seen in closed systems. We expect that the delocalization and destruction of resonance states occurs primarily as the result of coupling between a resonance state and the continuum rather than between resonance states [78].

Avoided crossings between resonance states may play an important role in other phenomena in this system. For example, it has been shown in bound systems that avoided crossings between Floquet eigenstates can result in increased high harmonic generation (HHG). Avoided crossings contribute to increased HHG in two ways. During the turn-on of a laser field avoided crossings can put the quantum system into a superposition of Floquet states that may emit radiation at higher frequencies than would be emitted by a single Floquet state [40]. Avoided crossings also contribute to HHG by spreading the Floquet states over a wider range of energy, thus allowing a single Floquet state to emit higher frequency radiation. For the type of avoided crossing observed here the states are only delocalized near the exact field strength at which the avoided crossing occurs, because at this field strength the Floquet states have mixed their structure [76]. At that particular field strength, though, this effect could lead to increased HHG. In fact, increased HHG has been observed in previous studies of the avoided crossings in this system [65].

Chapter 6

Destruction of Quasienergy

Resonance States

In the previous chapter we examined the creation of resonance states as the strength of the driving field was increased in the driven inverted Gaussian system. In this chapter we will study a system where the number of resonance states decreases as the strength of the driving field is increased. An examination of this system by Moiseyev and Korsch [79] revealed two mechanisms that led to the disappearance of a discrete quasienergy eigenvalue from the spectrum of the system. The first mechanism was an avoided crossing between two quasienergy states that pushed one of the eigenvalues into the continuum. The second mechanism was a threshold effect where one of the quasienergy states has an ionization energy that is an integer

multiple of the photon energy, resulting in strong coupling between the state and the continuum and eventually the destruction of the discrete quasienergy state.

In this chapter we examine the phase-space representations of resonance states as they are destroyed by the threshold effect mentioned above. As the field strength is increased the resonance states show a flow of probability out of the interaction region and into the region of phase space occupied by the continuum states. This is an indication of strong coupling to the continuum. We attempt to quantify this coupling and show that it increases dramatically when the resonance state has an ionization energy close to the energy of a photon in the field. In addition, we carry out a close examination of two avoided crossings between a resonance state and the continuum. We find that this particular type of avoided crossing is not solely responsible for the destruction of the resonance state, although it may accelerate the process.

6.1 Time-Dependent Rosen-Morse Model

The model we study is a simple one-dimensional, time-periodic system whose Hamiltonian is given by $H = H_0 + V(t)$, where $H_0 = p^2/2 + V_0(x)$ is the Hamiltonian of the time-independent system and $V(t)$ represents a time-periodic driving field. In this paper we choose for $V_0(x)$ the Rosen-Morse potential, which has been used to model the vibrational states of polyatomic molecules [80]. The Rosen-Morse potential (in

atomic units) is given by:

$$V_0(x) = -\frac{V_0}{\cosh^2(x/x_0)}. \quad (6.1)$$

For $V(t)$ we choose

$$V(t) = -\frac{V_0\epsilon \cos(\omega t)}{\cosh^2(x/x_0)} \quad (6.2)$$

with field strength ϵ and frequency $\omega = 1$ a.u. This is the same model studied by Moiseyev and Korsch [79], but we leave \hbar fixed at 1 a.u. and use $V_0 = 2$ a.u. and $x_0 = 1/\sqrt{3}$ a.u. For these parameters the time-independent potential has only three bound states. We choose these parameter values because the number of resonance states in the system is small, which allows us to easily follow all of the resonance states as ϵ is increased in the system. In addition, other studies have been done on this system for these parameter values [81] and this allows us to directly compare our eigenvalue calculations with published results.

Because the coordinate-dependent factor in the interaction potential has the same form as the time-independent potential, the time-averaged potential supports the same number of bound states as does the potential for $\epsilon = 0$. Moiseyev and Korsch exploited the simplicity of this model to identify the two mechanisms for resonance destruction mentioned above [79]. In this work, though, the number of resonance states is so small that the resonance eigenvalues are unlikely to have an avoided crossing, rendering the avoided crossing mechanism ineffective. This allows us to focus on the threshold effect and gain a clear picture of how this type of

resonance destruction manifests itself in the phase-space structure of the quasienergy eigenstates.

Before we begin exploring the quantum dynamics of this system it is important to discuss the classical motion. Strobe plots of the classical motion are shown in Figure 6.1 for several values of the field strength. Fig. 6.1a shows the bound classical motion for the undriven system and the border of this region is the separatrix between the bound and unbound motion. The interaction region (the region within the separatrix) stretches out to about $x = \pm 7$ a.u. before tapering off. As the field strength is increased the trajectories near the separatrix become chaotic, while the motion near the bottom of the potential well ($x = 0, p = 0$) remains regular. As ϵ is increased further this regular region shrinks and for field strengths greater than $\epsilon \approx 1.2$ a.u. no regular region is visible. The disappearance of the stable island near ($x = 0, p = 0$) as ϵ is increased is the underlying cause of the destruction of the resonances in the quantum system, but the quantum dynamics are not completely determined by this classical picture.

6.2 Resonance Destruction

As in our previous investigations of quantum systems we focus on the eigenstates of the Floquet matrix (see App. A). In order to calculate the Floquet eigenstates of this open quantum system, we employ the technique of complex coordinate scaling

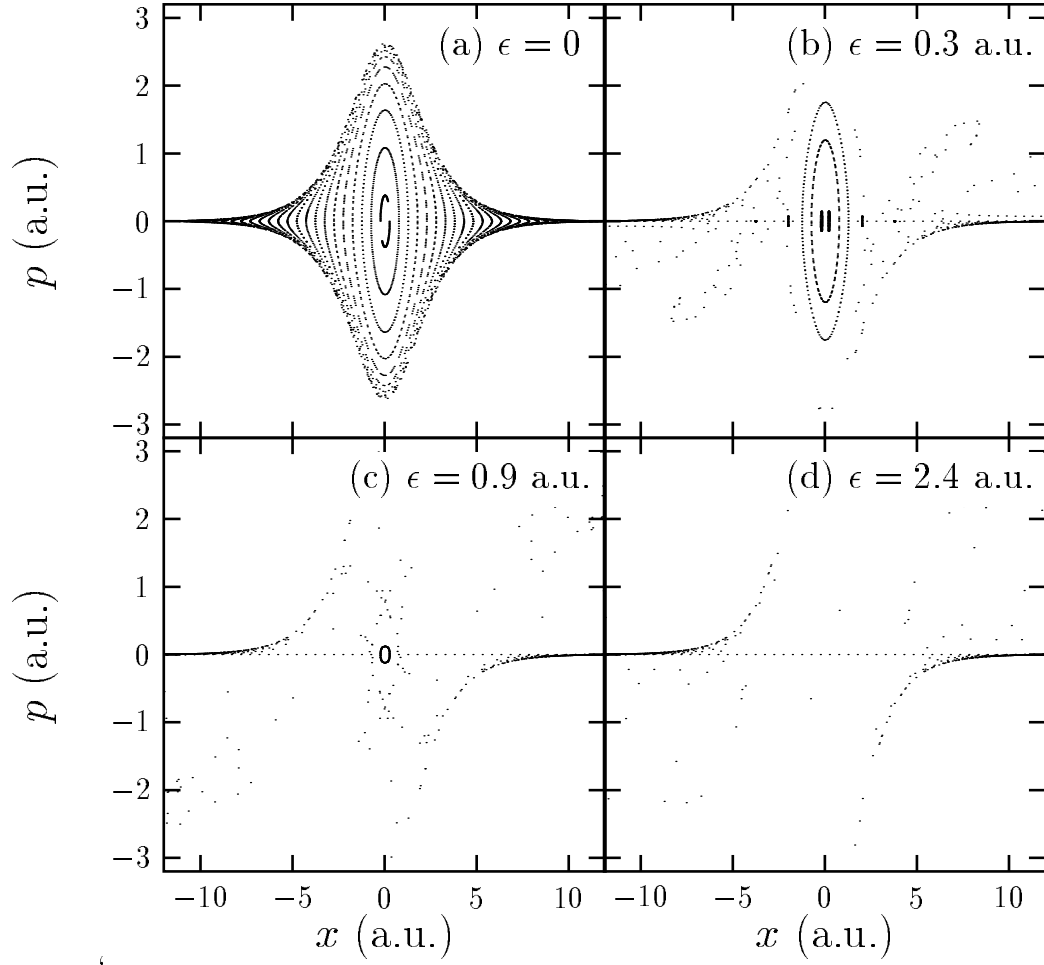


Figure 6.1: Strobe plots of the classical dynamics of the time-periodic Rosen-Morse system at several field strengths. The stable region surrounding $(x = 0, p = 0)$ shrinks as ϵ is increased. For ϵ greater than about 1.2 a.u. there is no detectable stable region.

described in Ch. 5 and in Refs. [69, 71, 70]. As in Ch. 5 we will use both regular complex coordinate scaling (CCS) and exterior scaling (ECCS). We find that the regular scaling over all space is best for calculating eigenvalues, but that the exterior scaling is better for studying the structure of the eigenfunctions.

Our calculation procedure is identical to that used in Ch. 5. All calculations are performed using a particle-in-a-box basis. For the regular scaling calculations we used a box size of $L = 40$ a.u. and 100 basis states. For the exterior scaling calculations we used a larger box with $L = 80$ a.u. and 200 basis states. We first calculate the eigenvalues and eigenstates of the time-independent Hamiltonian H_0 . We find, for our parameter values, that the system has three bound states with energies $-3/2$, $-2/3$, and $-1/6$ a.u., which is in agreement with published results [81]. We then use the eigenstates of H_0 as a basis for our calculation of the Floquet eigenstates of the time-dependent system.

As in Ch. 5 we will use plots of the eigenvalues of the Floquet matrix to identify the metastable resonance states. The eigenvalues of the discretized continuum states form a spiral that runs from the edge of the unit circle to the origin on these plots. As the scaling angle θ is increased this spiral converges more rapidly to the origin. The resonance eigenvalues, on the other hand, are not on the spiral and are independent of the value of θ . In Figure 6.2 we show the Floquet eigenvalues for the system (using CCS) for field strengths ranging from $\epsilon = 0$ to $\epsilon = 2.4$ a.u. The

resonance states are labeled A , B , C , and D . At $\epsilon = 0$, state D is a quasibound state with a very small positive energy while states A , B , and C are bound states. As ϵ is increased the eigenvalues associated with these states move from the edge of the unit circle toward the origin. For very high values of ϵ the eigenvalues are absorbed into the continuum spiral and the resonance states are destroyed. From the figure it appears that states B and C are destroyed at lower field strengths than states A and D . Note that the eigenvalues in the continuum spiral move slightly as ϵ is increased.

Figure 6.2 shows the movement of the eigenvalues for two different values of the scaling angle θ . The reason for this is that for finite basis calculations the resonance eigenvalues are weakly dependent on θ . To insure that the value of θ did not play a significant role in determining the character of the eigenvalue curves we performed all of our calculations using two different values of θ . It is clear from the figure that the general character of the curves does not depend on θ . The only significant differences occur where resonance eigenvalues approach the continuum spiral. This difference occurs because changing the value of θ shifts the position of the spiral. The most dramatic difference occurs where state C encounters the spiral. In Fig. 6.2a, state C appears to undergo an avoided crossing with a continuum state which is then kicked out of the continuum spiral as state C is absorbed into it. This state in turn has an avoided crossing with another state which is kicked out of the

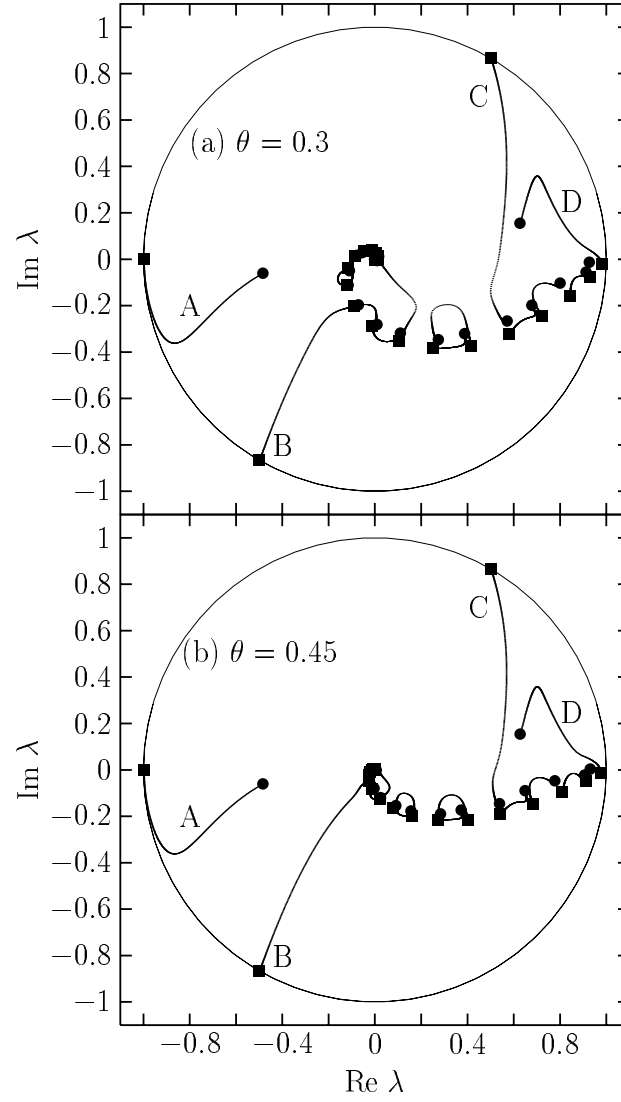


Figure 6.2: Movement of eigenvalues for the time-periodic Rosen-Morse system with $\omega = 1$. The eigenvalues are shown for ϵ ranging from 0 to 2.4 a.u. The filled squares indicate the eigenvalues at $\epsilon = 0$ and the filled circles indicate the eigenvalues at $\epsilon = 2.4$. Both plots use regular complex scaling with a box size $L = 40$ a.u. and 100 basis states. In (a) the scaling angle is $\theta = 0.3$ and in (b) it is $\theta = 0.45$. The labels A , B , C , and D indicate the eigenvalue curves associated with the four resonance states. The eigenvalues on the continuum spiral move slightly as ϵ is increased.

spiral and falls in toward the origin. In Fig. 6.2b this process is not as clearly visible. Close inspection reveals that the same process is taking place but much closer to the continuum spiral than in Fig. 6.2a. This is not surprising as the spiral has changed its position (as expected) in Fig. 6.2b.

Figure 6.3 shows the movement of the eigenvalues for the states calculated using ECCS, which is the technique that we use to compute the eigenfunctions that we will examine in the next section. Again, the same general features appear. For these calculations the box size is larger, so the density of discretized continuum states is greater. In Fig. 6.3b the eigenvalues of the resonance states are shown for several field strengths without the continuum spiral. The points shown in this plot are for values of ϵ that are regularly spaced by increments of 0.3 a.u. from $\epsilon = 0$ to $\epsilon = 2.4$ a.u. Some states do not have eigenvalues for high values of ϵ because the states are no longer identifiable as resonance states at these high field strengths. Fig. 6.3b indicates that state *B* is the first to be destroyed, followed by state *C*, while states *A* and *D* remain outside of the continuum spiral at $\epsilon = 2.4$ a.u.

6.3 Phase-space Picture

We wish to study the changes in the phase-space structure of the resonance eigenstates as they are destroyed. We will again use the Husimi distribution (see App. B) to represent the states in phase-space. We can calculate the Husimi distributions for

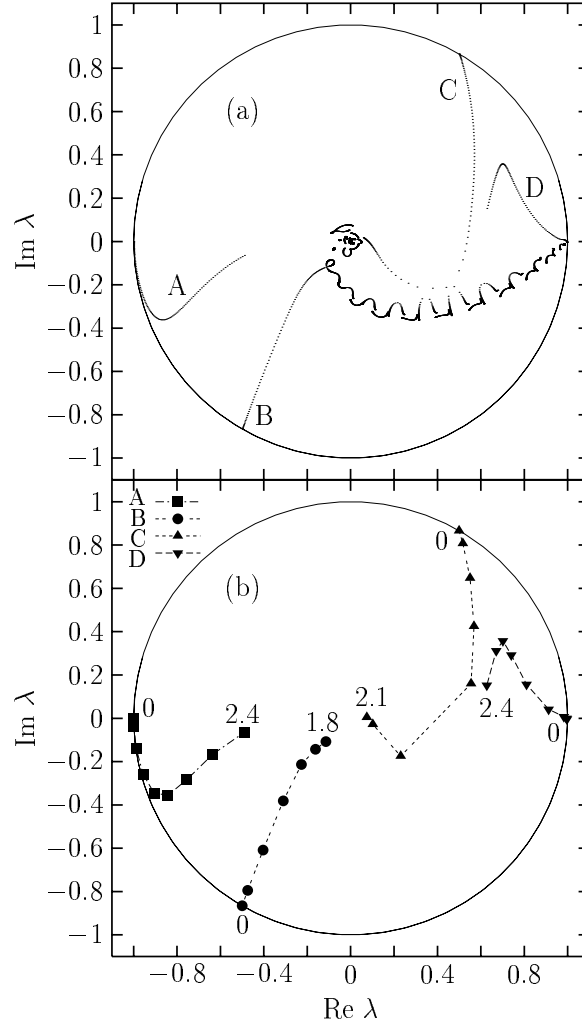


Figure 6.3: Movement of eigenvalues calculated using exterior complex scaling, with $\omega = 1$, $\theta = 0.45$. The eigenvalues are calculated using a box size $L = 80$ and 200 basis states with the coordinate complex-scaled only in the region $|x| > 10$ a.u. In (a) the eigenvalues for all 200 states are shown for ϵ ranging from 0 to 2.4 a.u. In (b) only the eigenvalues of the four resonance states are shown for $\epsilon = 0$ to 2.4 a.u., in steps of 0.3 a.u. The numbers in the plot indicate the values of ϵ at the end points. Eigenvalues for state B stop at $\epsilon = 1.8$ a.u. because at higher field strengths that state can no longer be identified. Eigenvalues for state C stop at $\epsilon = 2.1$ a.u. for the same reason. The lines in (b) are intended only to aid the eye.

these exterior scaled states using the usual procedure because there is no complex scaling in the interaction region. As explained in the previous chapter, as long as we only compute Husimi distributions within the interaction region we do not have to worry about the effects of the complex scaling.

Figure 6.4 shows the Husimi distributions for state A (as labeled in Fig. 6.3) at several field strengths. State A is the ground state of the system at $\epsilon = 0$. The change in the phase-space structure of state A corresponds well to what is seen in the movement of its eigenvalue. At low field strengths the state is only slightly distorted from its original form and its eigenvalue remains close to the edge of the unit circle, indicating that the state has a long lifetime. For very high values of ϵ the eigenvalue has moved significantly toward the origin and the Husimi distribution of the state is no longer well-localized within the interaction region. This is an indication that it is coupling with the continuum states, which lie outside of the interaction region, that leads to the destruction of this resonance state.

Figure 6.5 shows Husimi distributions for state B , the first excited state at $\epsilon = 0$, for several field strengths. This state is the first of the resonance states to be destroyed as ϵ is increased. This is indicated in the Husimi distribution of the state which already shows a significant flow of probability out of the interaction region for $\epsilon = 0.3$ a.u. This process continues as ϵ is increased and at $\epsilon = 0.9$ a.u. the majority of the state's probability is located outside of the interaction region.

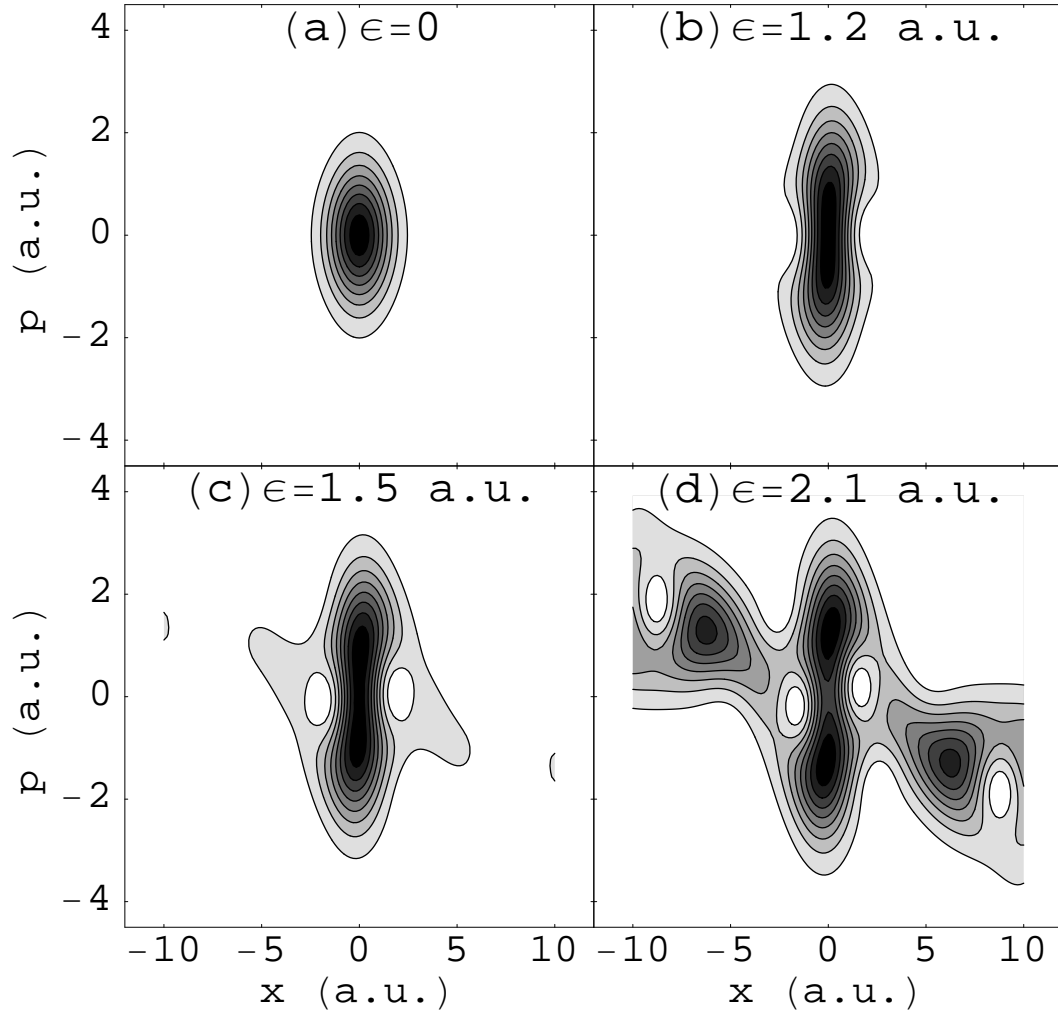


Figure 6.4: Husimi distributions for state A at several field strengths. This state remains localized within the interaction region for field strengths below $\epsilon = 1.5$ a.u. The lifetimes of the resonance states (in units of the driving period $T = 2\pi/\omega$) are (b) $\tau = 16.1T$, (c) $\tau = 5.5T$, and (d) $\tau = 1.2T$.

Again, this corresponds to the rapid movement of state B 's eigenvalue curve from the unit circle to the origin in Fig. 6.3. For $\epsilon > 0.9$ a.u. the eigenvalue of this state has merged with the continuum spiral and the phase-space structure of the state is indistinguishable from that of a discretized continuum state.

Figure 6.6 shows the Husimi distributions of state C , the second excited state at $\epsilon = 0$, for several field strengths. The changes in the phase-space structure of this state as ϵ is increased are similar to those undergone by state B , although state C is destroyed at a higher value of ϵ than is state B . State C has an avoided crossing with the continuum near $\epsilon = 1.5$ a.u. which we will examine in detail later in this chapter.

Husimi distributions for state D , which is a quasibound state at $\epsilon = 0$, are shown in Figure 6.7. By $\epsilon = 0.9$ a.u. the phase-space structure of this state has changed significantly from its structure at $\epsilon = 0$. The state has become much more localized within the interaction region. This corresponds with the emergence of this state's eigenvalue from the continuum spiral. As ϵ is increased further the state becomes increasingly localized within the interaction region, but then begins to delocalize after $\epsilon \approx 1.8$ a.u. This matches the turning point of the eigenvalue trajectory for state D in Fig. 6.3, where the eigenvalue begins to move rapidly toward the origin as ϵ is increased.

The pattern observed for all four resonance states is that they maintain rel-

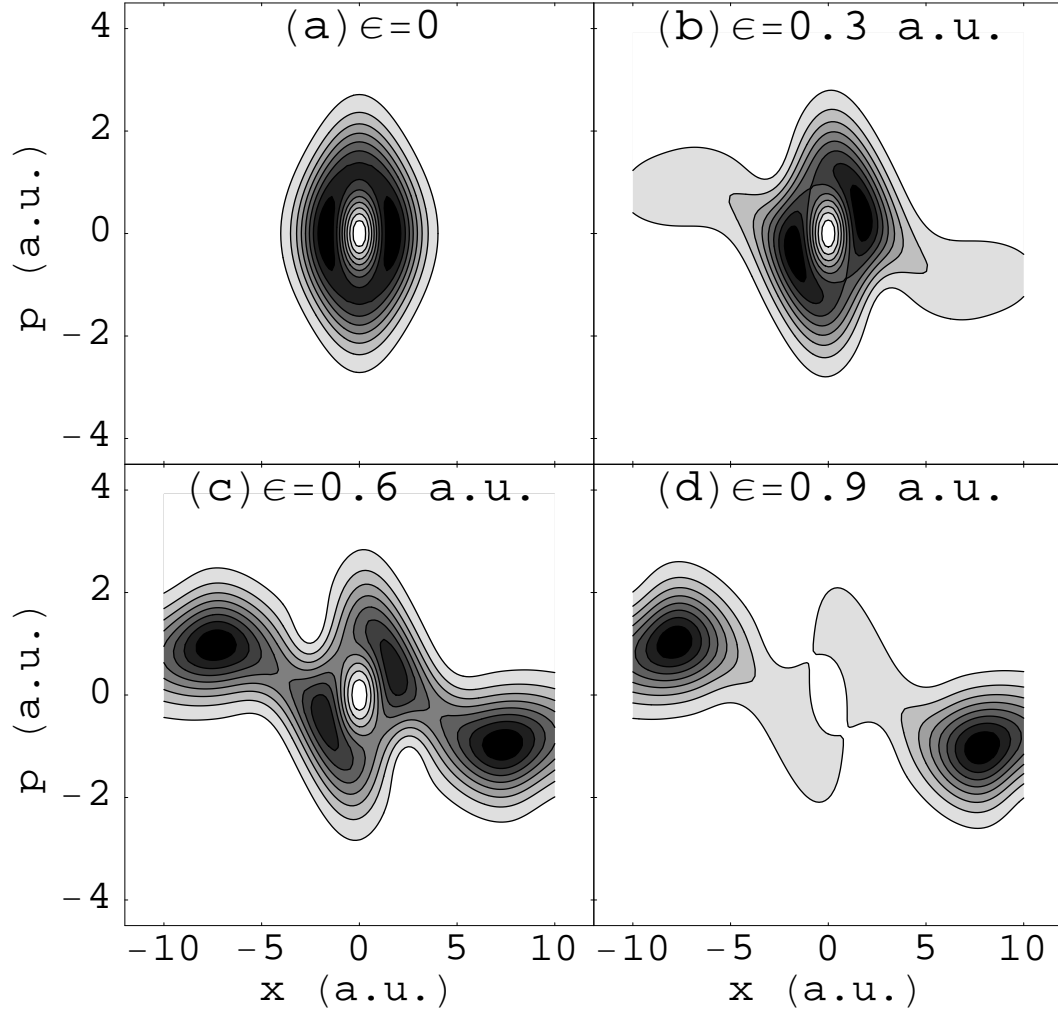


Figure 6.5: Husimi distributions for state B at several field strengths. This state is localized in the interaction region only at very low field strengths. At $\epsilon = 0.9$ a.u. this state is located almost entirely outside the interaction region. The lifetimes of the resonance states (in units of the driving period $T = 2\pi/\omega$) are (b) $\tau = 6.4T$, (c) $\tau = 1.6T$, and (d) $\tau = 0.7T$.

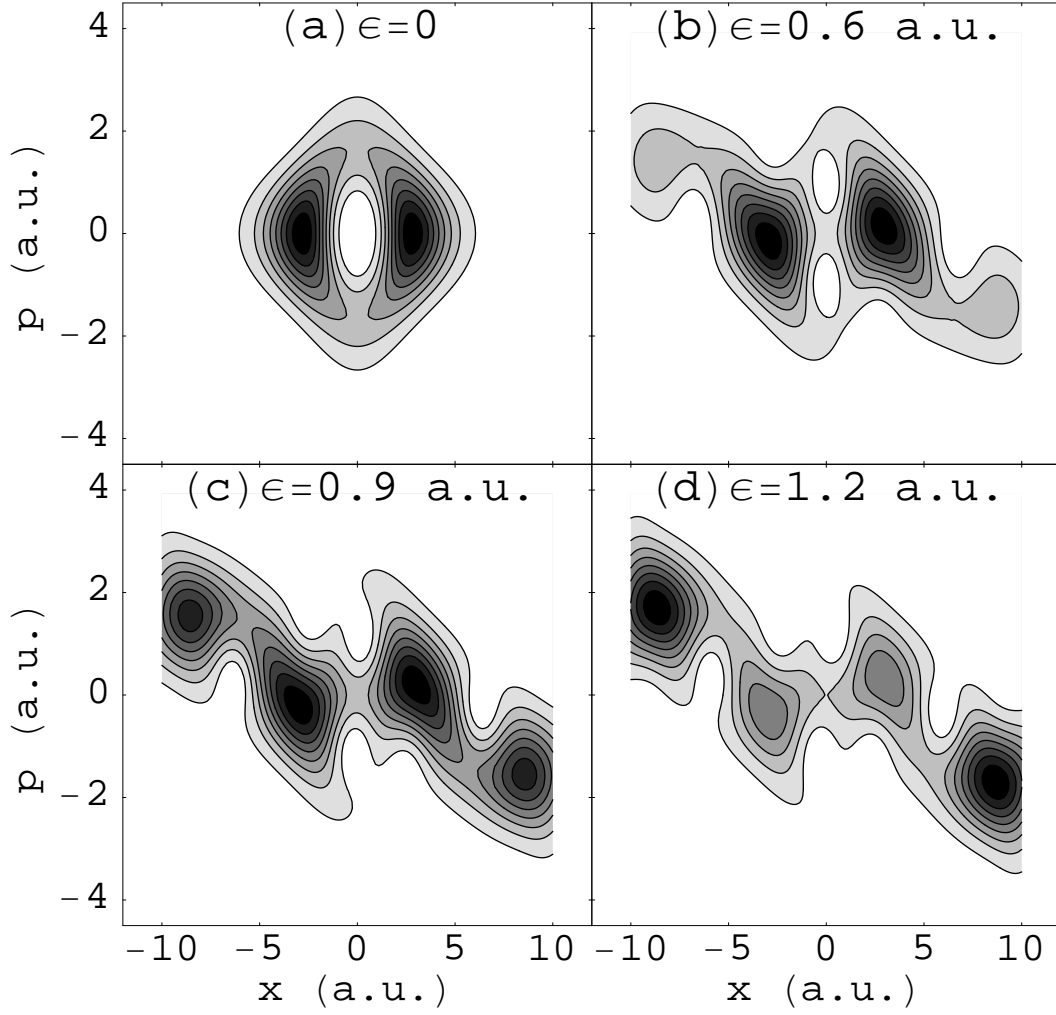


Figure 6.6: Husimi distributions for state C at several field strengths. This state is localized in the interaction region only for low field strengths. For $\epsilon = 1.2$ a.u. it is located mostly outside of the interaction region. The lifetimes of the resonance states (in units of the driving period $T = 2\pi/\omega$) are (b) $\tau = 3.1T$, (c) $\tau = 1.5T$, and (d) $\tau = 0.9T$.

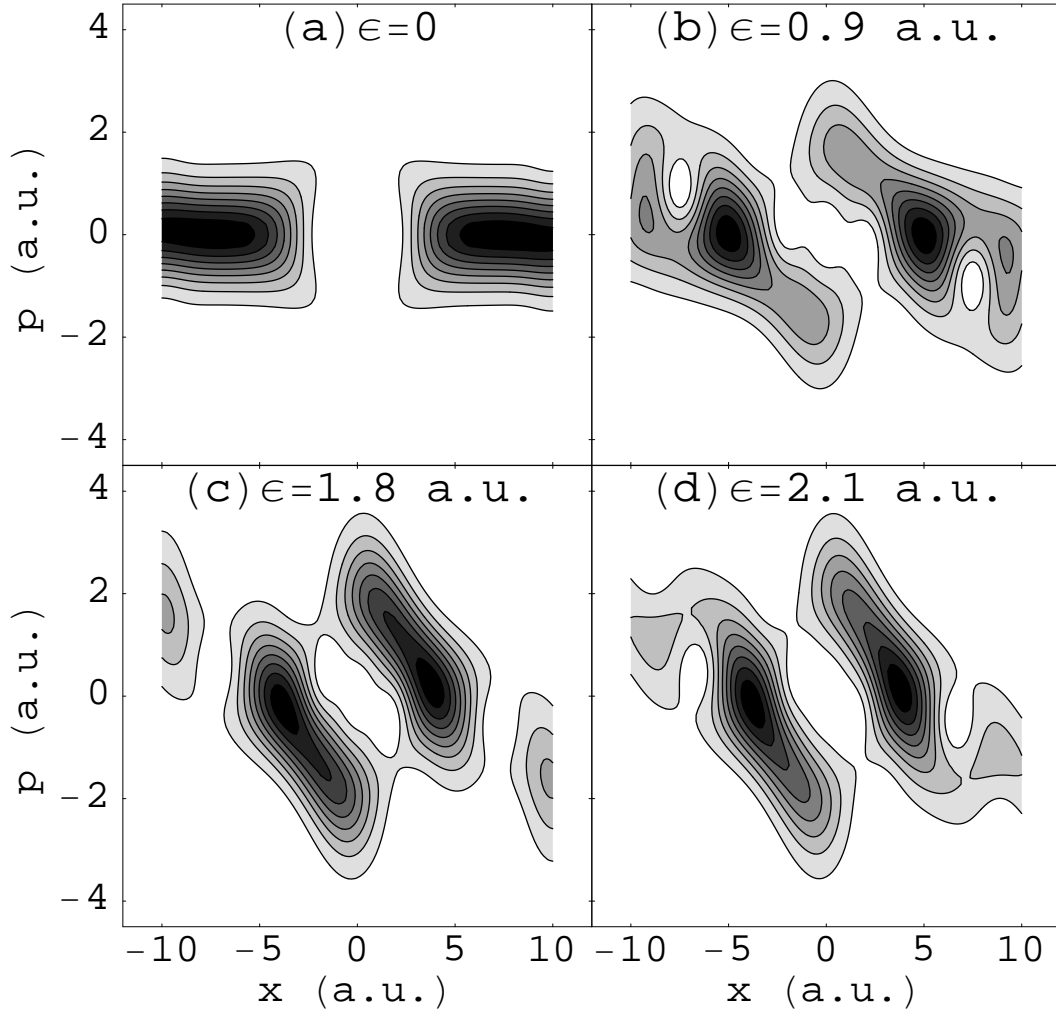


Figure 6.7: Husimi distributions for state D at several field strengths. At $\epsilon = 0$ this state is in the continuum (it has positive energy). At higher value of ϵ it becomes a resonance state and it becomes concentrated in the interaction region. For very high ϵ it begins to move out of the interaction region. The lifetimes of the resonance states (in units of the driving period $T = 2\pi/\omega$) are (b) $\tau = 5.5T$, (c) $\tau = 2.1T$, and (d) $\tau = 1.7T$.

atively long lifetimes as long as their phase-space structure is well-localized and isolated within the interaction region. As ϵ is increased the states become strongly coupled to the continuum and their phase-space structure is altered so that it is no longer localized. This is accompanied by a significant reduction in the lifetimes of the states as their eigenvalues move toward the origin in Fig. 6.3. In the next section we will investigate the causes of the strong coupling to the continuum that leads ultimately to the destruction of these resonance states.

6.4 Coupling to the Continuum

The Husimi distributions discussed in the previous section indicate that it is strong coupling of the resonance states to the continuum that leads to their destruction. To quantify this coupling we must investigate a form of perturbation theory for these Floquet states. If one knows the eigenstates for a particular field strength ϵ , one can calculate the eigenstates for a slightly higher field strength $\epsilon + \delta\epsilon$ using a form of time-independent perturbation theory [24]. The term that leads to mixing of states as ϵ is increased is proportional to the time-average of the matrix

$$\langle \alpha | V_0(x) | \beta \rangle, \quad (6.3)$$

where $|\alpha\rangle$ and $|\beta\rangle$ are Floquet eigenstates and $V_0(x)$ is the time-independent Rosen-Morse potential. To measure how strongly a resonance state is coupled to the

continuum we define

$$R_\alpha^c = \left(\sum_{\beta \in C} |\langle \alpha | V_0(x) | \beta \rangle|^2 \right) / \left(\sum_{\text{all } \beta} |\langle \alpha | V_0(x) | \beta \rangle|^2 \right), \quad (6.4)$$

where α labels a resonance state, the first sum is over only the continuum states, and the second sum is over all Floquet eigenstates. No time average is taken, but we find that this quantity provides a good measure of the coupling of a resonance state to the continuum.

Figure 6.8 shows R_α^c versus ϵ for all four of the resonance states in this system. The results are consistent with what was observed in the Husimi distributions and eigenvalue trajectories. State *A* remains only weakly coupled to the continuum until $\epsilon \approx 1.2$ or so, then gradually becomes more strongly coupled to the continuum as its Husimi distribution is delocalized (Fig. 6.4) and its eigenvalue moves toward the origin (Fig. 6.3). State *B* starts off with relatively weak coupling to the continuum but becomes strongly coupled after a small increase in ϵ , which is consistent with the destruction of this resonance state at low ϵ described earlier. State *C* is strongly coupled to the continuum at $\epsilon = 0$ (not surprising since the state is only weakly bound), but its coupling does not increase significantly as ϵ is increased. This may explain why state *C* survives for higher field strengths than does state *B*. State *D* actually shows a decrease in its coupling to the continuum as ϵ is increased and its eigenvalue moves away from the continuum spiral. At high values of ϵ this trend reverses as state *D* begins to delocalize (Fig. 6.7) and its eigenvalue moves toward

the origin (Fig. 6.3).

To determine whether or not the strong coupling to the continuum is related to photon absorption, we must have some measurement for the ionization energy of the resonance states. For this purpose we examine the real part of the quantity

$$H_\alpha = \langle \alpha | H_0 | \alpha \rangle, \quad (6.5)$$

which is the expectation value of the time-independent Hamiltonian for the resonance state $|\alpha\rangle$. Figure 6.9 shows the real part of H_α versus ϵ for all four resonance states. State *A* is midway between the one- and two-photon ionization energies at $\epsilon = 0$, which is consistent with its low value of R_α^c at low field strengths. State *A* crosses the one-photon ionization energy near $\epsilon = 1.2$ a.u., which is very close to the field strength at which its R_α^c value begins to increase. State *B*, on the other hand, starts out much closer to the one-photon ionization energy than does state *A* and it rapidly moves closer to that energy as ϵ is increased. This is consistent with the rapid increase of R_α^c for this state as ϵ is increased. After about $\epsilon = 0.9$ a.u. state *B*'s energy increases rapidly until it crosses the threshold and state *B* ceases to be a resonance state. The picture is less clear for states *C* and *D*. State *C* starts with an energy near the threshold, but moves toward lower energies as ϵ is increased, which is consistent with the relatively flat value of R_α^c seen in Fig. 6.8c. However, at $\epsilon = 1.5$ a.u. this state has an anomalously low value for $\text{Re } H_\alpha$. This may be the result of an avoided crossing that the state goes through at this field strength. For

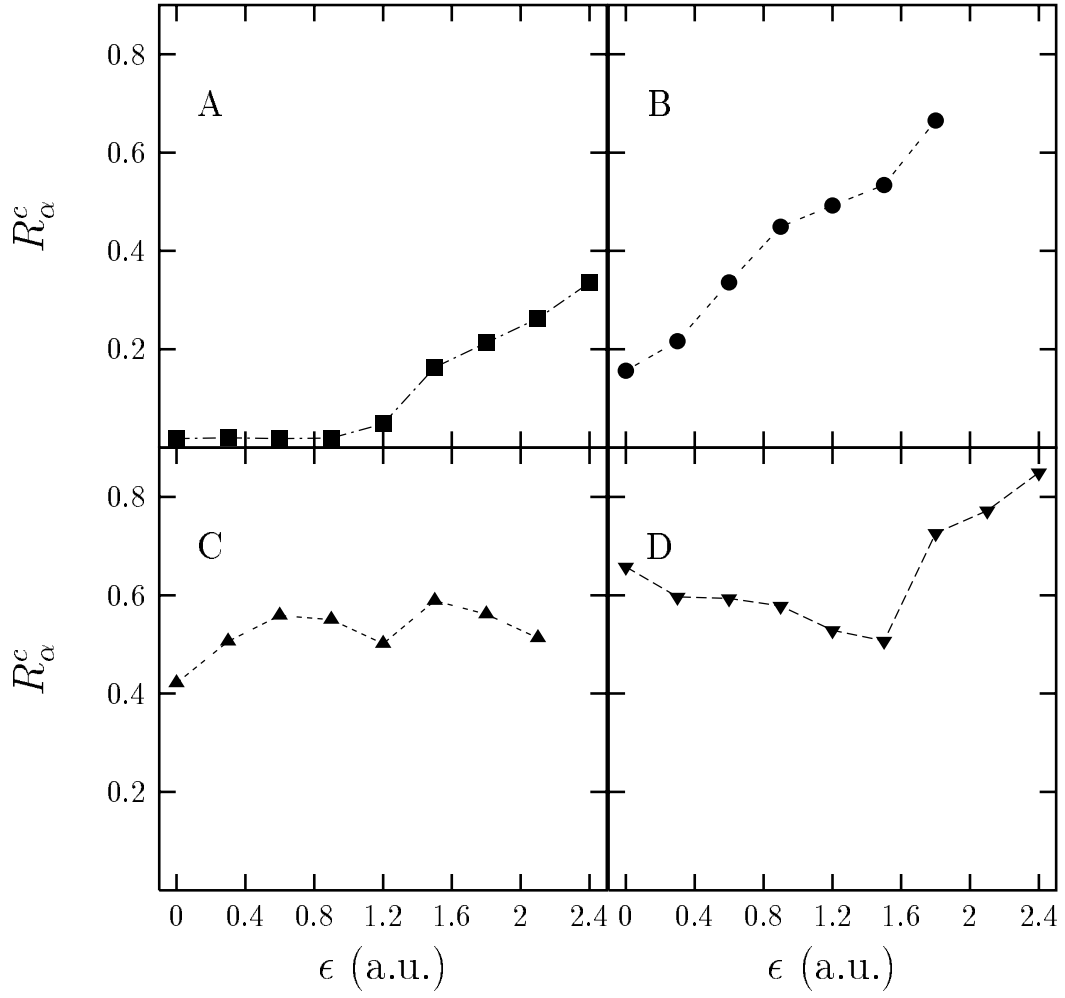


Figure 6.8: Plots of R_α^c versus ϵ for all four resonance states. R_α^c is a dimensionless quantity that indicates how strongly a given state is coupled to the continuum (see Eq. 6.4). Strong coupling to the continuum results in a decrease in the state's lifetime as ϵ is increased.

higher field strengths state C 's energy increases rapidly until it crosses the threshold and merges with the continuum. State D 's energy remains close to the threshold and does not show any clear correlation with the plot in Fig. 6.8d.

It is apparent that the destruction of the resonance states in this system is the result of the threshold effect described in Ref. [79]. When a state's ionization energy approaches the photon energy as ϵ is increased, that state's coupling to the continuum will increase. This causes the state to become delocalized in phase-space and its lifetime to decrease. As ϵ is increased further the state will gradually become more delocalized, with a shorter lifetime, until it merges into the continuum and ceases to be a resonance state.

6.5 Avoided Crossing

Overlapping avoided crossings can play a major role in delocalizing Floquet states in bound systems [76]. Because of the complexity of an open system, it is important to examine even isolated avoided crossings that involve resonance states to determine what role they play in the destruction of these states. In this section we will examine two avoided crossings between resonance states and the continuum. The first is shown in Figure 6.10, which is a detail from Fig. 6.3a. Fig. 6.10 shows that the original state C (now labeled C_1 in Fig. 6.10) undergoes an avoided crossing with one continuum state (labeled C_2), which is then ejected from the continuum spiral

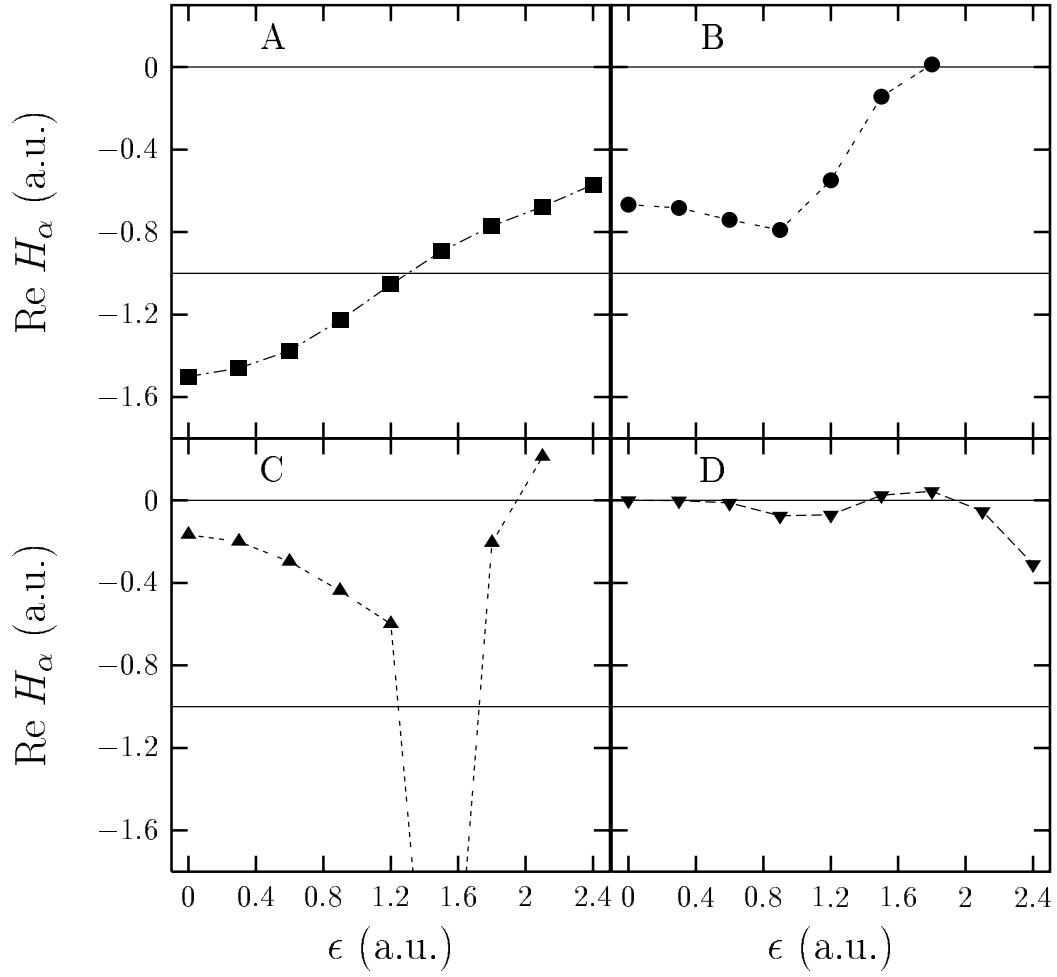


Figure 6.9: Plots of the real part of H_α versus ϵ for all four resonance states. H_α is the expectation value of the time-independent Hamiltonian H_0 for a quasienergy state $|\alpha\rangle$. Lines are drawn at the ionization threshold ($H_\alpha = 0$) and the one-photon resonance ($H_\alpha = -\omega$). State C has an anomalously low value of $\text{Re } H_\alpha$ at $\epsilon = 1.5$ a.u., which may be because that state is involved in an avoided crossing near $\epsilon = 1.5$ a.u.

while state C_1 merges into that spiral. State C_2 then has an avoided crossing with a third state (C_3) and then moves off toward the origin. In fact, what we have been referring to as state C is really two different states, C_1 and C_2 . In the previous sections we chose to follow C_2 rather than C_1 for $\epsilon > 1.43$ because at these field strengths state C_1 is in the continuum spiral while state C_2 is outside the spiral.

Figure 6.11 shows the Husimi distributions of the states C_1 , C_2 , and C_3 in the vicinity of the avoided crossings. The most striking thing about these Husimi distributions is how similar they are to each other even before the avoided crossings take place. This is an indication that these states are already strongly coupled before their eigenvalues approach each other. However, the phase-space structure of these states does undergo some modification as they pass through the avoided crossings. State C_1 becomes somewhat more localized and its lifetime increases as it passes through the avoided crossing. State C_3 remains approximately constant in both structure and lifetime throughout this range of ϵ . State C_2 on the other hand, loses nearly all of its probability in the interaction region and its lifetime decreases substantially as it passes through the avoided crossing.

This avoided crossing does not seem to play a major role in the destruction of the resonance state C because the state C is already strongly coupled to the continuum before the avoided crossing. However, the avoided crossing may modify the way in which the destruction of the resonance takes place. In this case the

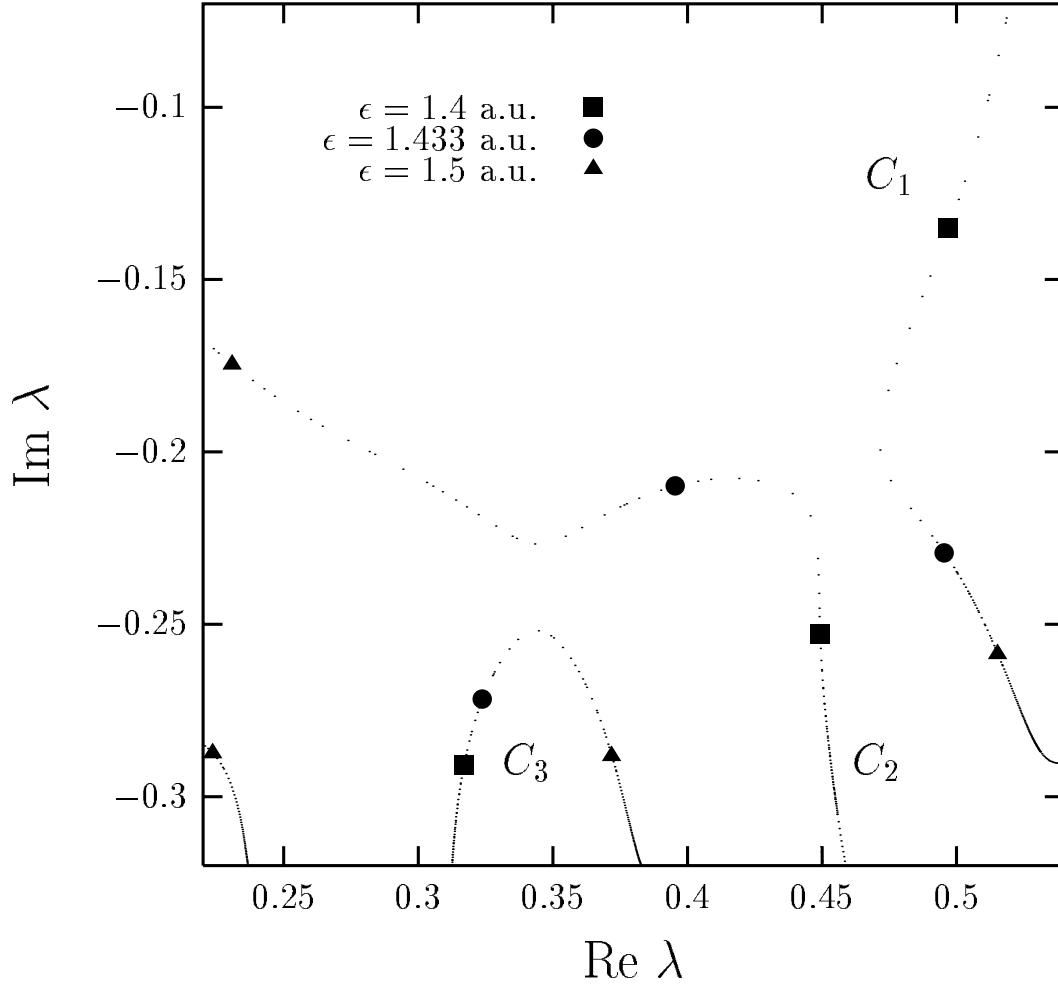


Figure 6.10: Detail from Fig. 6.3a showing an avoided crossing involving state C . The curve labeled C_1 is the same as the curve labeled C in Fig. 6.3. C_2 labels the state that has the first avoided crossing with C_1 near $\epsilon = 1.42$ a.u. and C_3 labels the state that has an avoided crossing with C_2 near $\epsilon = 1.45$ a.u. The markers indicate the eigenvalues at $\epsilon = 1.4, 1.433, \text{ and } 1.5$ a.u.

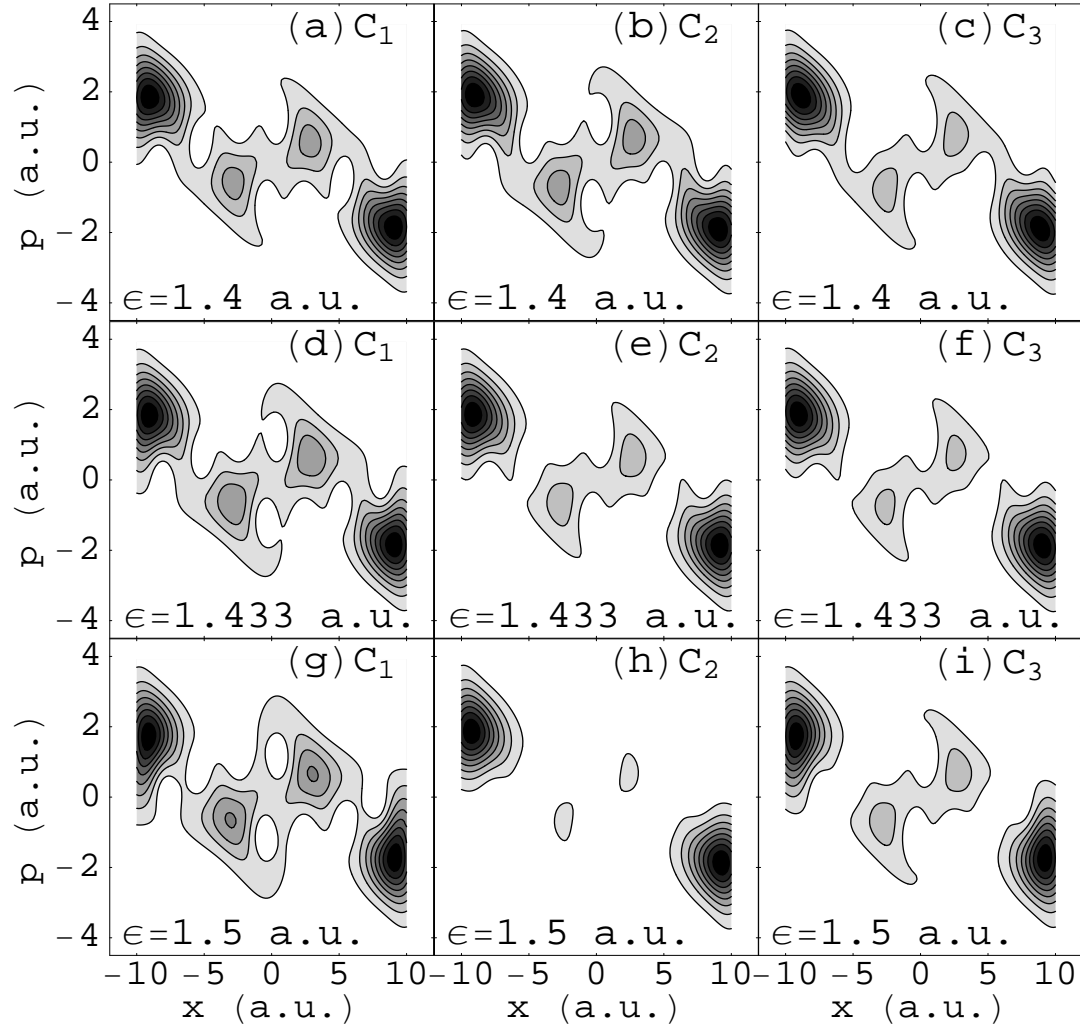


Figure 6.11: Husimi distributions of the states involved in the avoided crossings shown in Fig. 4.5. The lifetimes (in units of the driving period $T = 2\pi/\omega$) are (a) $\tau = 0.75T$, (b) $\tau = 0.75T$, (c) $\tau = 0.59T$, (d) $\tau = 0.83T$, (e) $\tau = 0.62T$, (f) $\tau = 0.58T$, (g) $\tau = 0.91T$, (h) $\tau = 0.40T$, and (i) $\tau = 0.66T$.

original state C merges into the continuum spiral well away from the origin in Fig. 6.3, but as it does so it ejects one of the original continuum states. This state is now a resonance state, since it is no longer in the continuum spiral, but its eigenvalue moves rapidly toward the origin and it is no longer identifiable as a resonance state for $\epsilon > 2.1$ a.u.

Figure 6.12 shows another avoided crossing, this time between state B (labeled B_1 in the figure) and a discretized continuum state (labeled B_2). This avoided crossing occurs close to the origin in Fig. 6.3a, indicating that state B has a very small lifetime when it passes through this avoided crossing. Figure 6.13 shows the Husimi distributions of the two states at field strengths below and above the critical field strength for the avoided crossing. The two states are nearly identical before and after the avoided crossing, indicating that they are already strongly coupled prior to the avoided crossing. Again, this avoided crossing does not seem to contribute to the destruction of the resonance state.

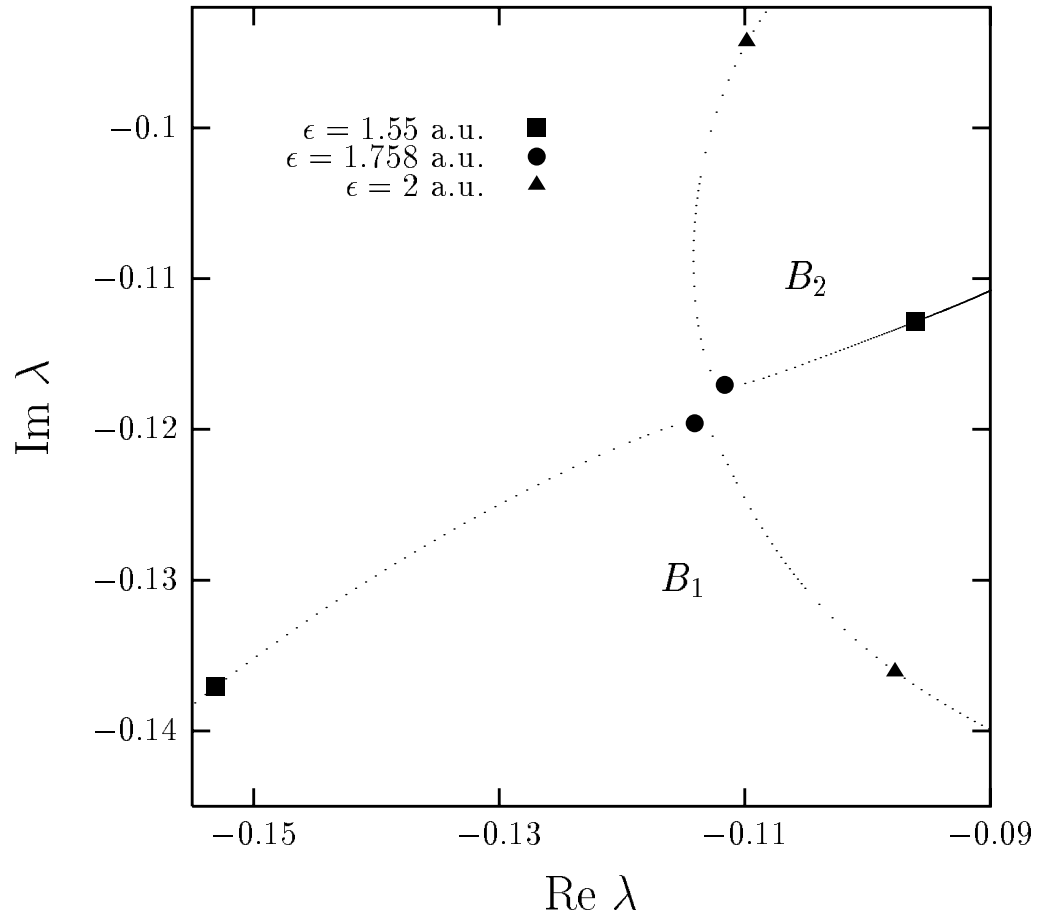


Figure 6.12: Detail from Fig. 6.3a showing an avoided crossing involving state B . The curve labeled B_1 is the same as the curve labeled B in Fig. 6.3a. B_2 labels the state that has an avoided crossing with B_1 near $\epsilon = 1.76$. The markers indicate the eigenvalues at $\epsilon = 1.55, 1.758$, and 2 a.u.

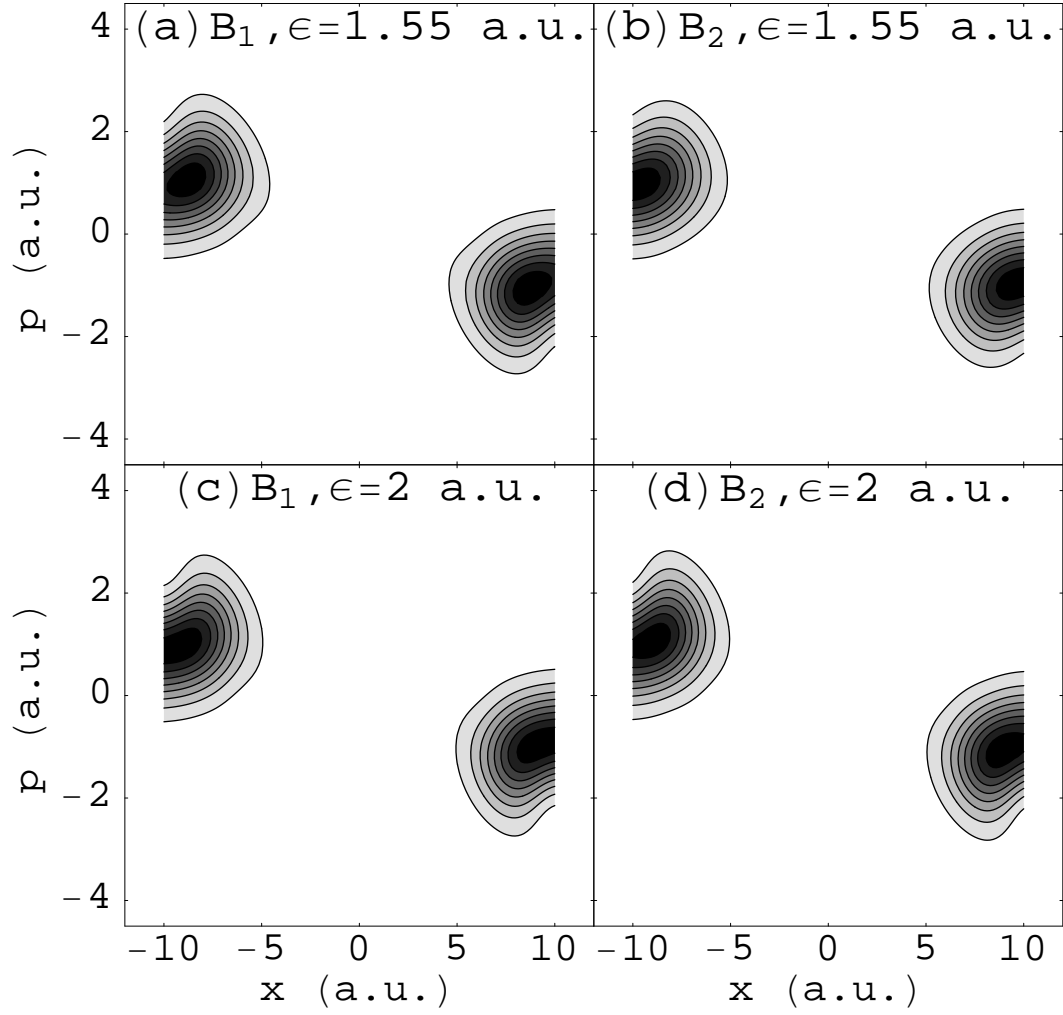


Figure 6.13: Husimi distributions of the states involved in the avoided crossing shown in Fig. 6.12. The lifetimes (in units of the driving period $T = 2\pi/\omega$) are (a) $\tau = 0.32T$, (b) $\tau = 0.26T$, (c) $\tau = 0.28T$, and (d) $\tau = 0.26T$.

Chapter 7

Conclusions and Discussion

We began our study of time-periodic quantum systems by introducing the driven infinite square well. In Chapter 2 we investigated how the underlying classical dynamics affects the radiation spectrum of the quantum system. The simulations described in Chapter 2 mimic the procedure of a laboratory experiment, in that the system is in an unperturbed initial state and is then subjected to a driving field that is ramped on as a function of time. We found that initial quantum states that were located in the classically regular region produce very little harmonic generation. Initial states located in a resonance region produce a noisy spectrum with the highest emitted frequencies determined by the energy range of the classical resonance. States in the chaotic region produce high harmonics with a cutoff determined by the energy range of that region. Avoided crossings in the quasienergy spectrum can lead to

population transfer as the driving field is ramped on, putting the system into a superposition of Floquet states that can radiate at high harmonics. This indicates that avoided crossings might be used to engineer high harmonics in real systems. A properly shaped pulse could produce a superposition of Floquet states that radiates efficiently at high frequencies.

Continuing our study of the driven square well system, we deviated in Chapter 3 from mimicking an experimental procedure. Instead we focused on the structure of the Floquet eigenstates. In Chapter 3 we identified two types of avoided crossings: isolated (or sharp) and overlapping (or broad). Sharp avoided crossings cause the structure of the two states involved to mix, but this mixing is undone as the field strength is increased beyond the critical value for the avoided crossing. In a broad avoided crossing the mixing among the states remains at field strengths beyond the critical value. This can lead to the delocalization of the Floquet states that are involved in the avoided crossing. Broad avoided crossings can also lead to increased high harmonic generation in the radiation spectrum of an individual Floquet state, while sharp avoided crossings result in only a transient increase in high harmonic generation.

In Chapter 4 the concept of information entropy is used as a measure of the localization of Floquet eigenstates. We showed that overlapping avoided crossings lead to an overall increase in the entropy (and delocalization) of the system. How-

ever, even after the system has passed through many overlapping avoided crossings some states may remain localized. We identified the classical mechanism behind this persistent localization at high field strengths. We discussed the relationship between classical chaos, avoided crossings, delocalization of eigenstates, and changes in eigenvalue statistics. We ended our investigation of the driven square well by proposing a matrix picture of the transition to chaos in this system. This picture of how the quantum system evolves as the driving field is increased can consistently account for the phenomena we have seen in our study.

We extended our study to include open systems in Chapter 5. We used the technique of complex coordinate scaling to compute the Floquet eigenstates of an inverted Gaussian well driven by a periodic field. The number of quasibound states in this system increases as the driving field is increased, even though the classical dynamics becomes increasingly unstable. We determined that the newly created resonance states are scarred on unstable periodic orbits of the classical motion. These periodic orbits move apart from each other as the field strength is increased and this allows for the creation of new quantum resonance states. Also in Chapter 5 we closely examined the structural changes of two resonance states as they passed through an avoided crossing with each other. The results were similar to that seen in the sharp avoided crossing in Chapter 3.

In Chapter 6 we studied the destruction of resonance states in the time-

periodic Rosen-Morse system. We found that the resonance states, initially well-localized in the interaction region, experience a flow of probability out of the interaction region as the driving field is increased. This phenomenon is the result of coupling to the continuum which occurs because of resonant photon absorption. We also examined two avoided crossings between resonance states and the continuum and found that, because the resonance states are already strongly coupled to the continuum before the avoided crossing occurs, there is relatively little change in the structure of the eigenstates as they pass through the avoided crossing.

These investigations provide an overall picture of how a quantum system changes its character as its classical analog becomes chaotic. For bound systems this picture is described in detail in Chapter 4, although we have not yet established the connection between periodic orbits and this matrix picture. Open systems present some difficulties which are indicated in our studies of the inverted Gaussian and Rosen-Morse systems. The interaction of resonance states with each other, as seen in the avoided crossing of Chapter 5, can be similar to the interaction of states in a bound system. However, the phenomena of resonance creation and destruction cannot be effectively described by the matrix picture given in Chapter 4. In both open and closed systems, though, it is clear that chaos in the classical system plays an important role in determining the dynamics of the quantum system.

Appendix A

Floquet Theory

Time-dependent quantum systems have no energy eigenstates because these systems have Hamiltonians that are not invariant under an infinitesimal time translation. However, the Hamiltonian of a time-periodic system is invariant under a discrete time translation $t \rightarrow t + T$, where T is the period of the time-dependent term in the Hamiltonian. Because of this symmetry it is possible to define eigenstates for a time-periodic quantum system that characterize the quantum dynamics in much the same way that energy eigenstates characterize a time-independent quantum system. These are the Floquet eigenstates [82].

Floquet eigenstates are eigenstates of the one-period time evolution operator $\hat{U}(T)$. These eigenstates satisfy

$$\hat{U}(T)|\Omega_\alpha\rangle = e^{-i\Omega_\alpha T/\hbar}|\Omega_\alpha\rangle, \quad (\text{A.1})$$

where Ω_α is the quasienergy associated with the Floquet state $|\Omega_\alpha\rangle$. For a closed quantum system the time evolution will be unitary and the Floquet eigenvalues, $e^{-i\Omega_\alpha T/\hbar}$, will have unit modulus. This means that the quasienergies of closed systems will be real. Open systems that allow ionization will have a non-unitary time evolution which leads to Floquet eigenvalues with less than unit modulus and complex quasienergies with negative imaginary parts. It is apparent from Eq. A.1 that the real part of the quasienergy is only defined modulo $\omega_0\hbar = 2\pi\hbar/T$.

The Floquet eigenvalues and eigenstates can be computed numerically by first calculating the matrix $\hat{U}(T)$ in some convenient basis (usually the eigenstates of the Hamiltonian with the time-dependent term removed). To compute $\hat{U}(T)$ one simply integrates the Schrödinger equation N times (where N is the number of basis states) from $t = 0$ to $t = T$ with initial conditions $|\Psi(t = 0)\rangle = |n\rangle$, where $|n\rangle$ is the n^{th} basis state ($1 \leq n \leq N$). The wavefunction at the end of each integration is a vector of length N that forms the n^{th} column of the matrix $\hat{U}(T)$. A numerical diagonalization of this matrix produces the eigenvalues and eigenvectors.

Appendix B

The Husimi Distribution

Visualization of the quantum mechanical phase-space requires the construction of a phase-space probability density for the various quantum eigenstates. The uncertainty principle prevents the construction of a true phase space probability density in the classical sense, but it is possible to construct a quasiprobability density that is positive definite and gives a coarse-grained picture of the distribution of the quantum state in phase-space. One such quasiprobability density is the Husimi distribution [83]. To construct the Husimi distribution of a given quantum state one simply calculates the overlap between the given state and a minimum uncertainty wavepacket centered on a particular point (x_0, p_0) in phase space. The wavepacket is given in configuration space by [84]

$$\langle x|x_0, p_0\rangle = \left(\frac{1}{\sigma^2\pi}\right)^{1/4} \exp\left(-\frac{(x-x_0)^2}{2\sigma^2} + \frac{ip_0(x-x_0)}{\hbar}\right), \quad (\text{B.1})$$

where σ is a coarse-graining parameter that determines the relative widths of the wavepacket in the x and p directions. Calculating $|\langle\psi|x_0, p_0\rangle|^2$ for a grid of phase space points will produce a quasiprobability distribution that can be easily viewed as a contour plot. These contour plots can be used to visualize the phase space structure of quantum states. This structure can then be compared with structures in a strobe plot of the classical phase space.

Appendix C

Transformation from Radiation to Length Gauge

The Hamiltonian of a one-dimensional system interacting with a driving field in the radiation gauge can be written

$$H(q, p, t) = \frac{1}{2m} \left(p - \frac{\epsilon}{\omega} \sin(\omega t) \right)^2 + V(q) \quad (\text{C.1})$$

where q is the canonical coordinate, p is the canonical momentum, m is the mass of the particle, ϵ is the strength of the driving field, and ω is the frequency of the driving field. The transformation to the length gauge is achieved through the generating function [85]

$$F_2(q, P, t) = qP + q \frac{\epsilon}{\omega} \sin(\omega t) \quad (\text{C.2})$$

so that

$$p = \frac{\partial F_2}{\partial x} = P + \frac{\epsilon}{\omega} \sin(\omega t) \quad (\text{C.3})$$

$$Q = \frac{\partial F_2}{\partial P} = x, \quad (\text{C.4})$$

where Q and P are the canonical coordinate and momentum in the length gauge.

This canonical transformation produces a new Hamiltonian (in terms of Q and P)

given by

$$K = H + \frac{\partial F_2}{\partial t} = \frac{1}{2m} P^2 + V(Q) + \epsilon Q \cos(\omega t). \quad (\text{C.5})$$

This is the Hamiltonian of a one-dimensional system interacting with a driving field

in the length gauge. Note that $q = Q$ at all times, and $p = P$ for $t = 2\pi n/\omega$.

Because of this relationship between the canonical variables in the radiation and

length gauges, strobe plots created using the two different gauges will be identical.

Bibliography

- [1] L. E. Reichl, *The Transition to Chaos In Conservative Classical Systems: Quantum Manifestations* (Springer-Verlag, Berlin, 1983).
- [2] F. Haake, *Quantum Signatures of Chaos* (Springer-Verlag, Berlin, 1992).
- [3] M. V. Berry and M. Wilkinson, Proc. R. Soc. Lond. A **392**, 15 (1984); J. von Neumann and E. Wigner, Phys. Z. **30**, 467 (1929). [English translation in R. Knox and A. Gold, *Symmetry in the Solid State* (W. A. Benjamin, Inc., New York, 1964).]
- [4] S.-J. Wang and S. Y. Chu, Phys. Rev. A **47**, 3546 (1993).
- [5] O. Bohigas, S. Tomsovic, and D. Ullmo, Phys. Rep. **223**, 43 (1993).
- [6] R. C. Brown and R. E. Wyatt, Phys. Rev. Lett. **57**, 1 (1986).
- [7] P. W. Anderson, Rev. Mod. Phys. **50**, 191 (1978).

- [8] F. L. Moore, J. C. Robinson, C. F. Bharucha, B. Sundaram, and M. G. Raizen, Phys. Rev. Lett. **75**, 4598 (1995).
- [9] F. M. Izrailev, Phys. Rep. **196**, 299 (1990).
- [10] R. A. Marcus, in *Horizons of Quantum Chemistry*, Proceedings of the 3rd International Congress on Quantum Chemistry, Kyoto, 1979, edited by K. Fukui and B. Pullman (Reidel, Dordrecht-Holland, 1980), p. 107; R. A. Marcus, in *Nonlinear Dynamics*, Conference Proceedings, N.Y.A.S., New York, 1980.
- [11] M. Tabor, *Chaos and Integrability in Nonlinear Dynamics* (Wiley, New York, 1989).
- [12] M. C. Gutzwiller, *Chaos in Classical and Quantum Mechanics* (Springer-Verlag, New York, 1990).
- [13] E. J. Heller, P. W. O'Connor, and J. Gehlen, Phys. Scr. **40**, 354 (1989); E. B. Bogomolny, Physica D **31**, 169 (1988).
- [14] P. Agostini, F. Fabre, G. Mainfray, G. Petite, and N. K. Raham, Phys. Rev. Lett. **42**, 1127 (1979); P. Kruit, J. Kimman, H. G. Muller, and M. J. van der Wiel, Phys. Rev. A **28**, 248 (1983); R. R. Freeman, P. H. Bucksbaum, H. Milchberg, S. Darack, D. Darack, D. Schumacher, and M. E. Geusic, Phys. Rev. Lett. **59**, 1092 (1987).

- [15] Z. Chang, A. Rundquist, H. Wang, M. M. Murnane, and H. C. Kapteyn, Phys. Rev. Lett. **79**, 2967 (1997); J. J. Macklin, J. D. Kmetec, and C. L. Gordon, Phys. Rev. Lett. **70**, 766 (1993).
- [16] C. O. Reinhold, J. Burgdörfer, M. T. Frey, and F. B. Dunning, Phys. Rev. Lett. **79**, 5226 (1997).
- [17] M. P. de Boer, J. H. Hoogenraad, R. B. Vrijen, R. C. Constantinescu, L. D. Noordam, and H. G. Muller, Phys. Rev. A **50**, 4085 (1994).
- [18] Bala Sundaram and Peter W. Milonni, Phys. Rev. A **41**, 6571 (1990); S. Cocke and L. E. Reichl, **53**, 1 (1996); J. Javanainen, J. H. Eberly, and Q. Su, Phys. Rev. A **38**, 3430 (1988); J. H. Eberly, Q. Su, and J. Javanainen, J. Opt. Soc. Am. B **6**, 1289 (1989); Q. Su and J. H. Eberly, Phys. Rev. A **43**, 2474 (1991).
- [19] W. A. Lin and L. E. Reichl, Physica D **19**, 145 (1986).
- [20] M. Z. Fuka, J. K. McIver, W. Becker, M. Orszag, and R. Ramírez, Phys. Rev. E **51**, 1935 (1995).
- [21] W. A. Lin and L. E. Reichl, Phys. Rev. A **37**, 3972 (1988); J. Y. Shin and H. W. Lee, Phys. Rev. E **50**, 902 (1994).
- [22] G. Gabrielse and H. Dehmelt, Phys. Rev. Lett. **55**, 67 (1985).
- [23] B. Galdrikian, B. Birnir, and M. Sherwin, Phys. Lett. A **203**, 319 (1995).

- [24] B. Birnir, B. Galdrikian, R. Grauer, and M. Sherwin, Phys. Rev. B **47**, 6795 (1993).
- [25] B. Chirikov, Phys. Rep. **52**, 263 (1979).
- [26] Vitali Averbukh and Nimrod Moiseyev, Phys. Rev. A **51**, 3911(1995).
- [27] P. B. Corkum, Phys. Rev. Lett. **71**, 1994 (1993); M. Lewenstein, Ph. Balcou, M. Yu. Ivanov, Anne L’Huillier, and P. B. Corkum, Phys. Rev. A **49**, 2117 (1994).
- [28] F. I. Gauthey, C. H Keitel, P. L. Knight, and A. Maquet, Phys. Rev. A **55**, 615 (1997).
- [29] M. L. Pons, R. Taïeb, and A. Maquet, Phys. Rev. A **54**, 3634 (1996); J. Kamiński, Phys. Lett. A **151**, 308 (1990).
- [30] H. P. Breuer, K. Dietz, and M. Holthaus, Z. Phys. D **8**, 349 (1988).
- [31] H. P. Breuer and M. Holthaus, Z. Phys. D **11**, 1 (1989).
- [32] see *Handbook of Mathematical Functions*, Vol. 55 of *National Bureau of Standards Applied Mathematics Series*, edited by M. Abramowitz and I. A. Stegun (U. S. Gov’t. Printing Office, Washington, DC, 1968).
- [33] W. A. Lin and L. E. Reichl, Phys. Rev. A **40**, 1055 (1989); L. E. Reichl, Phys. Rev. A **39**, 4817 (1989).

- [34] J. Zakrzewski and D. Delande, Phys. Rev. E **47**, 1650 (1993).
- [35] X. Yang and J. Burgdörfer, Phys. Rev. A **48**, 83 (1993); J. Zakrzewski and D. Delande, Phys. Rev. E **47**, 1665 (1993).
- [36] J. Henkel and M. Holthaus, Phys. Rev. A **45**, 1978 (1992).
- [37] L. Bonci, A. Farusi, P. Grigolini, and R. Roncaglia, Phys. Rev. E **58**, 5689 (1998).
- [38] Q. Jie, S.-J. Wang, and L.-F. Wei, Z. Phys. B **104**, 373 (1997).
- [39] M. Latka, P. Grigolini, and B. J. West, Phys. Rev. A **50**, 1071 (1994).
- [40] W. Chism, T. Timberlake, and L. E. Reichl, Phys. Rev. E **58**, 1713 (1998).
- [41] M. S. Santhanam, V. B. Sheorey, and A. Lakshminarayan, Mol. Phys. **88**, 325 (1996).
- [42] S. D. Frischat and E. Doron, J. Phys. A **30**, 3613 (1997); N. Moiseyev, H. J. Korsch, and B. Mirbach, Z. Phys. D **29**, 125 (1994).
- [43] G. P. Berman, O. F. Vlasova, and F. M. Izrailev, Sov. Phys. JETP **66**, 269 (1987).
- [44] E. Vergini and D. A. Wisniacki, Phys. Rev. E **58**, R5225 (1998).

- [45] D. W. Noid, M. L. Koszykowski, M. Tabor, and R. A. Marcus, J. Chem Phys. **72**, 6169 (1980).
- [46] G. O. Morrow and L. E. Reichl, Phys. Rev. A **50**, 2027 (1994).
- [47] B. Sundaram and R. V. Jensen, Phys. Rev. A **47**, 1415 (1993).
- [48] E. J. Heller, Phys. Rev. A **35**, 1360 (1987).
- [49] E. J. Heller, Phys. Rev. Lett. **53**, 1515 (1984).
- [50] M. L. Mehta, *Random Matrices and the Statistical Theory of Energy Levels* (Academic, New York, 1967).
- [51] F. M. Izrailev in *Quantum Chaos - Quantum Measurement*, edited by P. Cvitanovic et al. (Kluwer Academic Publishers, 1992).
- [52] R. Ramaswamy and R. A. Marcus, J. Chem. Phys. **74**, 1385 (1981).
- [53] M. Latka, P. Grigolini, and B. J. West, Phys. Rev. E **50**, 596 (1994).
- [54] B. Galdrikian, M. Sherwin, and B. Birnir, Phys. Rev. B **49**, 13744 (1994).
- [55] M. V. Berry and M. Robnik, J. Phys. A **17**, 2413 (1984).
- [56] E. G. Vergini, J. Phys. A **33**, 4709 (2000); E. G. Vergini and G. G. Carlo, J. Phys. A **33**, 4717 (2000).

- [57] J. L. Shoendorff, H. J. Korsch, and N. Moiseyev, *Europhys. Lett.* **44**, 290 (1998).
- [58] T. Takami, *Phys. Rev. Lett.* **68**, 3371 (1992).
- [59] M. Joyeux, *J. Chem. Phys.* **102**, 2816 (1995).
- [60] M. Pont and M. Gavrila, *Phys. Rev. Lett.* **65**, 2362 (1990); R. M. Potvliege and P. H. G. Smith, *Phys. Rev. A* **48**, R46 (1993).
- [61] W. Chism, D. Choi, and L. E. Reichl, *Phys. Rev. A* **61**, 054702 (2000); R. Grobe and C. K. Law, *Phys. Rev. A* **44**, R4114 (1991); F. Benvenuto, G. Casati, and D. L. Shepelyansky, *Phys. Rev. A* **47**, R786 (1993); R. V. Jensen and B. Sundaram, *Phys. Rev. A* **47**, R778 (1993); G. Casati, I. Guarneri, and G. Mantica, *Phys. Rev. A* **50**, 5018 (1994).
- [62] S. Yoshida, C. O. Reinhold, P. Kristöfel, J. Burgdörfer, S. Watanabe, and F. B. Dunning, *Phys. Rev. A* **59**, R4121 (1999).
- [63] R. V. Jensen, M. M. Sanders, M. Saraceno, and B. Sundaram, *Phys. Rev. Lett.* **63**, 2771 (1989).
- [64] J. N. Bardsley and M. J. Comella, *Phys. Rev. A* **39**, 2252 (1989).
- [65] N. Ben-Tal, N. Moiseyev, R. Kosloff, and C. Cerjan, *J. Phys. B* **26**, 1445 (1993).

- [66] N. Ben-Tal, N. Moiseyev, and R. Kosloff, Phys. Rev. A **48**, 2437 (1993).
- [67] N. Ben-Tal, N. Moiseyev, and R. Kosloff, J. Chem. Phys. **98**, 9610 (1993).
- [68] H. A. Kramers, *Collected Scientific Papers* (North-Holland, Amsterdam, 1956), p. 272; W. C. Henneberger, Phys. Rev. Lett. **52**, 613 (1984).
- [69] W. P. Reinhardt, Ann. Rev. Phys. Chem. **33**, 223 (1982).
- [70] N. Moiseyev, Phys. Rep. **302**, 211 (1998).
- [71] N. Moiseyev, J. Phys. B **31**, 1431 (1998).
- [72] I. Vorobeichik and N. Moiseyev, Phys. Rev. A **59**, 1699 (1999).
- [73] R. Zavin, I. Vorobeichik, and N. Moiseyev, Chem. Phys. Lett. **288**, 413 (1998).
- [74] O. E. Alon and N. Moiseyev, Phys. Rev. A **46**, 3807 (1992); N. Lipkin, N. Moiseyev, and E. Brändas, Phys. Rev. A **40**, 549 (1989).
- [75] Y. Gontier and M. Trahin, Phys. Rev. A **19**, 264 (1979).
- [76] T. Timberlake and L. E. Reichl, Phys. Rev. A **59**, 2886 (1999).
- [77] W. E. Lamb, Jr., Phys. Rev. **85**, 259 (1952); C. R. Holt, M. G. Raymer, and W. P. Reinhardt, Phys. Rev. A **27**, 2971 (1983).
- [78] T. Timberlake and L. E. Reichl (unpublished).

- [79] N. Moiseyev and H. J. Korsch, Phys. Rev. A **44**, 7797 (1991).
- [80] N. Rosen and P. M. Morse, Phys. Rev. **42**, 210 (1932).
- [81] N. Moiseyev and H. J. Korsch, Phys. Rev. A **41**, 498 (1990); N. Ben-Tal, N. Moiseyev, C. Leforestier, and R. Kosloff, J. Chem. Phys. **94**, 7311 (1991).
- [82] J. H. Shirley, Phys. Rev. **138**, B979 (1965); H. Sambe, Phys. Rev. **A39**, 2203 (1973).
- [83] K. Husimi, Proc. Phys. Math. Soc. Jpn. **22**, 246 (1940); K. Takahashi, Prog. Theo. Phys. Supp. **98**, 109 (1989).
- [84] B. Crespi, G. Perez, and S. J. Chang, Phys. Rev. E **47**, 986 (1993).
- [85] H. Goldstein, *Classical Mechanics, 2nd Ed.* (Addison-Wesley, Reading, Massachusetts, 1980).

Vita

Todd Keene Timberlake was born in Rome, Georgia to Susan Keene Timberlake and Guy Jackson Timberlake, Jr. on December 14, 1973. While attending school he lived in Ohio, Virginia, New Jersey, and South Carolina. He graduated from Christ Church Episcopal School in Greenville, South Carolina in 1990. He immediately entered Vanderbilt University where he received the Bachelor of Science in Physics/Astronomy and Mathematics, summa cum laude with Honors in the College of Arts & Science, in 1994. In August, 1994 he began graduate studies in the Physics Department of the University of Texas at Austin. In 1998 he married Karen Lee Peterson and moved to Houston, Texas while continuing his graduate work. From 1998 to 2001 he taught mathematics at St. John's School in Houston, Texas. In the Fall of 2001 he will begin work as an Assistant Professor of Physics at Berry College in Rome, Georgia.

Permanent Address: 1909 Banks St., Houston, TX 77098

This dissertation was typeset with L^AT_EX by the author.